

FERROMAGNETIC JOSEPHSON JUNCTIONS WITH BOTH IN AND
OUT OF PLANE MAGNETO ANISOTROPY

By

Victor Aguilar

A DISSERTATION

Submitted to
Michigan State University
in partial fulfillment of the requirements
for the degree of

Physics—Doctor of Philosophy

2021

ABSTRACT

FERROMAGNETIC JOSEPHSON JUNCTIONS WITH BOTH IN AND OUT OF PLANE MAGNETO ANISOTROPY

By

Victor Aguilar

In this thesis we present experimental data showing enhancements of critical current through ferromagnetic Josephson junctions. Previous work in our group has shown promising results using ferromagnets with perpendicular magnetic anisotropy (PMA) as one of the magnetic layers in Josephson junctions. Magnetic characterization has shown that these PMA layers have strong out of plane magnetization. In this work we use a multilayer of palladium and cobalt as the PMA layer. By depositing the PMA layer as the central ferromagnet in between two other ferromagnets we are able to generate long range spin triplet supercurrent. There are both benefits and drawbacks with spin triplet supercurrent when compared to spin singlet supercurrent. We present a method used to confirm the presence of spin-triplet supercurrent generation from an S-type superconductor. We also compare the magnitude of the spin-triplet supercurrent in our junctions with the supercurrent in similar junctions where the central PMA layer is configured as a synthetic antiferromagnet. Finally we show data from phase sensitive measurements where we have fabricated a device with two Josephson junctions that can each be in one of two phases, either a 0 or π state. This last set of data shows switches of phase in Josephson junctions that are controlled by an external magnetic field, which can have applications in cryogenic memory.

Copyright by
VICTOR AGUILAR
2021

ACKNOWLEDGMENTS

TABLE OF CONTENTS

LIST OF TABLES	viii
LIST OF FIGURES	ix
Chapter 1 Introduction	1
1.1 Superconducting computing, energy efficiency and cryogenic memory	1
1.1.1 Background: energy use in large-scale computing systems	1
1.1.2 Superconducting computing	2
1.1.3 Spin-triplet supercurrent	5
1.2 Chapters overview	6
Chapter 2 Superconductivity and Magnetism	8
2.1 The Meissner-Ochsenfeld Effect	9
2.2 The Josephson Effect	11
2.3 Ferromagnetism	13
2.3.1 Magnetic Domains	13
2.3.2 Magnetic Anisotropy	14
2.4 Proximity effects in Josephson junctions	15
2.4.1 S/N proximity effect	15
2.4.2 S/F proximity effect	18
2.4.2.1 Current-phase relation of ferromagnetic Josephson junctions	22
2.5 Long range spin-triplet supercurrent in S/F ['] /F/F ['] /S Josephson junctions	24
2.6 SQUIDs	27
Chapter 3 Experimental Techniques	32
3.1 Microfabrication Techniques	32
3.1.1 Photolithography	32
3.1.2 Electron Beam Lithography	33
3.1.3 Sputtering	33
3.1.4 Ion Milling	34
3.2 Magnetic characterization	34
3.3 Josephson Junction Fabrication Procedure	36
3.3.1 Sample Preparation	36
3.3.2 Photolithography: setup and bottom lead deposition	37
3.3.3 Sputtering Chamber	39
3.3.4 Electron beam lithography-EBL	41
3.3.5 Junction definition by ion milling	42
3.3.6 Top lead	46
3.4 Measurement	46
3.4.1 Setup and mounting	46
3.4.2 Single junctions	47

3.4.3	Phase Sensitive Measurements-Superconducting Quantum Interference Device (SQUID)	48
3.5	Improvements to measurement and fabrication systems	49
3.5.1	Room temperature electronics:	49
3.5.2	Low temperature electronics:	49
3.5.3	Rezanator and sputtering chamber:	50
Chapter 4	Shuffled and Triplet Josephson junctions	51
4.1	Magnetic characterization of Pd/Co multilayers	54
4.2	Fabrication of junctions containing Pd/Co	58
4.3	Measurement	61
4.4	Results	64
4.5	Conclusions	65
Chapter 5	PMA-SAF and PMA Josephson junctions	68
5.1	Magnetic Properties	69
5.2	Fabrication of spin triplet PMA and PMA-SAF junctions	70
5.3	Measurement	72
5.4	Results	73
5.5	Conclusions	80
Chapter 6	Phase Controllable SQUIDS	82
6.1	Magnetic characterization	83
6.2	SQUID fabrication	85
6.3	Measurement	88
6.4	Results	91
6.5	Conclusions	100
Chapter 7	Conclusions and outlook	102
APPENDIX	106
REFERENCES	107

LIST OF TABLES

Table 6.1: Sample ferromagnets	100
Table 6.2: Maximum critical current	100
Table 6.3: Sample Resistance	101

LIST OF FIGURES

Figure 1.1: Memory Cell	5
Figure 2.1: Meissner Effect	9
Figure 2.2: Josephson Effect	12
Figure 2.3: Magnetic Domains	14
Figure 2.4: Schematic of Andreev Reflection	16
Figure 2.5: Band Structure	19
Figure 2.6: S/N and S/F Pair Correlation Functions	21
Figure 2.7: S/F/S Junctions Critical Current vs. Thickness	23
Figure 2.8: Triplet Josephson Junction	25
Figure 2.9: Schematic view of a dc SQUID	28
Figure 2.10: Critical current vs applied flux dc SQUID	31
Figure 3.1: Fabrication Process	38
Figure 3.2: Junction Array	45
Figure 4.1: Singlet and Triplet	52
Figure 4.2: PMA-SAF Junctions	53
Figure 4.3: Magnetic force microscopy of Pd/Co multilayers	55
Figure 4.4: Hysteresis Curve of Pd/Co multilayers: Out-of-plane	56
Figure 4.5: Hysteresis Curve of Pd/Co multilayers: In-plane	57
Figure 4.6: Photolithography Bottom Lead	60
Figure 4.7: Sample mounted on QDI	61
Figure 4.8: Photolithography Bottom Lead	62

Figure 4.9: V vs. I	63
Figure 4.10: I_c vs. H	65
Figure 4.11: $I_c R_n$ vs. Ni Thickness	66
Figure 5.1: PMA-SAF and PMA	70
Figure 5.2: PMA-SAF and PMA Josephson junctions	71
Figure 5.3: PMA Triplet Fraunhofer pattern	73
Figure 5.4: PMA-SAF Decay	74
Figure 5.5: PMA-SAF Decay	79
Figure 5.6: PMA Decay	79
Figure 6.1: Triplet PMA Josephson Junction	83
Figure 6.2: Easy axis magnetometer of elliptical and hex arrays: major loops	84
Figure 6.3: Easy axis magnetometer of elliptical and hex arrays: minor loops	85
Figure 6.4: Photolithography SQUID mask design	86
Figure 6.5: Top and orthographics view of ULI SQUID design	87
Figure 6.6: Wiring diagram for SQUID using QDI	88
Figure 6.7: Measurement Flow Diagram	89
Figure 6.8: Initial measurements	90
Figure 6.9: Sample 1a SQUID 3 before training	93
Figure 6.10: Sample 1a SQUID 3 after training	94
Figure 6.11: Sample 1a SQUID 1	95
Figure 6.12: Sample 1a SQUID 1	96
Figure 6.13: Sample 4a SQUID 2	97
Figure 6.14: Sample 4a SQUID 3	98

Figure 6.15: Sample 6a SQUID 1 99

Chapter 1

Introduction

1.1 Superconducting computing, energy efficiency and cryogenic memory

1.1.1 Background: energy use in large-scale computing systems

With the emergence of new technologies and the ability to have so much information stored and accessed by simply having access to a computer and internet we continue to see a rise in computer storage and the need for larger and larger data centers. When first joining this group, in 2014, energy usage in the U.S. from 2009 to 2020 was projected to go from 72 to 176 TWh [1], which was one of the key motivators for this research. Reducing energy consumption in technology was then and is now a major driving force since estimates said that reducing the data center energy consumption by a factor of 10 could potentially save the United States about \$15 billion dollars by the year 2020 assuming an energy cost of 0.1 \$/kWh. Another study published a couple of years later showed that globally electricity demands of data centers would be about 700 TWh in the year 2020 [2]. This study also showed that by the year 2030 the global electricity demand of data centers will be in the best case about 1137 TWh and up to 7933 TWh in the worst case scenario.

Data centers are not the only increasing consumers of energy; supercomputers are getting larger, faster, and more power hungry. The projected computing power of up to 10^{18} calculations per second at the Exascale Computing Project at Los Alamos, faster than current supercomputers at about 10^{15} calculations per second, indicates an even greater need for

energy efficiency to deal with these advancements in technologies. Supercomputers play a large role in the solving new and more complex problems. They are being used in many fields including quantum mechanics, weather forecasting, climate research and physical simulations to name a few examples. Breakthroughs in these fields are fueling new and more exciting discoveries. Although we have seen a steady rise in computing power ever since the introduction of this technology, it is limited by a few key factors. Processor manufacturers face many challenges, one of which is the limit in size, more computing power in a smaller area. Intel is pushing towards sub nanometer production processors in the near future [3]. Cooling is another factor that must be looked at carefully when producing smaller and more powerful processors. Power dissipation in smaller areas is limited by surface area meaning these smaller chips will be running faster but also much hotter.

Energy efficiency is also an important obstacle at large scale. The power consumption of one of the most powerful modern supercomputers, the Sunway TaihuLight [4] with over 10.5 million cores, can be as high as 15MW at a peak performance of 93 petaFLOPS. The power consumption of next generation computers, exaFLOPS supercomputers, is predicted to be in the sub-gigawatts level [5]. This is similar to the power generated by a small powerplant which can cost hundreds of millions of dollars per year. Taking into account all the factors that can lead to an increase in energy usage is difficult but the overall trend leads to a need for a more energy efficient solution when compared to the Complementary Metal Oxide Semiconductor (CMOS) technology we have all grown accustomed to using.

1.1.2 Superconducting computing

To try to alleviate this inevitable rise in power consumption when considering large scale computing and data centers, one proposal is to develop superconducting computers which

are expected to have orders of magnitude better energy efficiency over conventional CMOS technology [1]. The reasoning behind the energy efficiency comes from superconducting materials having the ability to carry current with zero energy loss due to Joule heating. In a system with Very-Large-Scale integration combining thousands of circuits, having superconducting components closely packed to each other without the worry of heat generation decreases time delays in interchip communications. To attain these superconducting states we must use materials that superconduct and cool them down to temperatures below their “critical temperature”, or T_c . For Niobium, the most commonly used superconducting material, T_c is just above 9 K. To reach temperatures below 9K we use liquid helium at about 4.2 K. Although it does cost a significant amount for cooling the circuits to liquid helium temperatures, this is taken into account when comparing superconducting computers over CMOS systems.

An important milestone in superconducting devices was discovered in the 1962 by Brian David Josephson, the Josephson effect, where you can have supercurrent flow across a thin, non-superconducting, barrier that is sandwiched by two superconductors. This discovery paved the way for new types of logic circuits that were based on what is known as a Josephson junction. A Josephson junction is based on the Josephson effect and is fabricated with different layers as you would imagine stacking coins on top of each other where each coin is a different material. One of these logic circuits is known as Resistive Single-Flux Quantum (RSFQ) logic. RSFQ was proposed by Konstantin Likharev, Oleg Mukhanov, and Vasili Semenov in 1985 at Moscow State University as a Josephson junction based logic that was able to achieve fast switching at picosecond time scales [6]. The RSFQ logic uses picosecond SFQ voltage pulses that can encode, process, and transport digital information as opposed to voltage levels produced by transistors in semiconductor technology. There have

been many more superconducting logic families based on Josephson junctions that have been developed. In one variant, reducing the resistor and adding an inductor in parallel to the RSFQ (LR-RSFQ) made a more energy efficient circuit. [7]. By reducing the bias voltage in a RSFQ circuit you can also increase the energy efficiency giving a Low Voltage RSFQ (LV-RSFQ) [8]. As the name suggests the energy efficient RSFQ (eeRSFQ) [9] helps eliminate the static power losses of the RSFQ by replacing bias resistors with sets of inductors and current-limiting Josephson junctions. More closely related to our work the Reciprocal Quantum Logic(RQL) [10] was developed by Northrop Grumman Corporation and uses reciprocal pairs of SFQ pulses to encode a logical ‘1’ and works with alternating current. Finally I will just mention the Adiabatic Quantum flux parametron (AQFP) logic [11] which uses alternating current and was developed to be extremely energy efficient, but is slower than SFQ-based logic.

There are many components needed to have a working superconducting computer but our work focuses on the memory element of a superconducting computer. There are many researchers along with our group working on Josephson junctions containing ferromagnetic layers that can be used in a superconducting memory circuit [12–22]. Such a memory must be capable of switching quickly, have random access, and be non-volatile similar to Magnetic Random-Access Memory (MRAM). The benefit as mentioned previously over conventional logic circuits would be the gain in energy efficiency in the superconducting circuits.

An important step for this work is the proposed memory architecture from Northrop known as JM RAM. The JM RAM memory cell is composed of several elements, one of which is a ferromagnetic Josephson junction(MJJ) with a controllable ground-state phase shift. The readout of the memory is accomplished by applying flux to a selected memory cell so that the bit-read current exceeds the readout SQUID critical current in one memory state,

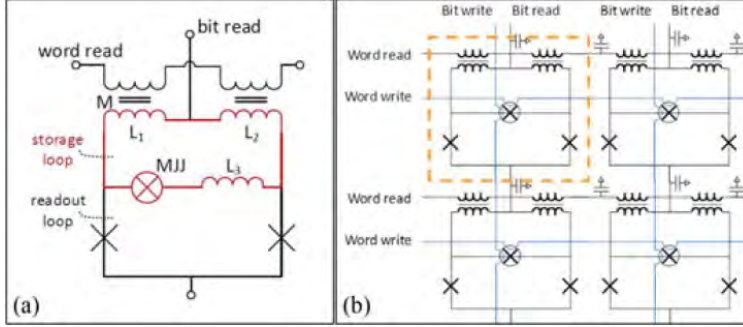


Figure 1.1: **Memory Cell** Diagram of a superconducting memory cell by Northrop Grumman. The left diagram is the memory cell where the X marks Josephson junctions. The right diagram is an array of memory cells. Taken from [23].

but not the other [23]. The MJJ is what our work focuses on [24–26].

The Northrop JMRAM memory cell is shown in Figure 1.1 where (a) is the memory cell and (b) is an array of memory cells showing the read and write lines [23]. In this circuit the magnetic Josephson junction plays the role as a bit by adding a variable phase to the SQUID loop [18,24,27]. Simply put the junction would serve as the “0” or “1” for the binary memory.

1.1.3 Spin-triplet supercurrent

The work in this thesis focusses on a special type of ferromagnetic Josephson junction in which the supercurrent is carried by spin-triplet electron pairs rather than the usual spin-singlet pairs found in conventional superconductors such as Niobium. The spin triplet supercurrent is fundamental to the following work. Spin triplet supercurrent has the unique property that it can travel significantly further than the spin singlet supercurrent in ferromagnets – almost as if they were normal metals. Our group has done extensive work on spin singlet ferromagnetic junctions and in some cases shown phase control of these types of junctions [18–20,24–26]. Our group has also demonstrated the generation and control of spin triplet supercurrent [28–31]. The culmination of that work was Joseph Glick’s demon-

stration of phase control with spin triplet supercurrent [27]. The limitation of that work was that the critical current in those junctions was too small for applications to the cryogenic memory discussed previously. The work we present here is specifically done to address that point of being able to have higher critical current with spin triplet supercurrent while still maintaining phase control. The spin triplet supercurrent is of particular interest because of its forgiving nature when considering how robust it is in terms of thickness variations of the central ferromagnetic layer. This may allow the triplet junctions to be easier to fabricate compared to spin singlet junctions. In this work we plan to answer the question whether it is possible to improve the critical current in spin-triplet Josephson junctions and then show phase control. This is done by characterizing, fabricating and measuring both spin triplet and control or spin singlet Josephson junctions [22]. Since the interplay of ferromagnetism and superconductivity are thought to counteract each other it is fascinating to see the interesting physics we have that could not exist without their coexistence.

1.2 Chapters overview

Chapter 2 give a brief discussion of superconductivity and magnetism starting with the Meissner-Ochsenfeld effect and Josephson effect. We then give a brief overview of ferromagnetism where we discuss magnetic domains and magnetic anisotropy. Superconducting Quantum Interference Device(SQUID) devices are briefly covered as the main part of the work requires them as a measurement tool. We then introduce the physics of S/N and S/F interfaces discussing supercurrent generation and propagation.

Chapter 3 gives a very detailed step-by-step explanation of experimental techniques used in nano-fabrication. Topics include fabrication techniques such as photolithography, elec-

tron beam lithography, sputtering and ion milling. There is a discussion of magnetic measurements using a SQUID magnetometer. Finally there is a section that deals with the measurement of samples as well as improvements made to various fabrication systems.

Chapter 4 provides the motivation behind the use of spin triplet junctions as possible memory bits. Since spin-triplet Josephson junctions are more forgiving in terms of thickness variations that can happen during the fabrication process, when compared to singlet junctions, they may be easier to fabricate in large quantities. The main point of this chapter is to show that the main contribution to the supercurrent in these types of junctions are spin-triplet pairs. This work lays the groundwork for chapters 5 and 6.

Chapter 5 provides a comparison of spin-triplet junctions containing a multilayer with perpendicular magnetic anisotropy arranged as a synthetic antiferromagnet (PMA-SAF), and junctions that contain only the perpendicular magnetic anisotropy (PMA) multilayer. There is an interpretation of what may cause the PMA junctions to have a shallower decay of critical current with increasing the number of bilayers in the multilayer, when compared to the PMA-SAF junctions.

Chapter 6 will show how we fabricate the on-chip SQUIDs used in conjunctions with our junctions to make our phase-sensitive measurements. We show some magnetics measurements used to characterize the junctions as arrays before fabrication of SQUIDs. We also show some measurement procedures as well and wiring steps for these samples. Finally we show data on the SQUIDs in what we refer to as “waterfall plots” in which we plot critical current as a function of external field and flux line current.

Chapter 7 is the summary chapter where we discuss results and possible outlooks for future experiments.

Chapter 2

Superconductivity and Magnetism

Superconductivity was first discovered in 1911 by Dutch physicist Heike Kamerlingh Onnes of Leiden University. A sample of mercury was cooled down to 4 degrees Kelvin, below its transition temperature, T_c , where the electrical resistance of this sample dropped to zero [32]. The remarkably discovery dawned the age of superconductivity. Onnes won the Nobel Prize for research in the field in 1913. Another related discovery was made in 1933 by German researchers Walther Meissner and Robert Ochsenfeld. They found that when a material is superconducting that it has the peculiar ability to expel magnetic fields [33]. This phenomenon is known as the Meissner effect. The field of superconductivity contains many materials than can superconduct from elements such as mercury, lead and niobium to more complicated materials such as yttrium barium copper oxide which has a much higher superconducting temperature of about 92 K. Conventional superconductors, the superconductors used in this work, have a full microscopic theory know as BCS theory. BCS theory was developed by J. Bardeen, L.N. Cooper and J.R. Schrieffer in 1957, who showed that dissipationless current flow in the superconducting state is caused by electron pairs [34, 35]. In this theory the electron pairs, know as Cooper pairs, behave as bosons, with zero total spin and momentum. The Cooper pairs condense to the lowest energy state characterized by a single phase-coherent wavefunction. This chapter will discuss the Meissner effect, the Josephson effect, Superconducting QUantum Interference Devices (SQUIDs), Magnetics Domains and the physics of superconducting/ferromagnetic (S/F) hybrid systems including the

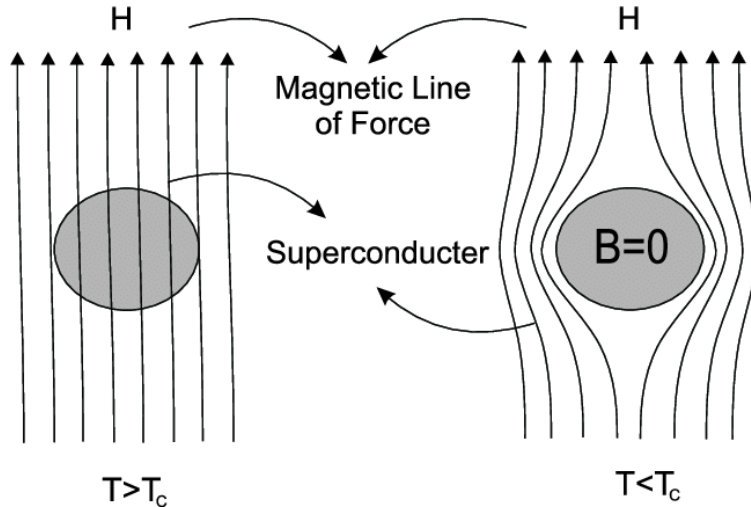


Figure 2.1: **Meissner Effect** Cartoon representation of a Meissner Effect. The left image shows the superconductor above T_c where the magnetic field B penetrates the material. The right side image shows the same superconductor below T_c where the magnetic field is expelled and we see there is zero net field inside the superconductor. Taken from [36].

properties of S/F/S Josephson junctions.

2.1 The Meissner-Ochsenfeld Effect

For simplicity we will look at the main points of the Meissner effect. When superconducting metals are cooled below their T_c they have the ability to expel magnetic flux from their interior [33]. The cause of this effect is that the superconductor generates surface currents that produce a field that exactly cancels the external field inside of the material. Interestingly this effect causes the superconductor to behave as a perfect diamagnet in the presence of an external magnetic field.

The Meissner Effect is a telltale sign of superconductivity. The brothers F. and H. London wrote down a pair of simple equations which incorporate the electrodynamic response of a superconductor. These equations describe the microscopic electric and magnetic fields inside a superconductor. Start with Newton's second law ($\mathbf{F} = m\mathbf{a}$) applied to the electrons in a

superconductor:

$$-e\mathbf{E} = m\frac{d\mathbf{v}}{dt}, \quad (2.1)$$

The current density is

$$\mathbf{J} = n(-e)\mathbf{v}, \quad (2.2)$$

Combining the previous two equations and assuming that superconducting electrons do not have their velocities reduced to zero by means of scattering, we have:

$$\partial\mathbf{J}/\partial t = \mathbf{E}/\Lambda, \quad (2.3)$$

where the time derivative of the current density, \mathbf{J} , is proportional to \mathbf{E} , and $\Lambda \equiv m/(e^2n_s)$. The factor e is the magnitude of the electron charge and m it's mass, and n_s is the density of superconducting electrons. Applying Maxwell equation $\nabla \times \mathbf{E} = -\partial\mathbf{B}/\partial t$, where \mathbf{B} is the magnetic field and taking the curl of 2.3, we get

$$\frac{\partial}{\partial t} \left[\nabla \times \mathbf{J} + \frac{\mathbf{B}}{\Lambda} \right] = 0. \quad (2.4)$$

which shows that the quantity inside the brackets is conserved. Given that deep inside a bulk superconductor, $\mathbf{J} = 0$ and $\mathbf{B} = 0$, we now have the London equation,

$$\nabla \times \mathbf{J} + \frac{\mathbf{B}}{\Lambda} = 0. \quad (2.5)$$

Using the Maxwell relation,

$$\nabla \times \mathbf{B} = \mu_0\mathbf{J} + \mu_0\epsilon_0(\partial\mathbf{E}/\partial t) \quad (2.6)$$

taking the curl of both sides, assuming that the electric field \mathbf{E} is constant in time we have,

$$\nabla \times (\nabla \times \mathbf{B}) = \mu_0 \nabla \times \mathbf{J} \quad (2.7)$$

which gives

$$\nabla(\nabla \cdot \mathbf{B}) - \nabla^2 \mathbf{B} = -\frac{\mu_0}{\Lambda} \mathbf{B} \quad (2.8)$$

now using $\nabla \cdot \mathbf{B} = 0$ in the previous equation we get,

$$\nabla^2 \mathbf{B} = \frac{\mu_0}{\Lambda} \mathbf{B} \quad (2.9)$$

$$\nabla^2 \mathbf{J} = \frac{\mu_0}{\Lambda} \mathbf{J}. \quad (2.10)$$

The μ_0/Λ is related to the length scale that fields can penetrate into the superconductor, which is known as the **London penetration depth**:

$$\lambda_L \equiv \sqrt{\Lambda/\mu_0} = \sqrt{m/(\mu_0 e^2 n_s)}. \quad (2.11)$$

2.2 The Josephson Effect

The Josephson effect is a macroscopic quantum phenomenon. In 1962 British physicist Brian Josephson predicted that supercurrent can flow between two superconductors that are separated by a thin barrier, without any external bias voltage applied. For that work he won the Nobel prize in Physics in 1973.

In this system we can write supercurrent I_s as a function of the critical current I_c and

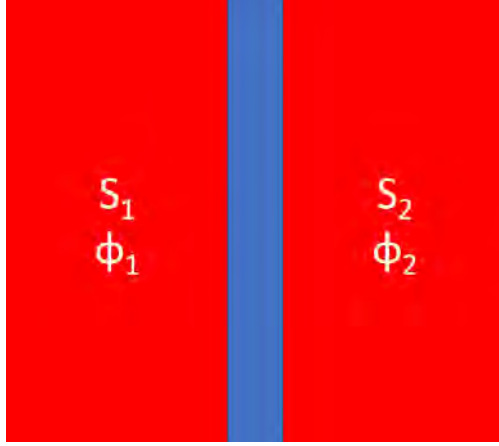


Figure 2.2: **Josephson Effect** Cartoon representation of a Josephson junction that contains two superconductors separated by a thin barrier. Each of the superconductors has its own intrinsic phase.

the phase difference ϕ across the junction:

$$I_s = I_c \sin \phi, \quad (2.12)$$

where $\phi = \phi_2 - \phi_1$. The equation is known as the current-phase relation.

If the current is larger than the critical current there will be a measurable voltage across the junction. In that case the phase acquires a time dependence,

$$\frac{d\phi}{dt} = \frac{2eV}{\hbar} = \frac{2\pi}{\Phi_0} V, \quad (2.13)$$

where $\Phi_0 = 2\pi\hbar/(2e)$ is the magnetic flux quantum. As a result, the supercurrent Eq. (2.12) oscillates at a frequency $\nu = 2eV/h$ and the energy of a Cooper pair traversing the junction changes by an amount $h\nu$.

By integrating the work done by the current to change the phase we get the Josephson energy stored in the junction.

$$E = \int I_s V dt = \frac{\hbar}{2e} \int I_c \sin \phi d\phi = E_J(1 - \cos \phi), \quad (2.14)$$

where we used Eq. (2.13) to change the energy integral from time to phase. The Josephson coupling energy is

$$E_J = \frac{\hbar I_c}{2e}. \quad (2.15)$$

2.3 Ferromagnetism

Like superconductivity, ferromagnetism is also a quantum phenomena that is observable macroscopically. In the following we discuss a brief description of what leads to ferromagnetism. Since spin is the dominant source to ferromagnetism we will try to give some understanding of this mechanism. We start by viewing the electrons magnetic moments as tiny magnets. In a ferromagnetic material, the exchange interaction causes neighboring spins to align parallel to each other. The exchange interaction is a consequence of Coulomb repulsion and the antisymmetry of the two-electron wavefunctions under particle exchange. Once the spins, and hence the magnetic moments, are aligned we see their effect on a much larger scale causing the ferromagnetism that can be observed.

2.3.1 Magnetic Domains

Considering a system that contains many dipoles that make up some material we know that the exchange energy is the leading term in how they behave microscopically. Figure 2.3 shows a series of systems that start with a single domain on the left and gradually increase in domains as you move to the right. We can see from the first image on the left we have a single

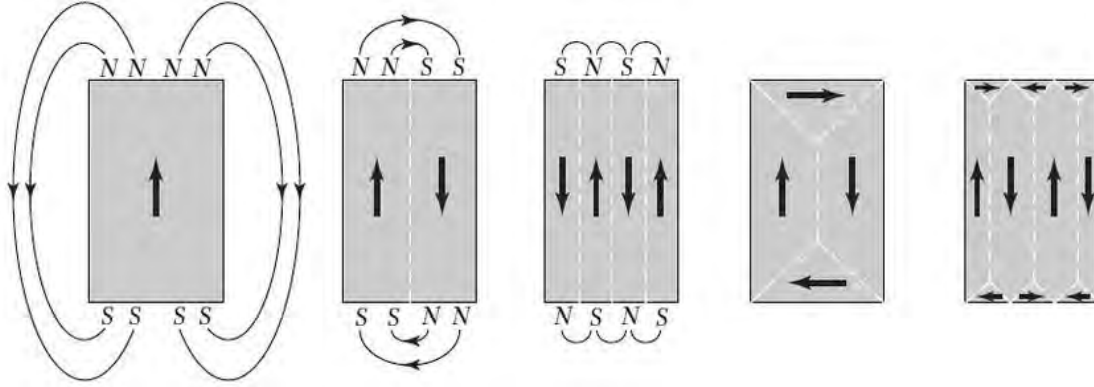


Figure 2.3: **Magnetic Domains** Cartoon representation of magnetic domains, starting from a single domain (left image) to increasing the number of domains moving right. The single-domain configuration has the smallest exchange energy but large magnetostatic energy. As you move to the right the exchange energy is increased due to the additions of domain walls, but the magnetostatic energy is lowered. Taken from [37].

domain ferromagnet with the lowest exchange energy but with large magnetostatic energy due to the large magnetic field created outside of the material. As we move to the right the number of domains increases, lowering the magnetostatic energy, and increasing the number of domain walls. Domain walls are very narrow surfaces which are continuous transitions between adjoining domains. The more domain walls we have the larger the exchange energy. The system is trying to decrease its energy so there is a point where breaking up into smaller domains is no longer favorable because of increasing exchange energy due to creating more domain walls.

2.3.2 Magnetic Anisotropy

Our work takes advantage of many types of magnetic anisotropy that can occur in metals. Magnetic anisotropy occurs when a ferromagnet has a preferred direction to have its spins pointing along. The preferred directions is called the easy axis while the perpendicular direction is called the hard axis. In our work we make use of what is called shape anisotropy where we purposely grow magnetic materials in elliptical shapes causing them to have

their easy axis pointing along the long axis of the ellipse. This shape is chosen because the magnetization direction can be switched between the two opposite directions using an external magnetic field. We can also have materials that have magnetocrystalline anisotropy where the combination of crystal structure and spin-orbit coupling causes the magnetization to preferentially point along certain crystallographic directions. Specifically for our work we use materials with low magnetocrystalline anisotropy, such as NiFe (Permalloy), to easily switch the direction of magnetization with an external magnetic field. We also use materials with higher magnetocrystalline anisotropy, such as nickel, to have their magnetization set in a certain direction and not change during a measurement. Finally we use materials that are fabricated so they have an out-of-plane magnetization, called perpendicular magnetocrystalline anisotropy (PMA), driven by strong spin-orbit coupling at the interface between Pd and Co.

2.4 Proximity effects in Josephson junctions

2.4.1 S/N proximity effect

The previous sections discussed traditional Josephson junctions that contain a thin insulating tunnel barrier. Now we focus our discussion on situations that more closely represent our experiment. The work described in this thesis involves Josephson junctions that contain normal metals as well as ferromagnets. Since the following experiments use several metals such as Cu, Pd, Ru among others we will present a simple mechanism behind charge transfer in a S/N system. Andreev reflection, named after Russian physicist Alexander F. Andreev, was discovered in 1964 and describes the scattering process that occurs when an electron in a normal metal approaches a superconductor [38]. During the process each Andreev reflection

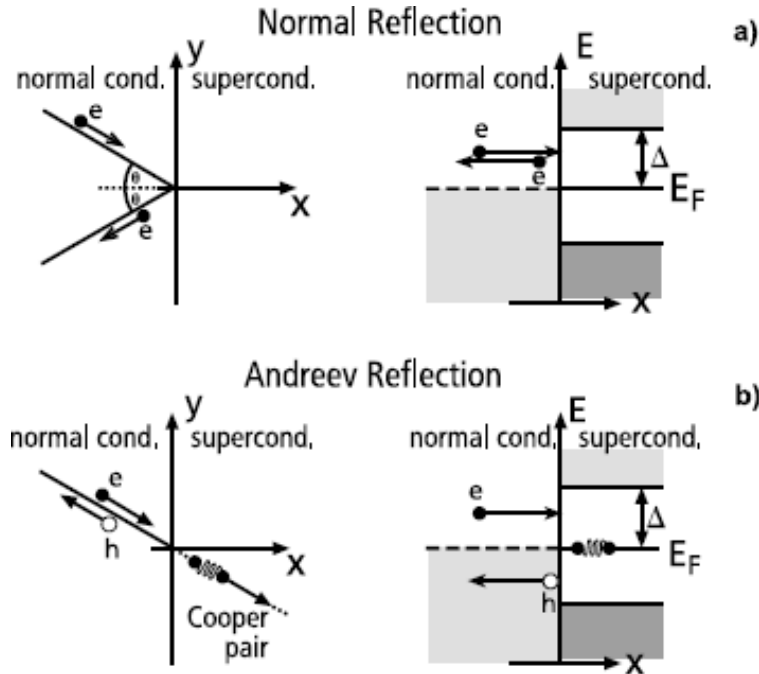


Figure 2.4: **Schematic of Andreev Reflection** Schematic of Andreev Reflection. a) Normal reflection shows an electron reflecting at the interface with the superconductor and scattered back into the normal metal. b) Andreev reflection shows an electron incident on the interface and a hole scattering back into the normal metal. Inside the superconductor a Cooper pair is created causing a $-2e$ transfer of charge into the superconductor. Taken from [39].

transfers a charge of $2e$ across the S/N interface.

Before we discuss Andreev reflection, we have to understand the energy level structure of electrons in a superconductor. As a superconductor cools below its critical temperature the electrons at the Fermi level form Cooper pairs. As we recall Cooper pairs behave like Bosons with zero spin and a single phase-coherent wavefunction. When these Cooper pairs form they have a lower energy than the original two electrons in single electron states. This lower energy causes an energy gap Δ to form in the single electron density of states, as shown in the right side of Figure 2.4. The metal that is next to the superconductor has electrons filled up to the Fermi level. So it appears that electrons can pass from the normal metal to the superconductor only if their energy exceeds Δ above the Fermi level. But there is another way.

Figure 2.4 shows cartoon diagrams of normal reflection and Andreev reflection. An electron propagating through a normal metal is incident at the interface where the metal meets the superconductor. Assume that the energy of the electron is less than Δ , so there are no single-particle states in the superconductor for the electron to occupy. We have two possible results. The not-so-interesting result is when the electron hits this surface and reflects back into the normal metal as seen in the image on the left in Figure 2.4(a). The more interesting result is when the electron performs an Andreev reflection, as shown in Figure 2.4(b). In this process the incident electron reflects as a hole back into the normal metal, which transfers a Cooper pair into the superconductor. The electron needed for this process comes from below the Fermi level in the normal metal, and has opposite spin, momentum and energy compared to the incident electron.

The reverse of this process is when a Cooper pair in the superconductor enters the normal metal producing two electrons that are no longer bound as a pair. The electrons do retain some phase coherence up to a certain length, known as ξ_N , which depends on the material and temperature. The length scale of the coherence depends on whether one considers the ballistic or diffusive limit, i.e. whether the mean free path is larger or smaller than ξ_N [40,41]. One can estimate ξ_N using an Uncertainty Principle argument, where the energy uncertainty comes from the thermal energy $2\pi k_B T$, causing a coherence time of order $\hbar/2\pi k_B T$. During that time an electron propagates a distance

$$\xi_N = \frac{\hbar v_F}{2\pi k_B T} \quad (2.16)$$

In the other limit where the mean free path is much shorter than ξ_N , the diffusive limit,

the electron motion is diffusive with diffusion constant D , and we have

$$\xi_N = \sqrt{\frac{\hbar D}{2\pi k_B T}}. \quad (2.17)$$

This coherence causes the normal metal to acquire some properties that appear to be superconducting. At low temperatures the normal metal coherence length can be as long as a micron. The inverse effect also occurs, whereby "leakage" of Cooper pairs from the superconductor weakens the superconductivity near the boundary.

2.4.2 S/F proximity effect

We now consider the more interesting case where we have a superconductor next to a ferromagnet. Since we have an exchange field and different spin bands in the ferromagnet we have more interesting physics. Here we provide a qualitative explanation of the physics behind the S/F system. For a more in-depth understanding we can look at the work done by Buzdin and Radović [42–45]. For simplicity we will look at the description by Demler, Arnold and Beasley, who modeled the ferromagnet as a normal metal with a Zeeman-like energy splitting between the majority and minority spin bands [46]. They assumed that spin is a good quantum number and Cooper pairs are being adiabatically transported across the SF interface.

First we will look at the band structure of a typical strong ferromagnet. Figure 2.5a shows the band structure for Ni. We notice several energy bands near the Fermi surface. This band structure is very complex. To simplify this superconductivity theorists use a model like figure 2.5b. In this model the ferromagnet has a parabolic band that is spin-split by twice the exchange energy, E_{ex} . They assume that the Fermi velocity is the same in both

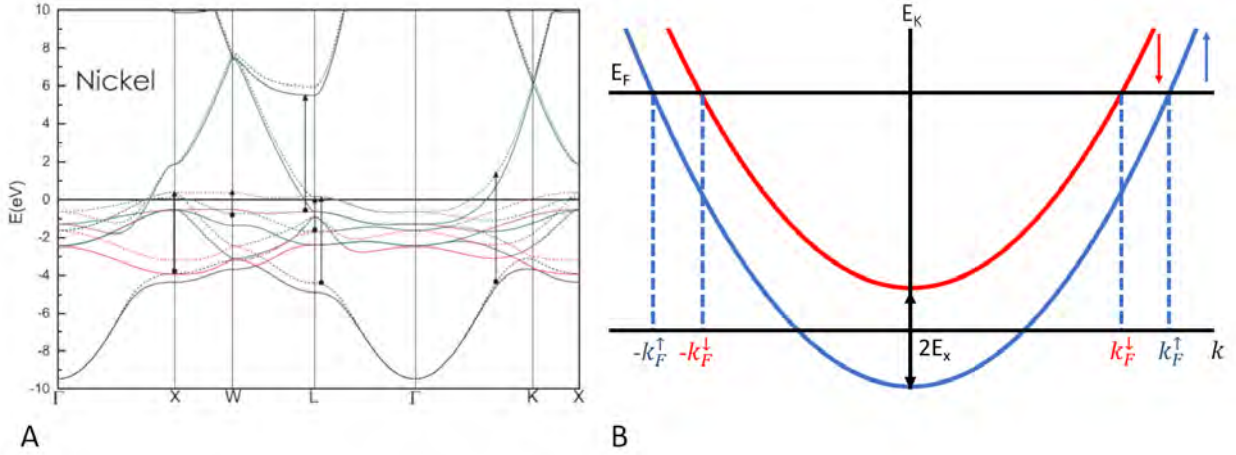


Figure 2.5: **Band Structure** A) Nickel band structure [47] showing energy bands for majority spins (solid lines) and minority spins (dashed lines). B) An idealized band structure for a ferromagnet contains a single parabolic band with spin splitting equal to twice the exchange energy. When a Cooper pair enters the ferromagnet the electrons go into different spin-bands causing the pair to acquire a non-zero center of mass momentum.

since $E_{ex} \ll E_F$.

Since we are studying S/F/S Josephson junctions, we want to know what happens to a Cooper pair that starts in one of the superconducting electrodes, and enters a ferromagnet. Considering only the spin and center-of-mass components of the wavefunction, in S we have the usual spin-singlet wavefunction:

$$\Psi = \frac{1}{\sqrt{2}}(|\uparrow\downarrow\rangle - |\downarrow\uparrow\rangle) \quad (2.18)$$

As the Cooper pair crosses the interface into the ferromagnet the two electrons are no longer in an eigenstate and enter different spin bands. The up-spin electron lowers its potential energy by E_{ex} while the down-spin electron increases its potential energy by E_{ex} . Since the electrons must conserve total energy their kinetic energies must change respectively lead-

ing to a non-zero center of mass momentum

$$\hbar Q = \hbar(k_F^\uparrow - k_F^\downarrow). \quad (2.19)$$

Since $E_{ex} \ll E_F$, we can approximate that as

$$Q = \frac{2E_{ex}}{\hbar v_F}. \quad (2.20)$$

The two terms in the spin-singlet wavefunction acquire opposite momenta: $|\uparrow\downarrow\rangle$ has Q and $|\downarrow\uparrow\rangle$ has $-Q$ center of mass momentum respectively, so we get:

$$\Psi = \frac{1}{\sqrt{2}}(|\uparrow\downarrow\rangle e^{iQX} - |\downarrow\uparrow\rangle e^{-iQX}) \quad (2.21)$$

where X is the center of mass coordinate. Rewriting this equation in terms of sine and cosine we get

$$\Psi = \frac{1}{\sqrt{2}}(|\uparrow\downarrow\rangle - |\downarrow\uparrow\rangle) \cos(QX) + i(|\uparrow\downarrow\rangle + |\downarrow\uparrow\rangle) \sin(QX). \quad (2.22)$$

Now we can see the two components of the pair correlation function inside the ferromagnet. The cosine term is dominant at the origin while the sine term starts from zero and grows larger from there. The cosine term is the spin-singlet term of the function while the sine term is the short range spin-triplet term.

A more general case is when the electron pairs have their momentum at an angle θ with respect to the interface normal, i.e. $\Delta p_x = \hbar/v_F \cos\theta$ and $\Delta p_y = \Delta p_z = 0$. Momentum is conserved in the direction parallel to the interface allowing the momentum to only change

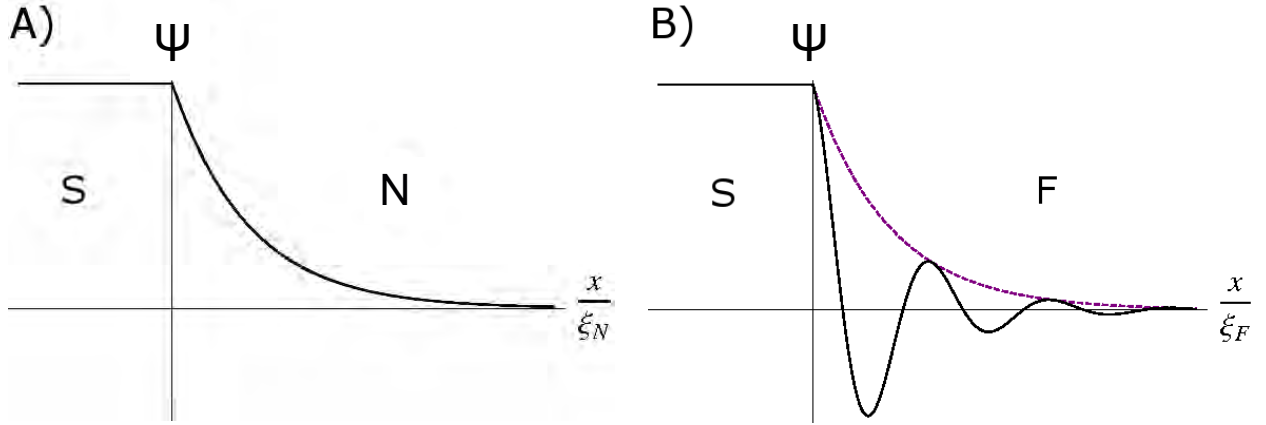


Figure 2.6: **S/N and S/F Pair Correlation Functions** Figure showing the S/N and S/F pair correlation functions. Both have a decay but the S/F system has steeper decay and has an oscillation.

in the x direction. Integrating over all possible angles of incidence gives the overall Cooper pair distribution as

$$\psi \propto \frac{\sin \frac{x}{\xi_F}}{\frac{x}{\xi_F}} \quad (2.23)$$

where the clean-limit coherence length is given by

$$\xi_F = Q^{-1} = \frac{\hbar v_F}{2E_{ex}}. \quad (2.24)$$

and we used Q from Eq 2.20. The dirty limit pair correlation function behaves as

$$\psi \propto e^{\left(\frac{-x}{\xi_F}\right)} \sin\left(\frac{x}{\xi_F}\right) \quad (2.25)$$

with a coherence length of [48]

$$\xi_F = \sqrt{\frac{\hbar D}{E_{ex}}} \quad (2.26)$$

For strong ferromagnets like Ni and Fe the exchange energy is on the order of 1eV [49, 50]

giving a coherence length ξ_F on the order of a nanometer, whereas normal metals can have coherence lengths ξ_N about 1000 times longer.

Figure 2.6 shows a comparison between the S/N and S/F pair correlation functions. The normal metal shows a decay as a function of thickness while the ferromagnet has an oscillation in addition to this decay. The oscillation of the wavefunction in the ferromagnets gives the ability to have π phase coupling between the two superconducting electrodes of a Josephson junction, giving what is known as a π junction which will be discussed in the following section.

2.4.2.1 Current-phase relation of ferromagnetic Josephson junctions

The energy stored in a conventional Josephson junction was found previously in Eq. 2.14 as

$$E(\phi) = \frac{\hbar I_c}{2e} (1 - \cos\phi). \quad (2.27)$$

The energy is minimized when $\phi = 0$. In 1977 Bulaevskii predicted that two superconductors sandwiching an insulator containing magnetic impurities could have a π phase shift (i.e. a sign change) in their Josephson coupling [51]. We saw this type of behavior in fig. 2.6b where the pair correlation function oscillates between positive and negative values as a function of thickness of a ferromagnet. Indeed, Buzdin showed that an S/F/S junction could have either 0 or π coupling depending on the thickness of the F layer. The 0- π oscillations of many ferromagnets have been mapped out by many groups including ours [16, 19, 20, 26, 52–61].

The energy stored in a π junction is

$$E(\phi) = \frac{\hbar I_c}{2e} (1 - \cos(\phi - \pi)) \quad (2.28)$$

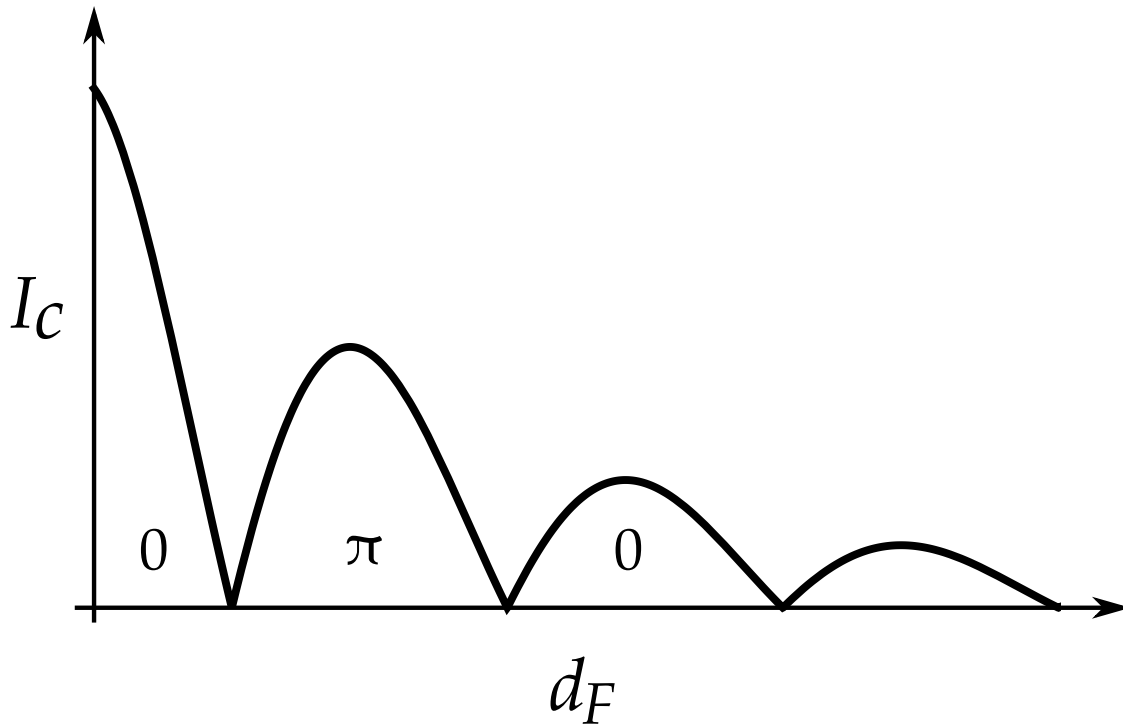


Figure 2.7: **S/F/S Junctions Critical Current vs. Thickness** Plot of a π junctions for S/F/S junction plotting critical current as a function of ferromagnet thickness. The minima delineates separations between standard junctions and π junctions.

making the first minima of the energy occur at $\phi = \pm\pi$.

Since the pair correlation function oscillates with ferromagnet thickness, the critical current does, too. In the diffusive limit, the oscillation of the critical current as a function of ferromagnet thickness can be modeled as

$$I_c = I_{c0} e^{-d_F/\xi_{F1}} * \cos(d_F/\xi_{F2} - \theta) \quad (2.29)$$

where ξ_{F1} and ξ_{F2} are the decay and oscillation length scales of the critical current respectively and θ is a phase shift [43]. I_{c0} is the maximum critical current and d_F is the thickness of the ferromagnet. The point where the critical current drops to zero and rises again indicates a change in ground-state phase going from either 0 to π or π to 0 since we can only measure the absolute value of the critical current in most experiments. Figure 2.7 shows critical current with varying F layer thickness which gives us the ability to map out the phase relation and extract many important features such as coherence length, period of oscillation and the critical current phase relation for a particular F layer.

2.5 Long range spin-triplet supercurrent in S/F'/F/F''/S Josephson junctions

We will now talk about a more complex situation that can occur in S/F systems. In 2001 Bergeret et. al. predicted that it was possible to generate spin triplet pairs from spin singlet pairs by using ferromagnetic layers with non-collinear magnetizations [62]. They and others then predicted several ways that spin triplet pair correlations can be generated in systems containing multiple ferromagnetic layers with magnetic inhomogeneity [62–66]. Those predictions have been verified experimentally by many different techniques [28, 29, 67–

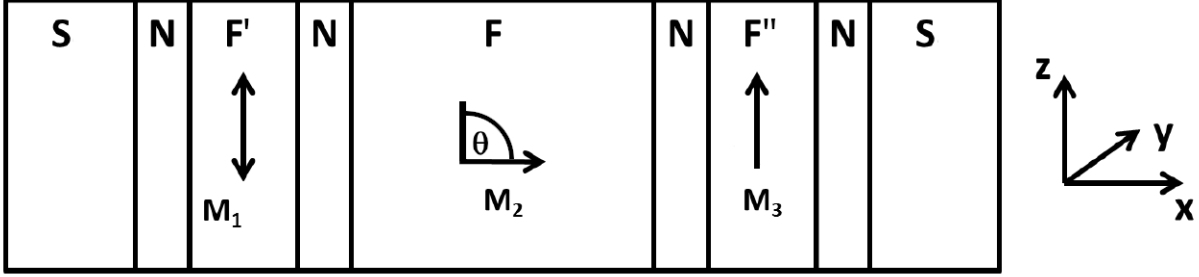


Figure 2.8: **Schematic of a Spin-triplets Josephson junction** Schematic drawing of a ferromagnetic tri-layer that has noncollinear magnetizations of adjacent ferromagnetic layers. S are superconductors, N are normal metals and F, F' and F'' are the ferromagnets. In this case the F' layer is the soft ferromagnet.

86]. In this thesis we will focus on the generation and propagation of spin triplet supercurrent in Josephson junctions containing multiple ferromagnetic layers.

Figure 2.8 is a schematic diagram of a proposal by M. Houzet and A. I. Buzdin in 2007 [87]. This figure shows a S/F'/F/F''/S Josephson junction composed of a ferromagnetic trilayer where by having ferromagnets with non-collinear magnetizations the Josephson current will be dominated by spin-triplet, long-range triplet proximity effect, pairs. If any two adjacent magnetizations are collinear, then only spin-singlet supercurrent is produced. In the work performed in this thesis, F' and F'' are in-plane ferromagnets. The F layer is a ferromagnet that has an out-of-plane magnetization.

Starting with a hand-waving argument we know about the S/F system we have Cooper pairs entering the ferromagnet expressed as a pair correlation function [88]. We can write equation 2.22 as

$$|\Psi\rangle = |0, 0\rangle \cos(QX) + i |1, 0\rangle \sin(QX). \quad (2.30)$$

where we have the pair correlation function in terms of the states $|s, m\rangle$ labeled according

to their total spin quantum number s and projection m . Eq. 2.30 has both the spin singlet $|0, 0\rangle$ and the short range spin triplet $|1, 0\rangle$ components in this representation. The $s = 0$ and $s = 1$ terms both enter the ferromagnetic layer but begin to decay rapidly as a function of F' thickness. The pairs now enter the second F layer that has a non-collinear magnetization with the first F' layer. The $m = 1$ spin triplet component undergoes a basis rotation set by the direction of the magnetization \mathbf{M} in F . The spin singlet component where $m = 0$ is rotationally invariant and does not change in the F layer. In the rotated basis we generate the other two spin triplet components,

$$|1, 0\rangle = \cos(\theta) |1, 0\rangle_\theta + \frac{\sin(\theta)}{\sqrt{2}} |1, 1\rangle_\theta - \frac{\sin(\theta)}{\sqrt{2}} |1, -1\rangle_\theta \quad (2.31)$$

The angle made between the F' and F layer is θ where $|s, m\rangle_\theta$ is expressed in the rotated basis. We have now converted from the short range triplet to the long range spin triplet where we have $|1, 1\rangle$ and $|1, -1\rangle$ as the newly generated long range triplet components. Both of these do not acquire any phase shift since they consist of two electrons in the same spin band. Since we want to have the maximum conversion from the F' to the F layers we use a ferromagnet with out-of-plane magnetization or perpendicular magnetic anisotropy (PMA). The PMA layer gives $\theta = \pi/2$ or $3\pi/2$ which maximizes the triplet supercurrent conversion. The spin singlet and $m = 0$ spin triplet pair correlations decay rapidly in the PMA layer as we have discussed previously. The $m = \pm 1$ components are able to propagate further in the F layer, like in a normal metal, so they are less dependent on thickness than the other pair correlations. The third ferromagnetic layer (F'') is used to convert back into the spin-singlet state since the superconductor only accepts spin-singlet states. The conversion back into spin singlet is done by another basis rotation perpendicular to the F layer.

The ground-state phase of the spin triplet Josephson junctions depends on the relative direction of magnetizations of all three ferromagnets. In our experiments we want to keep the F' and F'' layers in plane and the F layer out-of-plane to maximize the spin triplet conversion. The phase of such a junction, assuming the central PMA layer is not changing, depends on the F' and F'' layers magnetization being either parallel or antiparallel to each other. Having all three layers in plane would also generate spin triplet supercurrent if all three layers have non-collinear magnetizations. The problem with this type of junction is that controlling one layer out of three is extremely difficult. We are using shape anisotropy and an out of plane central ferromagnet to get around this issue. Ideally you want one of the layers to switch at a smaller field than the other one. In our experiments we choose the F' layer to be Permalloy (Py) which has a small switching field while the F'' layer is nickel which has a larger switching field. Although, in theory these junctions are great for generating spin triplet supercurrent, in practice the fabrication is much more difficult and is discussed in the later chapters.

2.6 SQUIDS

The goal of this work is to fabricate phase controllable $0-\pi$ junctions. This means we need to control the magnetics of individual layers within each of our Josephson junctions. The magnetics of the junctions are studied extensively and to verify that we are changing the phase of one of the junctions we have to perform an interference measurement by using a Superconducting QUantum Interference Device (SQUID). SQUIDS were first made by Robert Jaklevic, John J. Lambe, James Mercereau, and Arnold Silver at Ford Research Labs in 1964 [89]. SQUIDS are able to detect magnetic fields as small as a millionth as strong as those produced by the human brain or less than 5×10^{-18} T. They can also be used

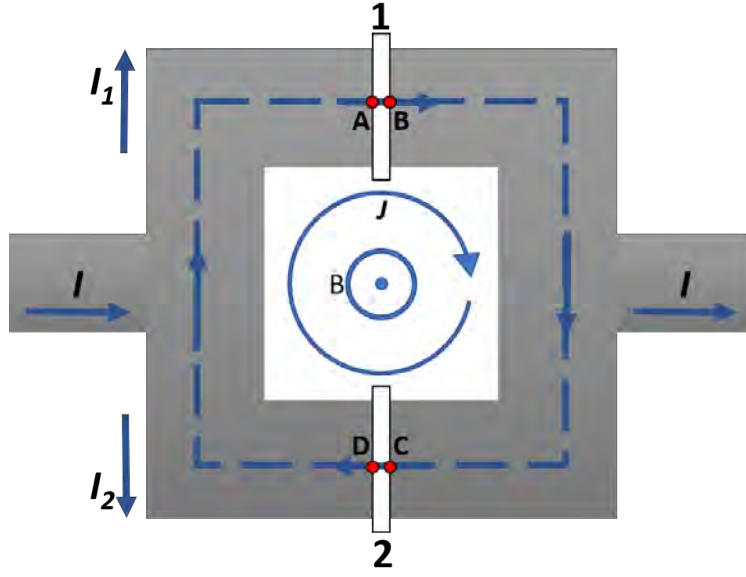


Figure 2.9: **Schematic view of a dc SQUID** Schematic view of a dc SQUID formed by two Josephson junctions in a superconducting loop driven by a current I . This current will split into I_1 and I_2 , or can equivalently be thought of as including a circulating current around the loop J . The blue dotted line indicates the closed contour integration path described in the text.

to detect things such as the cosmic microwave background radiation and nondestructive materials testing and are able to work in temperatures less than 10 K.

Figure 2.9 shows a schematic view of a DC SQUID which we will use as a model following work done previously [90,91]. The SQUID is made up a superconducting loop that has two Josephson junctions labeled 1 and 2 in the diagram. The SQUID has a current flowing through it with breaks up into two currents I_1 and I_2 . Applying what we know from the Josephson effect we can write these currents as $I_1 = I_{c1}\sin\phi_1$ and $I_2 = I_{c2}\sin\phi_2$, where I_{c1} and I_{c2} are the critical currents of the junctions and ϕ_1 and ϕ_2 are their phase differences, respectively.

Cooper pairs inside of a superconductor are represented by single-phased wavefunctions and because of this their phase can only change by $2\pi n$ around a closed loop. Using this

starting point we have,

$$2\pi n = \oint \nabla\theta \cdot d\mathbf{l} = \phi_{ab} + \phi_{bc} + \phi_{cd} + \phi_{da} \quad (2.32)$$

where we are summing up over each piece of the loop. The superconducting parts of the loop contribute two parts to the sum while the Josephson junctions give the other two parts to our sum. The relation between the phase and supercurrent density \mathbf{J}_s as well as the vector potential \mathbf{A} is,

$$\nabla\phi = \frac{2\pi}{\Phi_0} \left(\mathbf{A} + \frac{1}{\mu_0\lambda_L^2} \mathbf{J}_s \right) \quad (2.33)$$

We have the following,

$$\phi_{ab} = \phi_1 + \frac{2\pi}{\Phi_0} \int_a^b \mathbf{A} \cdot d\mathbf{l} \quad (2.34)$$

$$\phi_{bc} = \int_b^c \frac{2\pi}{\Phi_0} \left(\frac{1}{\mu_0\lambda_L^2} \mathbf{J}_s + \mathbf{A} \right) \cdot d\mathbf{l} \quad (2.35)$$

$$\phi_{cd} = -\phi_2 + \frac{2\pi}{\Phi_0} \int_c^d \mathbf{A} \cdot d\mathbf{l} \quad (2.36)$$

$$\phi_{da} = \int_d^a \frac{2\pi}{\Phi_0} \left(\frac{1}{\mu_0\lambda_L^2} \mathbf{J}_s + \mathbf{A} \right) \cdot d\mathbf{l} \quad (2.37)$$

If we consider the case where the arms of the loop are wider and thicker than the London penetration depth, and if we choose an integration path deep inside the superconductor, then the \mathbf{J}_s term is zero and the integral of the vector potential is equal to the total flux Φ enclosed.

$$2\pi n = \phi_1 - \phi_2 + \frac{2\pi}{\Phi_0} \oint_C \mathbf{A} \cdot d\mathbf{l} \quad (2.38)$$

or

$$\phi_2 - \phi_1 = \frac{2\pi\Phi}{\Phi_0} - 2\pi n \quad (2.39)$$

The total flux $\Phi = \Phi_{ext} + \Phi_{int}$ in the loop is the sum of the flux from an external field Φ_{ext} and the flux from the circulating current J and loop inductance L : $\Phi_{int} = LJ$.

$$\Phi = \Phi_{ext} + LJ \quad (2.40)$$

The circulating supercurrent is given by

$$2J = I_1 - I_2 = I_{c1} \sin \phi_1 - I_{c2} \sin \phi_2. \quad (2.41)$$

while the total current through the loop is

$$I = I_1 + I_2 = I_{c1} \sin \phi_1 + I_{c2} \sin \phi_2. \quad (2.42)$$

Combining eqs. 2.39, 2.40, 2.41 and 2.42 we have

$$I = 2I_c \cos\left(\frac{\pi\Phi}{\Phi_0}\right) \sin\left(\phi_1 + \frac{\pi\Phi}{\Phi_0}\right) \quad (2.43)$$

$$\Phi = \Phi_{ext} - LI_c \sin\left(\frac{\pi\Phi}{\Phi_0}\right) \cos\left(\phi_1 + \frac{\pi\Phi}{\Phi_0}\right) \quad (2.44)$$

where we assume both junctions have the same critical current. The maximum critical current can be found by maximizing eq. 2.43 with respect to ϕ_1 and using eq. 2.44 for ϕ_1 [92]. We now introduce the screening parameter $\beta_L \equiv \frac{2LI_c}{\Phi_0}$ as the ratio of the maximum circulating current to half a flux quantum $\Phi_0/2$. For cases where $\beta_L \ll 1$ the circulating

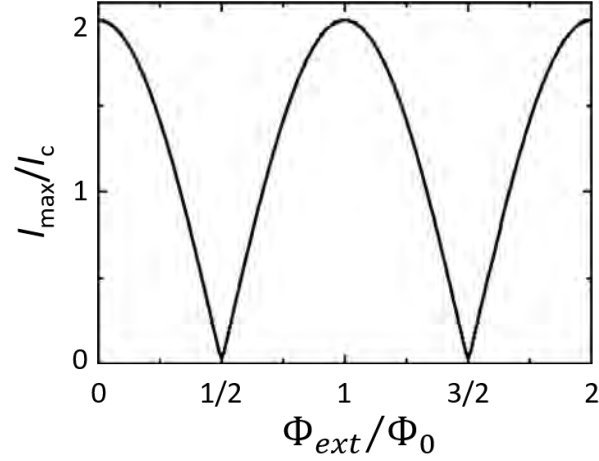


Figure 2.10: **Critical current vs applied flux for dc SQUID** Plot of critical current vs applied flux for symmetric dc SQUID. For $\beta_L \ll 1$ we see an oscillation between $2I_c$ and 0. The oscillation decreases in amplitude for larger values of β_L .

current can be ignored giving a maximum current through the device as,

$$I = 2I_c \left| \cos \left(\frac{\pi \Phi_{ext}}{\Phi_0} \right) \right| \quad (2.45)$$

Figure 2.10 shows a SQUID oscillation in a plot of I_{max}/I_c as a function of Φ_{ext}/Φ_0 . This figure assumes that $\beta_L \ll 1$ which gives the characteristic SQUID oscillation we have in our experiments.

Chapter 3

Experimental Techniques

3.1 Microfabrication Techniques

3.1.1 Photolithography

Photolithography(PL) in its simplest form is copying a pattern from a mask onto a substrate by the use of an ultraviolet light. The reason we use photolithography in our design is to pattern top and bottom leads of our junction designs on silicon substrates. Since the design of the leads doesn't have to be changed this step of the process is very reproducible. PL cannot be used to make features that are the size of our junctions so most of the features on the mask are relatively large. The process involves spinning a coating of a photoresist on top of the substrate and exposing the then baked photoresist to a UV light. There are different types of photoresist and all have specific purposes. The resist used in our fabrication process for Josephson junctions is a bi-layer(S1813/LOR5B). The bi-layer has been developed to help with the lift-off and definition of features because it can produce an undercut in the resist profile. The undercut is basically a shadow caused by a step where no deposited material can build up. For positive resist, exposure to UV light causes the photoresist to become more soluble in the developer. We also use negative resist that when is exposed causes the resist to cross-link to form a hard plastic. In either case the developer removes soluble resist defining the features from the lithography step. For our case the positive resist is the first lithography step where we use the resist to define a pattern and the metal is sputtered into

the pattern. After metal deposition, the remaining resist is removed which takes some of the metal along with it but leaves metal where no resist was present. That step is called "lift-off".

We use negative resist in our process for defining our junctions. The negative resist creates a hard plastic on top of the already deposited metal to protect it from chemical etching or ion milling. The negative resist protects the metal underneath it, so the ion mill etches away any metal not covered by the resist. Once the pattern is etched away the resist left on top of the remaining metal is removed.

3.1.2 Electron Beam Lithography

Electron beam lithography(EBL) is used as a small feature writing process. The features we write are on the order of a few tenths of a micron. Similarly to the PL the EBL uses resist to form patterns over a substrate. The difference here is that we have the ability to change the pattern anytime we write. The shape of the junctions can be altered from sample to sample to change their characteristic behavior. The EBL exposes the resist to highly energized electrons that causes the same cross-linking of the resist to form a plastic. The development process then follows to define the pattern written with the electron beam.

3.1.3 Sputtering

Sputtering involves highly energized atoms hitting a target surface causing the target atoms to be knocked off and deposited on a substrate. First we need to create a plasma from argon atoms. To create a plasma the neutral argon atoms are bombarded with electrons emitted from a tungsten filament, which knock off an outer electron causing the argon atom to carry a net positive charge. There is an electric field applied in the plane of the target

which will be called axis one for reference. A magnetic field generated by two permanent magnets points in the plane of the target but perpendicular to the electric field. The magnetic field causes the electrons to spiral according to their cyclotron frequency, making electron-argon collisions more probable. The ionized atoms are now attracted to the cathode that is held at a negative potential. The target is mounted on the cathode and the ions bombard the target surface knocking off (sputtering) atoms from the target, some of which land on the sample substrate. The target voltage is kept constant during the sputtering run and is unique for each target.

3.1.4 Ion Milling

To ion mill first we need to create a plasma. The plasma is created in a manner similar to what happens in the triode sputtering guns above. A magnetic field is applied perpendicular to the electric field, which applies a Lorentz force on the moving electrons causing them to spiral according to their cyclotron frequency, making the electron-argon collisions more probable. The ionized atoms are now accelerated to the grid (cathode) and out towards the sample. Before they reach the sample the ionized atoms pass through a neutralizer. The neutral argon atoms slam into the sample colliding with and knocking off atoms from the sample.

3.2 Magnetic characterization

An important first step in our research is to characterize the magnetic behavior of our samples since the relative orientation of the magnetic layers dictates the results of our electronic transport measurements. There are two measurements that we perform using a Quantum Design MPMS3 SQUID Magnetometer, magnetization vs. temperature and magnetization

vs. field, to characterize our samples. The first measurement is used when we want to find the transition (Curie) temperature of a given sample/material. The second measurement can probe information like switching behavior and saturation magnetization. Initial measurements are performed on films to get a general idea. If further investigation is needed the films can be patterned into arrays of nanomagnets with the same dimensions as our junctions. The sputtering of the films follows the same steps as the sputtering of the bottom leads. The only difference in the sputtering is that the photolithography step is not present for the magnetic films. After sputtering, the samples are brought out of the clean room and cut into four pieces taking care that they do not come into contact with anything magnetic. Samples are loaded into plastic straws and placed into the MPMS3 for measurement.

Arrays: The arrays are needed when we want to determine the switching behavior that will occur for the magnetic layers in our Josephson junctions. Starting with the magnetic films we must now pattern an array of pillars using EBL. Like the EBL procedure with our samples, starting with samples coated with e-beam resist, we use a diamond scribe to make a scratch mark near the corner of the substrate through the magnetic film. This scratch mark is used for focus and stigmation in the SEM. The writing script starts from the scratch mark and the stage moves away from the mark to the center of the array. The move places the mark outside of the writing area. Our standard array dimensions are 4.5mm in height and width. The array is developed using AZ-300MIF then rinsed with deionized water. The next step is to ion mill the array. We load the samples into ion mill holders using masks that have the largest cutout to mill as much of the film as possible. The less film left after ion milling the less magnetic residue will be left after processing. The ion mill is directed perpendicular to the surface. After ion milling we must prepare the array for dicing by spinning and baking photoresist on the array, for protection during dicing, and the chip must also be glued to a

sacrificial wafer. A few drops of photoresist are placed and spread thinly on the wafer where we plan to place the substrate making sure to press down on the corners of the sample. The wafer is then placed on a hot plate at 110 Celcius for an hour. The wafer is then brought out to the dicer and aligned and the arrays are diced into 6x6mm squares. For dicing we use the diamond blade to minimize magnetic contaminants left over from the blade. The arrays are diced completely through since they are attached to the wafer. We now take the wafer back into the cleanroom in preparation for removal of the resist. Acetone in a wafer beaker is warmed to 110 Celcius and the wafer is placed into a beaker for 20 minutes. We rinse off the acetone residue with IPA followed by DI water. For our measurements we want to look at the switching characteristics in both the easy and hard axis of the array. Using a diamond scribe, we label the easy axis on the back of the samples for orientation during measurement.

3.3 Josephson Junction Fabrication Procedure

3.3.1 Sample Preparation

Starting with a three-inch single-side polished silicon wafer in a class 100 cleanroom we spin photoresist in preparation for dicing. The resist protects the substrate during the dicing process and also keeps the surface clean from contaminants since the dicing is done outside of the cleanroom. After placing the wafer onto a Headway resist spinner we dispense S1813 photoresist from a disposable pipet onto it. The wafer is then spun at five thousand revolutions per minute for fifty seconds to create a uniform layer of photoresist. The wafer is then placed on a hot plate for two minutes at ninety degrees Celsius. The wafer is now brought out of the cleanroom and diced into 0.495 inch squares (chips) using an ADT wafer

dicing saw. Approximately eighteen chips can be diced out of one wafer. The dicing saw is programmed to cut into the wafer leaving only five thousandths of an inch of the wafer remaining. After dicing we take the wafer back into the cleanroom and label each individual chip using a diamond scribe with a distinct number according to the location in the sputtering chamber. The chips are held by the corners to prevent scratches near the areas of interest. The chips are cleaned by first holding them over a waste beaker with tweezers and rinsing the bulk of the resist using a wash bottle filled with acetone. The chips are then placed into individual test tubes that are half filled with acetone that has been warmed to 70 Celcius using a beaker water bath. The chips stay in the warm acetone for ten minutes with ultrasonic agitation on high. The chips are now rinsed with Isopropanol(IPA) to remove any acetone residue. The IPA is followed by a rinse in deionized water (DI) which is blown dry using nitrogen and wicked from the edge of the chip by cleanroom wipes. The chips are now placed into an oxygen plasma etcher for ten minutes at 300 watts after the plasma etcher was pre-cleaned by running empty at 300 watts for ten minutes.

Figure 3.1 shows a cartoon representation of the Josephson junction fabrication process. Each step is discussed in the following sections in detail. The layers in this representation correspond to materials that we can sputter in our chamber. These materials are named in the sputtering chamber section below.

3.3.2 Photolithography: setup and bottom lead deposition

Starting with the previously cleaned chips we first bake them at 110C to remove any residual water. After letting the substrates cool, one at a time, they are placed on a Headway resist spinner that is set to 3000 RPM and 45 seconds spin duration. After setting the correct spin speed we place the chip on the spinner and use a nitrogen gun to blow off the surface of

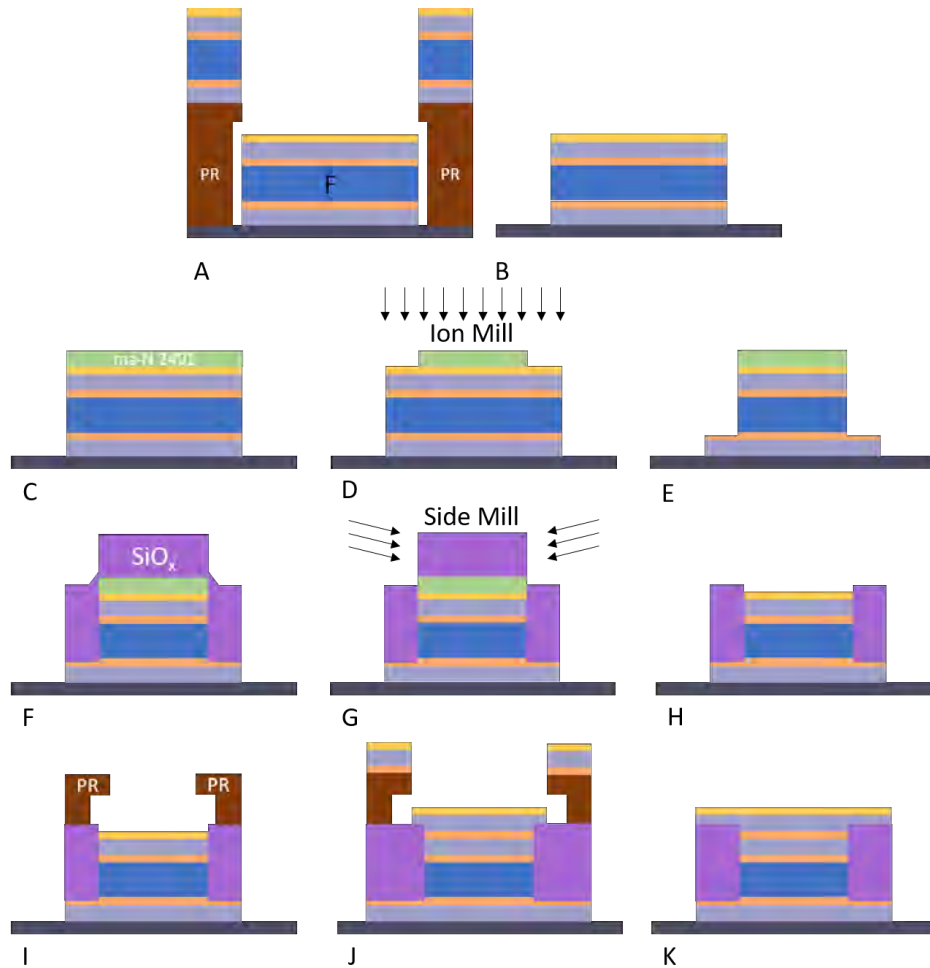


Figure 3.1: *Fabrication Process*: Diagram of fabrication process: A. Bottom lead lithography and deposition of metallic multilayer. PR is the bi-layer photo resist. B. Bottom lead liftoff C. Sample coated with electron beam lithography resist. D. Ion milling E. Patterned junction. F. Silicon Oxide deposition G. Side mill of silicon oxide H. Junction liftoff I. Top lead photolithography J. Top lead metal deposition K. Top lead liftoff

the chip. Using a disposable pipette we fill from the center of the resist bottle to avoid any possible contaminants from the surface. For our bottom lead we use a bi-layer to provide an adequate undercut. The first photoresist we spin is LOR5A, followed by S1813-G2. Holding the pipette directly above the center of the chip, dispense enough resist to cover the center while avoiding air bubbles from forming. Start to spin immediately after the resist settles. Place chips on an aluminum foil tray and into an oven for 45 minutes at 180C. After allowing the chips to cool repeat this process for S1813-G2 changing the spin speed to 5000 rpm for

50 seconds. To remove the solvent from the photoresist we bake the samples in an oven for 45 minutes at 110 Celcius. Before alignment the underside of the samples must be clean. A swab with acetone can be used to remove any baked-on resist from the back of the chip. This step is done to ensure a clean surface for the vacuum chuck in the ABM mask aligner to securely hold the substrate in place during alignment. Since the sample is held at the center of the chuck, rotation adjustments are about the center of the sample. Alignment is done using the edges of the chip. We expose the chips for 4.5 seconds. The developer used is MF 319 and is done for 45 seconds followed by a rinse with deionized water. The last step of the process is a plasma descum at 100 watts for 2 minutes right before loading the samples into holders.

3.3.3 Sputtering Chamber

Once the substrates have gone through the photo-lithography process we load them into aluminum sample holders. The holder has a stainless steel shutter with a single square cut-out that allows one sample to be exposed to sputtering at a time. The holders are cleaned before each sputtering run. Cleaning involves placing the shutters into a solution of one part deionized water to three parts nitric acid for thirty minutes and rinsing thoroughly with DI water. The shutters and aluminum parts are scrubbed to remove any residual metal with wire brushes and DI water. All parts are then placed into a beaker that is filled with acetone and placed in a sonication bath for five minutes. The sonication steps are repeated for ethanol and DI water. The parts are dried with a heat gun and placed into resealable zipper bags.

Each holder has openings for two substrates and each substrate is held in place by a copper heatsink. The samples are loaded into the holders in a class 100 room. Each holder

is labeled as “1” through “8” and individual samples are marked as “A” or “B” for sample identification. Place samples into holders while keeping the shutter opening always oriented towards the top of the holder relative to labeling. While loading the samples and to measure their temperature a thermocouple is mounted directly on a heatsink holding a sample using a screw as a mechanical anchor to keep it in place. Each sputtering run can have up to seven different sputtering guns, four 2 1/4 inch triode guns and three 1 inch magnetron guns. For the triode guns, ferromagnetic targets are soldered to a copper base using indium to prevent them from moving due to permanent magnets near them. The magnetron targets have silver paste on them and are held down with the gun parts. To avoid cross contamination each of the sputtering targets has its own parts that are kept with their corresponding targets. The sputtering chamber usually reaches a base pressure of 2×10^{-8} torr after baking the chamber for eight hours and after opening it to a cryopump for the following day. During the sputtering run, to further help lower the base pressure, we use a cold trap to freeze any possible water still in the chamber. Passing argon through a purifier we now introduce the gas into the chamber and control the pressure with the gate valve to the cryopump to a pressure of 2.3×10^{-3} torr for sputtering. The targets are water-cooled throughout the run and have interlocks that prevent switching on the targets without proper cooling. The plasma power supply is switched on followed by the target power supply and target controllers. For magnetic targets the voltage and current values are much higher when compared to non-magnetic targets. The voltage and current are slowly increased, fifty volts every thirty seconds, to avoid damaging the gun filament. Once the voltages are set we begin to measure sputtering rates using a film thickness monitor. When sputtering niobium we have the target on for thirty minutes prior to sputtering to coat the walls and act as a getter.

When we are done depositing the niobium we shut down the sputtering system according

to the shutdown procedure. The chamber can be left to warm up slowly overnight. If the samples are needed quickly we can warm up the chamber to room temperature using the heat strips to have the samples ready for liftoff in about 2 hours. The samples are removed from the sputtering chamber and placed into a ziplock bag. The samples are taken into the cleanroom to begin the lifoff process. To lift-off the photoresist we first remove most of it by rinsing the sample with Remover PG over a waste beaker. The sample is then placed in test tubes partial filled with Remover PG that have been warmed to 90 Celsius for 30 minutes and are sonicated for 2 minutes. The chips are then rinsed with IPA followed by a rinse with DI water. Verification of the lift-off process is done with an optical microscope.

3.3.4 Electron beam lithography-EBL

Once the bottom lead has been sputtered and we have processed the sample through lift-off we can now move on to the EBL process. In this step of the fabrication we are defining the shape of the junctions using a negative electron beam resist (ma-N 2401). This resist acts as a mask protecting everything that is underneath it. In the class 100 room the samples that have bottom leads are placed into the oxygen plasma etcher for a descum at 100 watts for 2 minutes. Once the samples are cool they are placed on the resist spinner that has been set to 3000 rpm for 40 seconds. The e-beam resist is dispensed from a disposable pipet onto the sample at the center of the chip avoiding any formation of bubbles. The samples are then baked on a hotplate for 60 seconds at 90 Celsius. The samples are now placed on the holder along with a stigmation sample. In preparation for ion milling we load five samples at a time for e-beam lithography to avoid having samples with e-beam resist on them for an extended period of time. Remembering to place the samples in the correct orientation for writing we take an optical image for ease of alignment using the SEM software. The height

adjustment for both holders made at MSU is 2mm. Following standard loading procedure the samples are loaded into the SEM. After turning on the beam, we move towards the center of the stigmation sample to begin our calibration procedure. The focus and stigmation is done on small circular gold features found on the alignment marks of the stigmation sample. The initial alignment is done at high magnification at a working distance of 15 mm. The following steps should be done with care not to expose the region of interest. Once we are done with the stigmation sample we go to the lowest magnification and move towards one of the pads of the bottom lead of our first chip. Using the vertical alignment tool on the SEM toolbar we align to the edge of the pad for writing (a slow, high resolution scan is useful for this step). Now we move near the area of interest and focus on one of the alignment marks next to the writing area at 60x magnification. Zooming out completely we move over the writing area then switch to EBL mode and align the sample using an alignment script in NPGS. Writing is done at 1000x magnification. Our current samples have three writing areas so focusing is done three times per sample. For development we use AZ300MIF developer for 30 seconds followed by a rinse in DI water. Verification of the lithography is done with an optical microscope.

3.3.5 Junction definition by ion milling

After writing features with EBL we are ready to pattern using the ion milling process. This step involves the use of two different holders during this process. The first sample holder allows the milling to occur perpendicular to the plane of the sample. This step etches the features from the bottom lead removing all but what is underneath the e-beam resist. We first place a stainless steel mask that covers part of the sample, exposing only the area near the e-beam resist to the mill. Stainless steel is used for the mask because of its low

etch rate. The sample is placed face down, directly on the mask. We apply a thin layer of silver paste to the back of the sample to provide good thermal conductivity aiding in keeping the sample from getting overheated during the milling process. The silver paste layer must be thin enough so as not to spill out onto the edge or face of the sample. Following the silver paste is a brass or copper heatsink. Some samples need a copper spacer to fill in the space between them and the heatsink. The parts are held together with bolts and a metal plate sandwiching all the parts together. The plates are labeled for identification during the milling process. The holders are loaded into the milling chamber, one at a time through a loadlock, purging with nitrogen between each opening and keeping track of the order of the holders for identification during the process. Pumping down the chamber for one day gives a base pressure of about 3×10^{-8} Torr. In preparation for milling we turn on power supplies for ten minutes prior. To calibrate the mill rate we must first deposit gold on a film thickness monitor (FTM). Argon is allowed to enter the chamber and using a turbo pump we tune to a pressure of 0.7 mTorr . To measure the mill rate, we place the FTM over the ion mill before each sample is milled keeping track of how much gold is left after each for the rest of the samples. Most samples need different mill times since the thicknesses of layers vary from sample to sample. Now we are ready to start milling and the chamber pressure is set to 0.19 mTorr using the turbo pump. Once the power supply is stable we open the shutter to the FTM and begin to measure a milling rate. The milling value is recorded and using the thickness for each material along with the k-factor we calculate the mill time for the corresponding sample. The k-factor corresponds to the ratio of milling rate of gold compared to the material of interest. The sample is now placed over the ion mill for the appropriate amount of time then the shutter is closed off once the time has elapsed. The steps are repeated for all samples and once completed we shut off the ion mill power supply

and argon gas. If the mill time exceeds 2 minutes we break it into parts.

The silicon oxide power supply is turned on and slowly brought up to the optimal voltage in 5 mV steps. The preferred deposition rate is near 7 angstroms per second. We want to protect the exposed areas with silicon oxide to prevent shorts from overlapping areas between the top and bottom superconducting electrodes. The rate is measured with the FTM making sure the value is set for silicon oxide. The sample is placed over the silicon oxide and spun continuously in order to have a uniform insulating layer. After milling the samples we take them back into the cleanroom and clean off the silver paste using a cotton swab and acetone. The samples are then placed into side mill holders making sure to have the bottom lead directed along the opening of the holder. Following the same steps as before we measure the rate of the ion mill and mill each side of the sample for four minutes on each side. The samples are rotated by 180 degrees to mill both sides of the sample. The side mill step is in place to help with the liftoff of the e-beam resist. Images before liftoff are taken with an optical microscope using manual settings for comparison. Samples are placed in Remover PG that has been warmed to 90C, for 10 minutes followed by a mechanically-assisted liftoff with a Q-tip. The samples are placed in the warmed Remover PG for 1 hour. After an hour we rinse the samples with DI water and verify that the pillars have had a successful lift off using an optical microscope. Once the steps are completed we are ready for the top lead lithography.

Arrays: For fabrication of arrays some different steps need to be taken. The arrays are written on unpatterned magnetic films. The film must be marked first in order to align, focus and stigmatize. The mark is done near a corner with a diamond scribe. The EBL array writing file will include an offset for centering the array. Once the ion milling is done the liftoff procedure may leave some resist on the tops of the pillars. The substrate must be

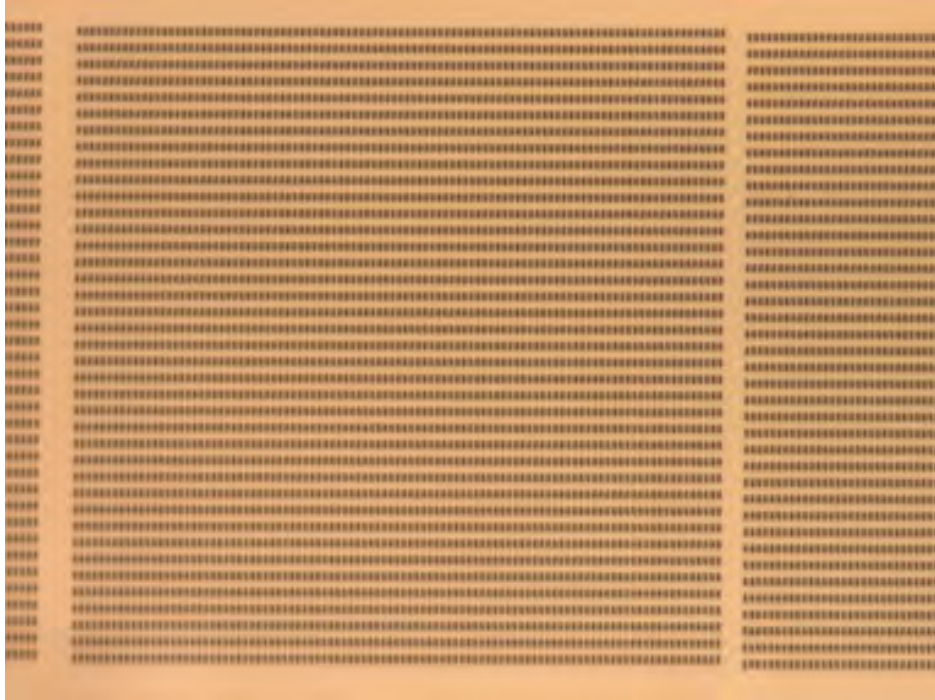


Figure 3.2: *Junction Array*: Optical microscope view of array of elliptical nanomagnets patterned with electron beam lithography. The pattern shown contains 99x39 nanomagnets, and is repeated 45 x 55 times to form the entire array.

attached to a large wafer for dicing out the array. The attaching of the substrate is done by wetting the back of the sample with photoresist and baking at 90C for 1 hour. The wafer with the sample is then spun to coat completely with photoresist and baked at 110C for 2 hours. The dicing is done by aligning to the edges of the array, which should be visible in the dicing saw.

Figure 3.2 is an optical image of one of our lithography patterns of arrays. The bits seen in the image are the same size as the junctions patterned in our samples. The pattern is 99x39 bits repeated 45 x 55 times. The arrays give us approximately 9.5 million bits. The write time for a whole array is 12 hours. The reasoning for having so many bit is to produce a signal strong enough to be measurable by the SQUID magnetometer.

3.3.6 Top lead

For the top lead photolithography we follow the same steps as before but the alignment is done using the markers from the bottom lead. The initial vertical, horizontal and rotational alignment is done using the marker near the center of the sample. The rotational alignment is done using the outer markers. As the mask is brought into contact the tilt adjustment must be held down to ensure full contact with the sample. We check the alignment once again to make sure nothing has shifted after full contact. The alignment must be checked after the development step to check for the correct overlapping of the leads. Two sputtering targets are used for the top lead sputtering process, niobium and gold. Before depositing the top leads, we use a small ion mill to clean off the capping layer of gold covering the niobium from the bottom lead. Each sample is milled just before the top lead niobium is deposited to minimize any possible oxidation of the niobium. The top lead is 150 nm of niobium which is once again capped with gold.

3.4 Measurement

3.4.1 Setup and mounting

Once we have completed the fabrication of our samples and have taken images of them using the optical microscope we take them into our measurement room. The first step is to check resistance values of the junctions using a two terminal measurement using a standard voltmeter. The sample is placed on a copper base, for stability, with a vacuum to hold it in place. Our typical resistance values for junctions are on the order of tens of mOhms when dipped but at room temperature using a two wire terminal measurement we get resistance values on the order of hundreds of kOhms due to the long Nb leads. We also check the

resistance along the top and bottom lead respectively. We prepare the sample for mounting on a quick dipper by pressing indium on each pad to be used as a mechanical anchor for electrical connections. The indium should be higher towards the center of the pad to give a place for the wire to be pressed into. The wire is placed on the center of the indium and a stub point is used to press the wire into the indium. The sides of the indium are rolled over the wire to help hold it in place. With the wire pressed, we place a small piece of indium on top and press it forming a sandwich securing the wire to the pad. These steps are repeated for all the pads keeping in mind that pressing indium on pads after dipping does not adhere as well as pressing them before dipping. Once all the connections are made to the quick dipper we secure the sample using some thread by wrapping it around the dipper's brass base and the sample. Resistance measurements are made through triax connections on the top side of the quick dipper to ensure proper wiring. The final step in the setup process is to place the mu-metal sheath over the sample area and secure it set screws. The mu-metal sheath is used to prevent external magnetic noise to alter our measurement process. The dipper is slowly lowered into the dewar to avoid excessive boiling off of the helium. The lowering time depends on the specific dipper that is being used.

3.4.2 Single junctions

There are two types of transport measurement systems in the lab. For samples with large critical currents, more than a few microAmps, we use a room temperature electronics system that can measure up to five samples every cool down. For samples with small critical currents, in the microAmp range, we use a measurement system that has low-temperature SQUID electronics and can measure one sample at a time. The first measurement taken is for optimizing parameters as the sample is in the virgin state. The virgin state measurement

is taken without applying an external magnetic field and is taken at zero field. For samples that contain nickel as one of the ferromagnetic layers, before the measurement, we must initialize at high field in order to push out all domain walls. If the initialization field is higher than 1200 Oe (Ni is initialized at 3000 Oe), we must remove magnetic flux trapped in the superconducting leads after the large field is applied. To remove trapped flux we must lift the dipper out of the liquid helium in order to have the niobium leads go normal. We take a resistance measurement through the sample using an Ohmmeter as we raise the dipper out of the liquid helium. The sample resistance will show a non-zero value when the sample goes normal. When the sample has gone normal we disconnect the Ohmmeter and wait for 10 seconds before lowering the dipper into the liquid helium again. To start taking measurements we make the field sweep start from the same direction as the initialization field. For these measurements the data is processed with a fitting program that fits the I-V curves to a square root function that gives the critical current for each magnetic field measurement.

3.4.3 Phase Sensitive Measurements-Superconducting Quantum Interference Device (SQUID)

The further characterization of our junctions is done by phase sensitive measurements. We fabricate a SQUID loop with two of our Josephson junctions along with an on-chip flux line. The flux line generates a local magnetic field that couples flux through the SQUID loop. The connection and mounting procedure is the same as the single junction procedure. For these measurements the external magnetic field is used to set the direction of the magnetization of the ferromagnetic layers in the junctions before the measurement. The external field is off during the experiment as we step through the flux line recording a SQUID oscillation. Depending on the relative orientations of the layers we can see shifts in the SQUID

oscillation plots.

3.5 Improvements to measurement and fabrication systems

During my time in the Birge group, as a part of the thesis work, I made several contributions to the development of shared infrastructure in the lab. This work involved improvements and added functionality to measurement equipment, measurement software and a new high-vacuum sputtering chamber named the “Rezanator”.

3.5.1 Room temperature electronics:

- **Built System** Wiring and testing of new electronics
- **Created measurement software** Using previous versions of software a new version was created
- **Measurement improvements** Added faster data acquisition by adjusting measurement parameters
- **Programmed Arduino micro-controller** Persistence switch controller was made using an Arduino micro-controller

3.5.2 Low temperature electronics:

- **Measurement speed improvement** Adjustable measurement parameters to improve speed of data acquisition
- **Added measurement features** Added time delay, major/minor loops, SQUID data formatting for easy plotting and repeatable loops for toggle switching

3.5.3 Rezanator and sputtering chamber:

- **Helped develop co-sputtering capability**
- **Ion mill characterization** Helped characterize and profile new ion mill for rotating sample
- **Made indexing arm attachment** Designed and machined indexing attachment for linear arm
- **Helped design hand-off system** Helped with the design and fabrication of the hand off system (motor holder, motor spindle, sample holder and Arduino motor controller with Labview controller software)
- **Pratt sputtering chamber** Added ion mill and gun 7 to the sputtering software

Chapter 4

Shuffled and Triplet Josephson junctions

In this chapter we compare two types of Josephson junctions that contain the same ferromagnetic layers but in different orders; we will call them “triplet” and “shuffled”. Both types of junctions contain three distinct magnetic layers. The triplet junctions are made up of two Ni layers that are either 1.2 or 1.6 nanometers thick. Between the two Ni layers is a Pd/Co multilayer that can vary in number of repeats. The shuffled junctions contain the same magnetic layers but the two Ni layers are now adjacent to each other followed by the Pd/Co multilayer. The junctions can either propagate spin triplet supercurrent or spin singlet supercurrent. In Section 2.4.3 of Chapter 2 I discussed how short-range spin-singlet pairs can be converted to long-range spin-triplet pairs in Josephson junctions containing three ferromagnetic layers, where adjacent layers have non-collinear magnetizations. The Pd/Co multilayer used in this chapter has perpendicular magnetic anisotropy (PMA), whereas the two Ni layers have in-plane magnetic anisotropy, so sandwiching the Pd/Co between the two Ni layers enables the generation of spin-triplet supercurrent. Shuffled junctions, because of the the order of the magnetic layers, can only generate spin-singlet supercurrent.

Joseph Glick, former Birge group graduate student, first studied spin-triplet junctions that contained Pd/Co multilayers with perpendicular magnetic anisotropy(PMA), but his PMA layers were arranged as synthetic antiferromagnets (SAFs), i.e. two PMA multilayers sandwiching a thin Ru spacer layer so that their magnetizations are coupled antiparallel to each other. Joseph found that triplet junctions containing a PMA-SAF had a somewhat

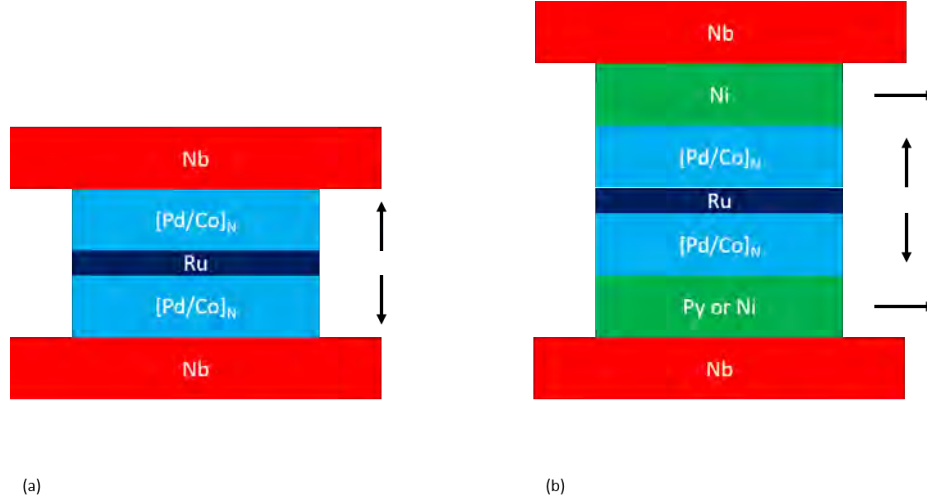


Figure 4.1: *Singlet and Triplet*: Side view of general singlet (a) and triplet (b) Josephson junctions, where the middle layer has the form of a PMA-SAF with out-of-plane magnetization. The Ni or Py layers in the triplet have in-plane magnetization. All the magnetic layers are separated by Cu spacers (not shown) to prevent magnetic coupling between adjacent layers.

shallower decay of their $I_c R_n$ product as a function of Pd/Co repeats when compared to his singlet junctions. That was expected since spin-triplet pair correlations should be long range in the Pd/Co multilayer, whereas spin-singlet correlations are short range. Joseph also found that for the thinnest PMA-SAF triplet junctions, junctions with the least number of repeated Pd/Co layers, the critical current was smaller than in similar PMA-SAF singlet junctions. That was puzzling, but a direct comparison between those types of junctions was not meaningful because the spin-triplet junctions contained two additional magnetic layers compared to the spin-singlet junctions. The motivation for the work described in this chapter is directly related to Joseph results. Our goal is to determine how much spin-singlet supercurrent propagates through the spin-triplet Josephson junctions. We do that by comparing the magnitude of the supercurrent in spin-triplet and shuffled junctions that contain the same number and kind of magnetic layers, but in different sequences.

Figure 4.1 shows magnetic layers in both singlet(a) and triplet(b) Josephson junction

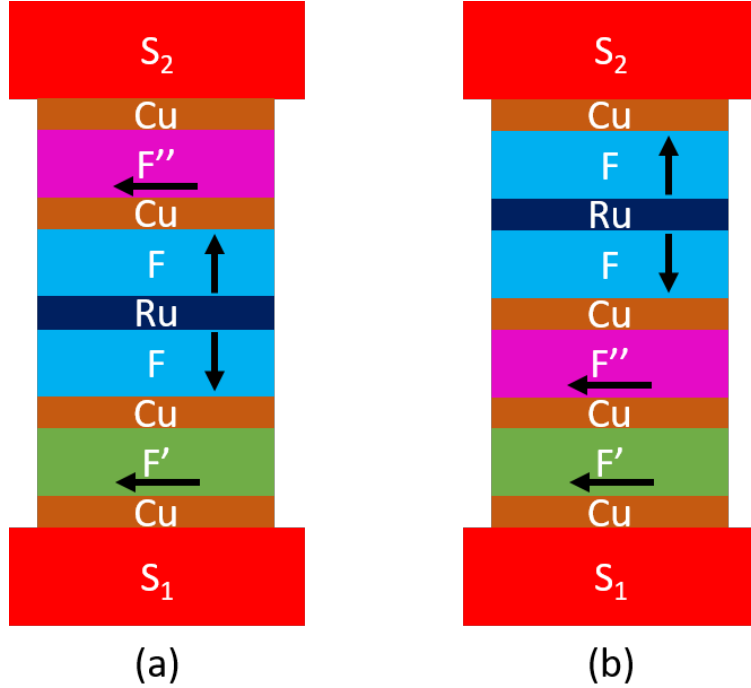


Figure 4.2: *PMA-SAF and Shuffled junctions*: Side view of the triplet (a) and shuffled(b) PMA-SAF Josephson junctions.

configurations. The singlet junction on the left contains a PMA-SAF while the triplet on the right has two Ni layers with the same PMA-SAF layer sandwiched in between them. An important property of the PMA-SAF is that it minimizes stray fields that might interfere with the behavior of our Ni layers. The directions of magnetization in the figures are labeled only for reference – they may be flipped by 180° .

Figure 4.2 shows a side view schematic of both the triplet junction (a) on the left and shuffled junction (b) on the right. For S_1 , we use a Nb/Al multilayer because it provides a much smoother surface than a pure Nb layer of the same thickness. The magnetic layers are separated by Cu spacers to prevent magnetic coupling of adjacent layers. The first F' layer, Ni in this case, is sputtered before any other ferromagnetic layers and directly on the Cu spacer. For the triplet junctions the next layer deposited is the PMA-SAF layer and for the shuffled junctions it is another Ni layer. Finally we have the remaining layer, Ni for the

triplet and the PMA-SAF for the shuffled junctions. The final step is to deposit a thick Nb top lead.

For the triplet junctions the first Ni layer allows the conversion of singlet ($s = 0$) pair correlations to short-range triplet ($s = 1, m_s = 0$). The PMA-SAF converts the short-range triplet to long-range triplet ($s = 1, m_s = \pm 1$) pair correlations. The final Ni layer converts back to singlet pair correlations which can enter back into the other superconducting electrode, thereby allowing the propagation of the supercurrent through the junction. Looking at the shuffled junction geometry we can clearly see that although we do convert to long-range triplet pair correlations we never convert them back into singlet pair correlations. This means that only spin singlet supercurrent can propagate through this type of junctions.

4.1 Magnetic characterization of Pd/Co multilayers

The first step of the process was to understand the magnetic behavior of the ferromagnets that we would like to use as the central ferromagnet in the junction stack. The selection of Pd/Co multilayers as the central layer was done in order to take advantage of their out of plane magnetization. The Pd/Co multilayer system can have either an in-plane or out-of-plane (OOP) magnetization, depending on the thicknesses of the individual Pd and Co layers. We have fabricated and measured Pd/Co multilayers of varying thickness to produce a stack that will have an out of plane magnetization relative to the substrate surface. We first need to find the correct thickness and verify that the multilayers are indeed magnetized out of plane. We also would like to know the strength of the magnetization of these multilayers. We begin by sputtering thin films of both PMA and the PMA-SAF magnetic layers on substrates that were prepared for sputtering using the cleaning process described in the

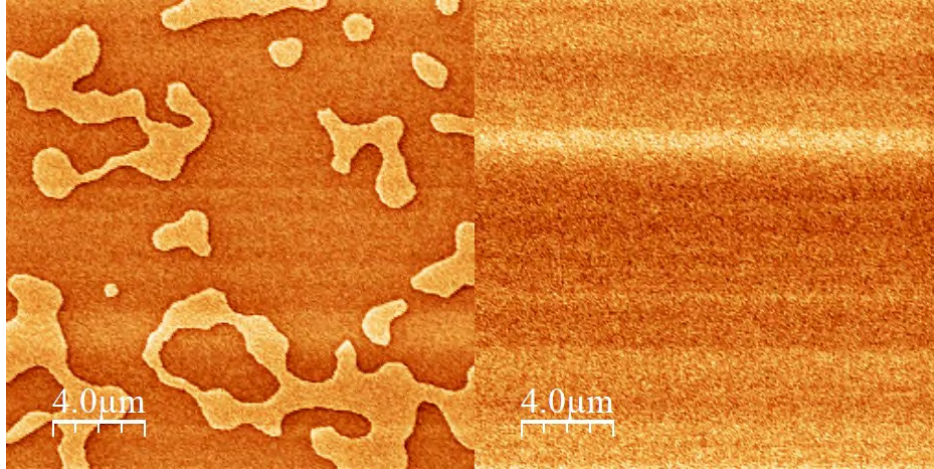


Figure 4.3: *Magnetic force microscopy of Pd/Co multilayers*: Top down view of Pd/Co multilayers imaged through a magnetic force microscope. Left image: virgin state, right image: after application of and removal of a magnetic field applied out of plane.

experimental techniques chapter. Samples that are sputtered for magnetic measurement are placed directly into substrate holders without a mask or lithography step. The shutter on the substrate holder provides almost complete exposure, when opened, to the sputtering guns. Samples were first grown looking specifically at the Pd/Co multilayers. We grew samples with varying number of Pd/Co repeats. A thin layer of Nb is deposited on the substrate which gives the following layers better adhesion to the substrate. Samples are grown at -20 Celsius just as the junctions.

Once the samples are sputtered we unload them in a class 100 clean room and load them into vials for measurement. Some of the samples were measured in a magnetic force microscope. The MFM scans the sample and images the domains in the multilayer that are aligned OOP. Figure 4.3 shows two MFM images of the Pd/Co multilayers measured after sputtering. The image on the left was measured as grown directly from the sputtering chamber. The image show the domains can vary greatly in size and shape leading to a very disordered structure. The image on the right is the same film after we applied a field out of plane to align all the domains in the multilayer. This image on the right shows that after

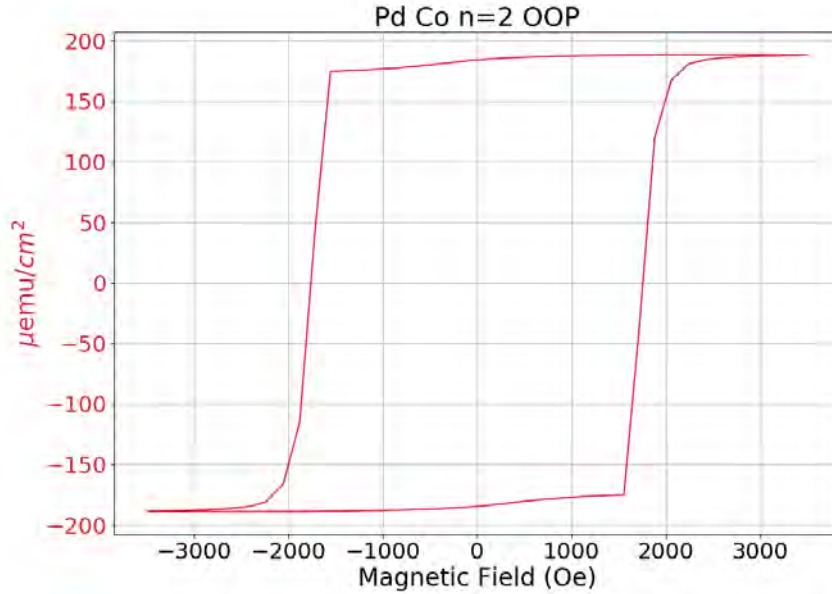


Figure 4.4: *Pd/Co multilayer thin film out-of-plane Moment vs. Field Plot*: Hysteresis curve of Pd/Co multilayers measured out-of-plane. Clean switching is observed at a field of about 1500 Oe. Saturation occurs above 4 kOe.

magnetizing the domains OOP they stay in that configuration.

The remaining films were measured using the MPMS3 SQUID magnetometer. The substrates that we dice measure $0.5 \times 0.5 \text{ in}^2$. To measure the samples with the SQUID they need to be placed into plastic straws first. The substrates are scribed into four pieces and broken along the scribe marks. Because of the strength of the magnetic material we only need to place two of the quarter pieces into the straw. They are placed back to back and pressed into the correct position in the straw. The centering of the samples is done at 10K. The sequence file we use for the measurement steps through a series of magnetic fields while the magnetic moment of the samples is measured. For the PMA samples we measured magnetization (M) vs. field (H) with the field oriented both in plane and out of plane. This measurement also tells us the initialization field needed to align the magnetization out of plane.

Figure 4.4 shows a hysteresis curve where the applied field is oriented out-of plane with

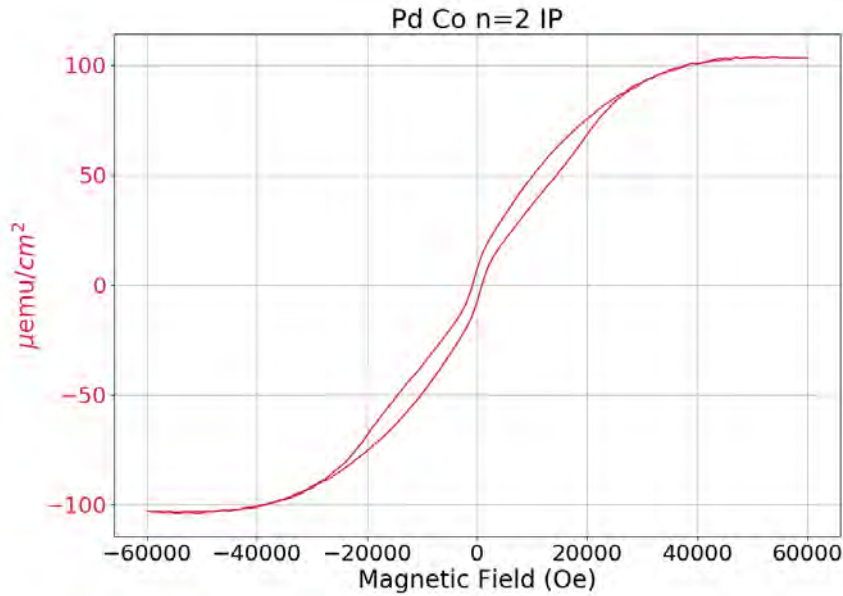


Figure 4.5: *Pd/Co multilayer thin film in-plane Moment vs. Field Plot*: Hysteresis curve of Pd/Co multilayers measured in-plane. Gradual switching is observed. Saturation occurs at about 50 kOe.

respect to the substrate. The figure shows that at large applied field the multilayer is fully saturated, and as the applied field is ramped down to zero the magnetization stays saturated. The magnetization stays saturated even as the field switches into the opposite direction, until the magnetization begins to switch at -1500 Oe. Figure 4.4 shows that the field needed to initialize the PMA layer is small enough so that it can be done at room temperature with a permanent magnet. The figure also shows us that the PMA system is very rigid and switches cleanly when initialized in the opposite direction. The plot shows a clean switch of the PMA layer near 1500 Oe.

In Figure 4.5 we have a hysteresis curve of a Pd/Co multilayer with the magnetic field applied in the plane of the substrate. We see a slow, almost linear, reversal of the magnetization with field. The magnetization saturates at -50 kOe. Figure 4.5 show that after a large IP field is applied and removed there is very little remnant magnetization. These

hysteresis curves give us a clear indication that the Pd/Co multilayers exhibit perpendicular magnetic anisotropy (PMA). Figure 4.5 also reveals that we can apply large in-plane fields to manipulate the Ni layers without worry of ruining the out-of-plane magnetization of the Pd/Co multilayer. The Pd/Co multilayer is very rigid in this system of 2 repeated layers.

Another important property that we take advantage of in these junction is that we can grow a thin layer of ruthenium between the Pd/Co multilayers at certain thicknesses which causes the magnetic layers to couple antiferromagnetically and create a synthetic antiferromagnet (SAF). The reasoning behind the use of PMA-SAF's as one of the magnetic layers is to minimize stray fields that can interfere with the behavior of our Ni layers. Figures 4.4 and 4.5 all are measurements of PMA films. For similar magnetic measurements of PMA-SAFs please refer to Figure 8.2 in Joseph Glick's dissertation [93].

4.2 Fabrication of junctions containing Pd/Co

The next step in the experiment was to fabricate junctions that were identical except for the central ferromagnetic layer where we have the following differences, S/Cu/Ni/Cu/[Pd/Co]_n/Ru/[Co/Pd]_n/Cu/Ni/Cu/S (triplet) and S/Cu/Ni/Cu/Ni/Cu/[Pd/Co]_n/Ru/[Co/Pd]_n/Cu/S (shuffled). Note that the first S at the bottom of the stack is a [Nb/Al] multilayer, whereas the top S is pure niobium. These Josephson junctions contain some of the most complicated stacks that our group fabricates. Fabrication of these stacks requires deviations from our standard junction fabrication process. The reason behind the complexity is the limitations of the sputtering chamber. The junctions contain five metals that we sputter from large targets: Nb, Al, Ni, Pd and Co, and three metals we sputter from small targets: Ru, Cu and Au. The chamber is designed to hold seven sputtering targets (four large and

three small) at once along with an ion mill. Since the process calls for 5 large targets, this means we need to exchange one of the targets during the sputtering process. This exchange of targets involves breaking vacuum and replacing one of the targets while the chamber is kept warm and with an argon environment. The exchange needs to be done as quickly as possible to avoid sample contamination. The sample must also have a layer of Au sputtered on it before breaking vacuum that must be milled off before continuing with the sputtering process. For all of our junctions we start first with the photolithography of the bottom lead. The bottom lead lithography is the most important step of the fabrication process. The layers deposited need to be as smooth as possible. Most of the process is carried out inside of a class 100 cleanroom to avoid debris adhering to the bare substrate. Any contaminants would propagate through all the layers. The smoothness of the layers gives more consistent switching characteristics of the Ni layers. The photomask we use has room for the connection of six junctions. The bi-layer photoresist recipe mentioned in chapter 3 is required for this process. This ensures well defined features after lift-off.

Figure 4.6 shows the bottom lead mask where we have two pads that are used as common connections for all 6 junctions. The four outer features along with the feature near the center of the mask, indicated with green circles, are the alignment marks that will be used for aligning the top lead to the bottom lead later in the process. There are smaller features near pairs of junctions that are used to align for EBL. The diamond pattern of the top pad is used for reference orientation when the samples are being handled without microscopes.

The photolithography process is the one discussed in chapter 3. The alignment process is not as important for the bottom lead as it is for the top lead. The important step is the contact pressure. The better the contact pressure the more accurately the features on the mask are reproduced on the chips. Setting up the sputtering chamber for bottom

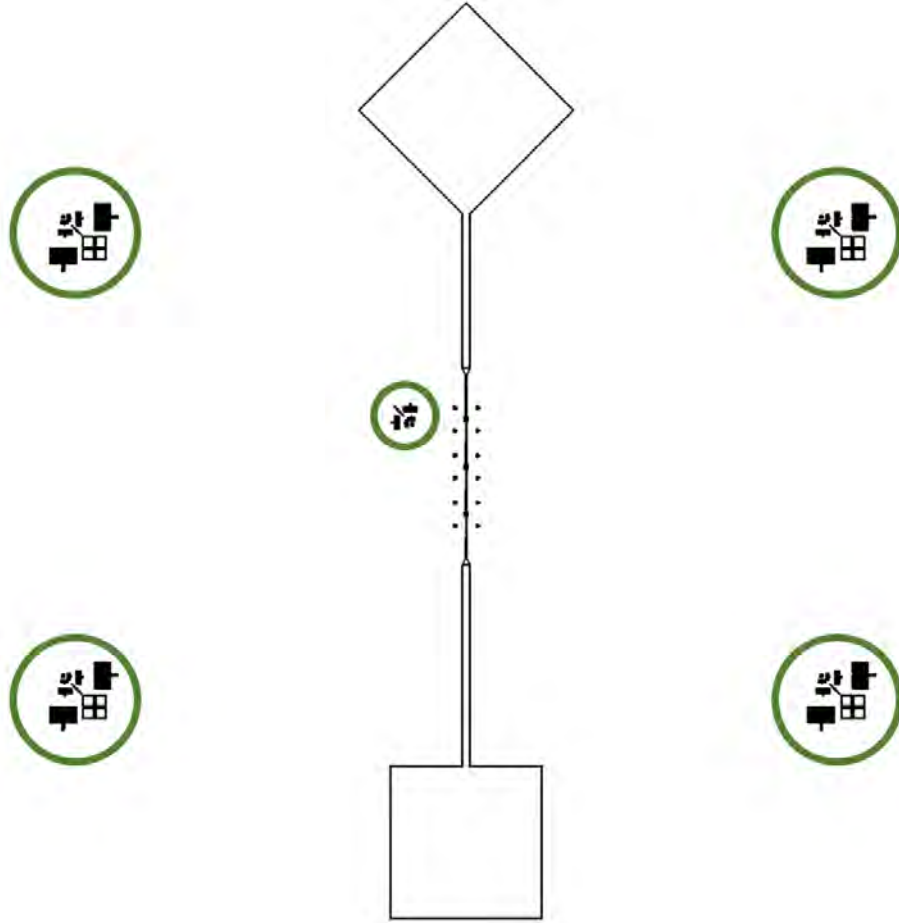


Figure 4.6: *Bottom Lead*: Top down perspective of the bottom lead photolithography mask. Two pads are the common connections for measurement. Alignment marks are indicated by green circles.

lead sputtering includes having the process ready for breaking vacuum during the run and replacing some of the targets for sputtering the second step in the bottom leads.

After the bottom leads are deposited, the chips are taken back into the cleanroom for lift-off. The rest of the junction fabrication process is described in Chapter 3 and summarized in Figure 3.1. The junctions we fabricate are elliptical to take advantage of the shape anisotropy for controlling the in-plane magnetic layers. The junctions have lateral dimensions of $1.25 \times 0.5 \mu m^2$. The Ni layers point along the longer axis of the ellipse which is called the easy axis. If we apply a large magnetic field in the opposite direction the Ni magnetization direction



Figure 4.7: *Sample mounted on QDI*: Electrical connections using Indium for sample mounted on QDI.

changes but still tends to point along the easy axis. Because we are using two Ni layers in addition to the PMA layer we should observe the switching of both layers at similar fields when sweeping the external magnet. This experiment will give the parallel state of the junctions when measured.

4.3 Measurement

Before we start handling any samples we must use a static wrist guard to prevent damaging them during the wiring process. Depending on the expected sample critical current value we can either use room temperature electronics or low temperature electronics. Once the sample is placed on the dipper we use sewing thread and wrap it around the sample and brass base to mount the sample.

Figure 4.7 is an image of sample mounted on Quick Dipper 1 (QDI). The base is isolated from the sample by waxed paper. The connections to the pads are made using Indium. The voltage wires connected to the SQUID are superconducting while the current lines are copper. The external superconducting magnet is wound on the brass barrel that slides over

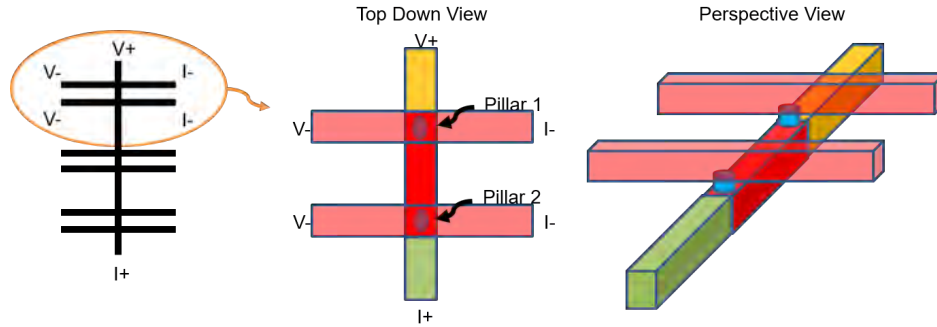


Figure 4.8: *Bottom Lead*: Cartoon representation of the bottom and top lead with the junctions sandwiched between.

the sample once the connections are tested.

Once the samples have been connected we test for proper connections using a multi-meter set to high resistance range, 2 kOhms, to avoid damaging the samples. The measurement data is taken using a Labview program created and updated in the Birge group. The measurement program controls current sources that drive the superconducting magnet and the sample as well as voltmeters that measure the voltage drop across a precision resistor to calculate the current through the magnet and the voltage across the sample. Figure 4.8 shows a cartoon representation of the top and bottom leads with the junctions between them. We use the bottom lead as common voltage and current connections and the top lead is used to select which junction we want to measure. Since these junctions contain Ni, initialization is done at a field of 2000 Oe to ensure the Ni domains are all pointed along the same direction. Sometimes we must initialize the Ni several times to “train” the layers. This training effect can be observed when the same sample is measured after similar initialization steps in a single dip. The Fraunhofer pattern looks smoother and more defined after you repeat the initialization process several times. It is important to point out that the sample must be taken into the normal state before each measurement if the initialization field is greater than 1500 Oe. Since the samples and measurement system contain Nb superconductors for the

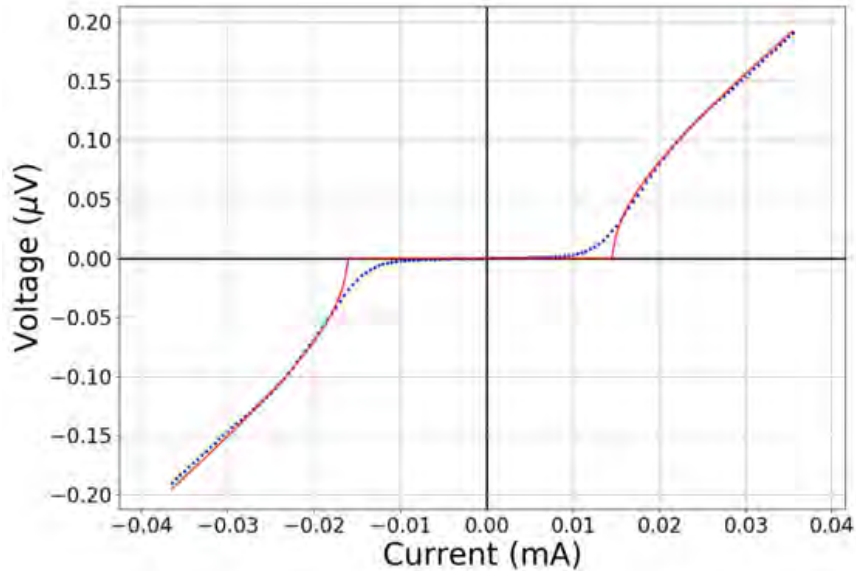


Figure 4.9: V vs. I : V vs. I . Plot of voltage vs. current for a typical Josephson junction. The red line is a fit to the data of the square-root function discussed in the text.

leads and wires, the initializing of the sample causes flux trapping that persists after the field is turned off. When the field exceeds 1500 Oe we remove the trapped flux by raising the sample out of the liquid helium bath and let it warm up enough so that it is no longer superconducting. We check this by connecting a multimeter to the sample as we raise the dipper to notice an increase in the resistance of the sample.

Figure 4.9 shows a typical I vs. V curve taken from our measurement system. The blue points are actual data from the measurement while the red line is the square root (SQR) $|V| = R\sqrt{I^2 - I_{c0}^2}$ function we use to fit the data. The sharp point on either side of the origin is the critical current value taken from the fit. Since these junctions have a smaller than typical critical current we observe rounding near the fitted critical data value. The data can be fit using another model, Ivanchenko-Zilberman (IZ) model, which takes into account the thermal rounding for smaller critical current junctions. The IZ model takes much more time to fit and sometimes has problems fitting nearly-linear I - V curves when the I_c value is

very small. The difference in the fits gives a slightly higher critical current for the IZ model so using the SQR model gives us a lower bound to the data.

4.4 Results

Once we have collected all the IV curves we can now move on to extraction of the critical currents of the data. For each step of the magnetic field we will plot a critical current. Figure 4.10 is a plot of critical current vs. field which is known as a Fraunhofer pattern of one of the triplet PMA junctions. We can see that I_c goes to zero between each lobe signifying that our sample has no shorts. In this case the sample was initialized with the field in the negative direction and the measurement was taken with the field stepping in the positive direction. The measurement procedure was stopped when the field reached 20 mT to avoid causing the Ni magnetization to switch in the other direction. For this sample the maximum I_c was about 0.4 mA. These measurements were done for both types of junctions with similar initialization procedures. For the I_c of each junction we used the maximum value taken at the peak of the Fraunhofer pattern.

In figure 4.11 we show data for both triplet and shuffled PMA-SAF junctions with Ni thicknesses of 1.2 and 1.6 nanometers. We notice that the triplet junctions in either thickness have similar $I_c R_n$ products of about $1\mu V$. The plot also shows that the shuffled junctions have a much smaller critical current when compared to the triplet junctions. We can also see what we expect to see when observing singlet critical current, namely that the thicker Ni junctions have a smaller $I_c R_n$ product when compared to the thinner Ni junctions. This decay of critical current as thickness increases is a signature of supercurrent in singlet Josephson junctions.

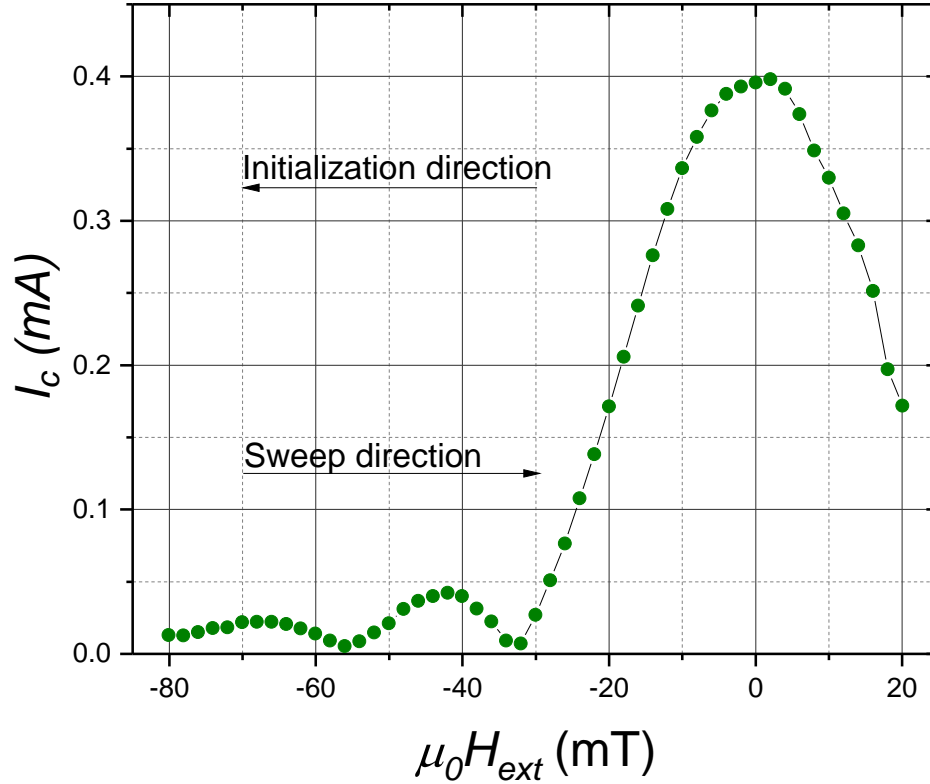


Figure 4.10: I_c vs. H : Plot of critical current vs. external magnetic field of a PMA Josephson junction. For this measurement the pillar was initialized with the magnetic field in the negative direction. The field was then swept in the positive direction passing zero field and stopped just before the Ni magnetization switches to the opposite direction.

4.5 Conclusions

The chapter shows the fabrication, measurement and data collecting procedure as well as the interpretation of triplet and singlet Josephson junctions. Since singlet supercurrent doesn't depend on the order of the various magnetic layers, the shuffled junctions allowed us to obtain a direct comparison of the triplet and singlet supercurrent in Josephson junctions. The supercurrent in triplet Josephson junctions is shown to be dominated by spin triplet pair carriers by the observation of the larger $I_c R_n$ products of triplet junctions when compared to shuffled junctions.

We can now understand what Joseph Glick's work showed when he compared his triplet

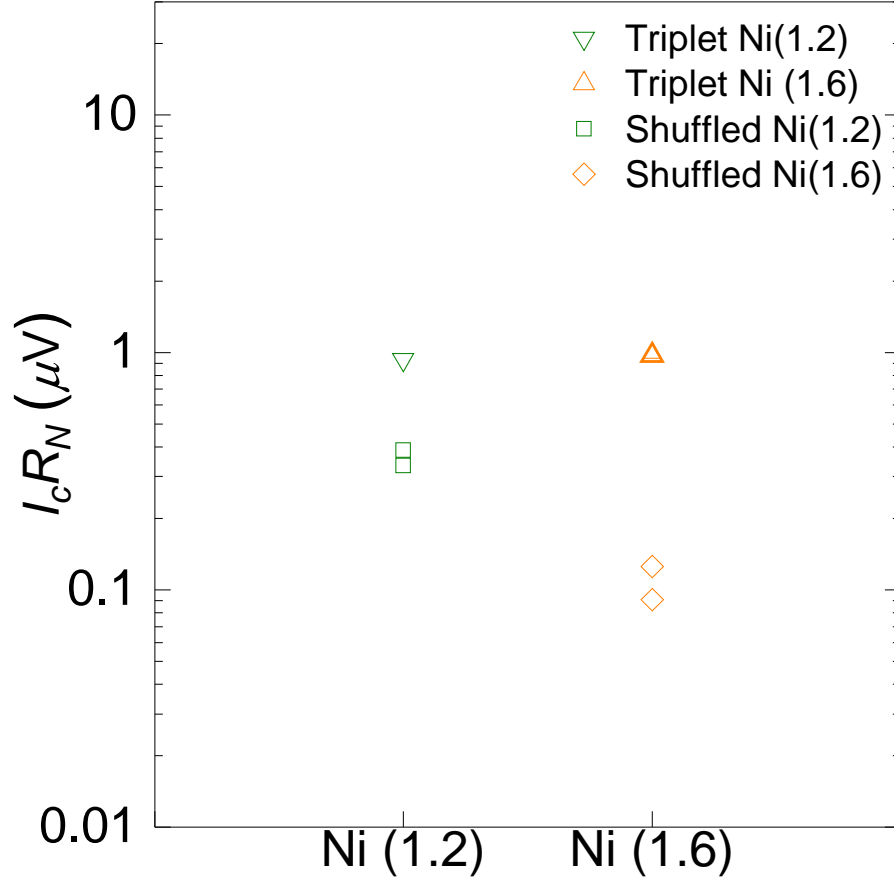


Figure 4.11: $I_c R_n$ vs. Ni Thickness: Plot of $I_c R_n$ vs Ni thickness. This plot shows the $I_c R_n$ product of PMA-SAF triplet junctions (triangles) and PMA-SAF shuffled junctions (squares) of with two different Ni thickness plotted with corresponding . Triplet junctions shows similar $I_c R_n$ product for either thickness. Shuffled junctions show a smaller value of $I_c R_n$ for the larger Ni thickness.

and singlet junctions. In junctions with the thinnest Co/Pd multilayers (with one Co/Pd bilayer on each side of the SAF), the larger supercurrent he observed in his singlet junctions was simply due to the fact that those junctions contained fewer magnetic layers, and fewer interfaces, than his triplet junctions. Once the total number of Co/Pd bilayers increased to $n = 4$ or greater (two bilayers on each side of the SAF), then triplet junctions had larger I_c , as expected.

The decay of the supercurrent with Ni thickness is a more subtle issue. We know from

Chapter 2 that singlet pair correlations and associated supercurrent oscillate and decay with F-layer thickness. For Josephson junctions containing a single layer of pure Ni, Baek *et al.* have shown that the oscillations in I_c have minima at Ni thicknesses of about 0.9 nm and 3.5 nm. In our shuffled junctions, putting two 1.6-nm Ni layers back-to-back may act similarly to a single Ni layer of thickness 3.2 nm, which is close to the minimum at 3.5 nm. So the smaller value of $I_c R_n$ in the 1.6-nm shuffled junctions may be a signature of the oscillation, rather than the overall decay with thickness. Nevertheless, the lack of decay of the supercurrent with Ni thickness in triplet junctions suggests that these junctions carry mostly spin triplet pair correlations.

Chapter 5

PMA-SAF and PMA Josephson junctions

In this chapter we will look at two types of spin triplet Josephson junctions that contain three ferromagnetic layers. The motivation for this work stems from the previous work done by, former graduate student, Joseph Glick on spin triplet Josephson junctions. Joseph was able to control the ground-state phase difference across these junctions between 0 and π by switching one of the three ferromagnetic layers by 180 degrees without disturbing the other two layers. Such a phase-controllable junction could be used as a memory element in a superconducting computer. Joseph's junctions had critical current values up to $5\mu A$, which is too small for use in a memory element. Because of this the next goal is to increase the critical current in these spin-triplet Josephson junctions while maintaining phase control.

As in the previous chapter, the junctions studied here are composed of three ferromagnetic layers, where one of the layers has an out of plane magnetization and the other two layers have in plane magnetization. These junctions are able to convert spin singlet supercurrent into spin triplet supercurrent in their central ferromagnetic layer. The ability to convert to spin triplet is due to the layers having non-collinear magnetization between adjacent layers. The spin triplet supercurrent, as we have seen in chapter 4, can propagate further in a ferromagnetic layer when compared to spin singlet supercurrent. The work in this chapter is focused on the central Pd/Co multilayer that has out-of-plane (OOP) magnetization. The complete junction stacks are composed of two in plane ferromagnetic layers surrounding an out of plane ferromagnetic layer. The OOP layer in these junctions can be either in the form

as a single Co/Pd multilayer, which we will refer to as PMA for perpendicular magnetic anisotropy, or as two multilayers coupled antiferromagnetically, which we refer to as PMA-SAF. We have seen that spin triplet supercurrent is the dominant supercurrent in these junctions and now we will be focusing on increasing the amount of spin triplet propagation in Josephson junctions.

5.1 Magnetic Properties

All Josephson junction fabrication starts with first understanding the magnetic properties of the individual layers. Similar to the work done from chapter 4 we begin by looking at the Pd/Co multilayers. In figure 5.1a we see the PMA stack which is composed of repeated layers of Pd(0.9nm) and Co(0.3nm) sputtered directly on top of each other. The PMA-SAF stack has the same layers as the PMA, but with the Pd layer in the very middle replaced by a Ru(0.95nm) layer. The Ru layer causes the adjacent Co layers to couple antiferromagnetically. The total number of Co layers in the PMA-SAF is even, with the same number above and below the Ru, which gives a net zero magnetization to the PMA-SAF. The Figure shows uniform magnetization pointing out of the plane for both the PMA and PMA-SAF stacks, but the up and down directions might be reversed in the latter. Measurements needed to show which layer is pointing in a specific direction are not available in our lab. The specific direction of the magnetization is not as important as the overall net magnetization for either stack: magnetization is out of plane for our junction design to be compatible with the spin triplet design.

For magnetic measurements we refer back to chapter 4. From figure 4.3 we know that the Pd/Co multilayers, in their virgin state, have large domains that are non uniform in size

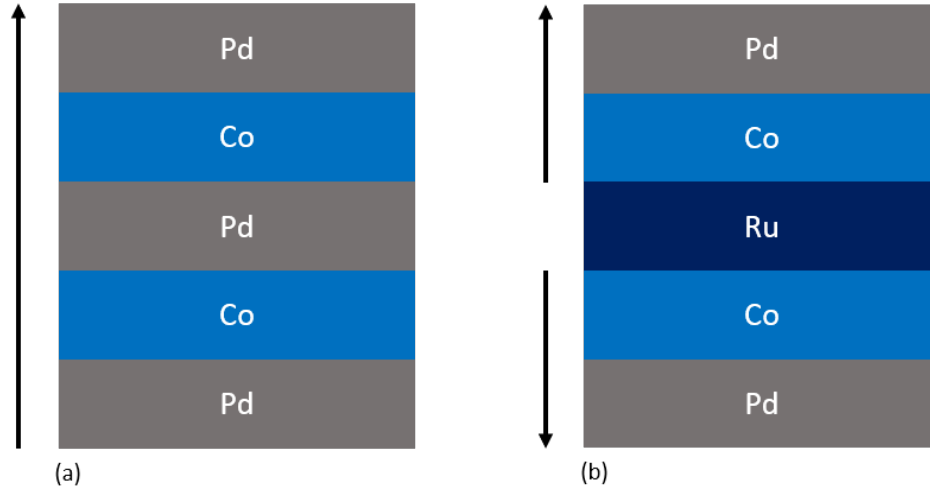


Figure 5.1: *PMA-SAF and PMA*: Side view of the PMA(a.) and PMA-SAF(b.) ferromagnetic stacks with palladium/cobalt multi-layers. PMA-SAF on the left has a ruthenium spacer between the multilayers to couple them antiferromagnetically

and shape. Figure 4.4 and 4.5 have shown that the Pd/Co multilayers exhibit strong out of plane magnetization with very little in plane as well as a very high switching field when trying to change the magnetization to the opposite direction.

5.2 Fabrication of spin triplet PMA and PMA-SAF junctions

Figure 5.2 show the stacks for the PMA-SAF(a) and PMA(b) Josephson junctions. When we fabricate the PMA and PMA-SAF triplet Josephson junctions we do both in the same sputtering run to avoid any run-to-run variations in the samples. We also face the same issue that we did before where the number of guns in the sputtering chamber limited the amount of materials that can be sputtered in one run. The fabrication of these sample require five materials that are sputtered from large targets: Nb, Al, Ni, Pd and Co, and up to three materials sputtered from small targets: Ru, Cu and Au for the PMA-SAF. Since the chamber is designed to hold seven sputtering targets (four large and 3 small targets) at once along with an ion mill we must sputter the superconducting layer first then break vacuum,

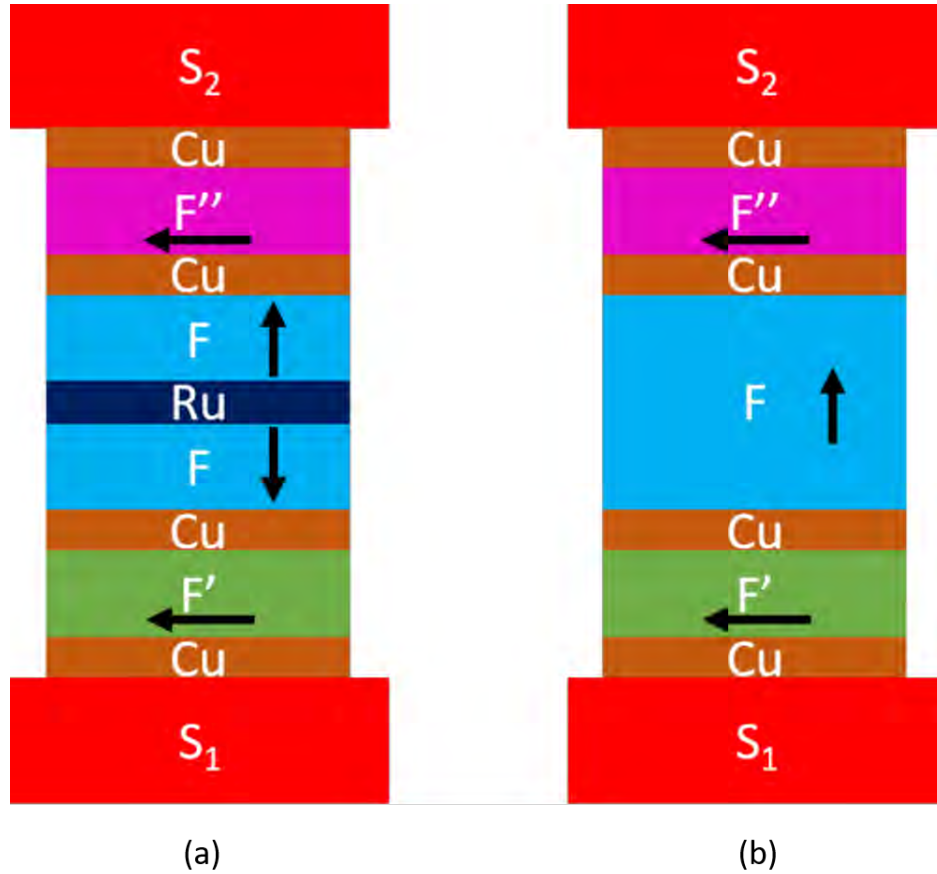


Figure 5.2: *PMA-SAF Decay*: PMA-SAF and PMA Josephson junctions.

replace the targets, and seal the chamber to sputter the ferromagnets.

The photomask used is the same as the previous chapter which has room for 6 junctions. The bi-layer photoresist recipe mentioned in chapter 3 is required for this process. This ensures well defined features after lift-off. The single junctions pattern used is the same as in chapter 4 figure 4.6. The four outer features along with the feature near the center of the mask, indicated with green circles, are the alignment marks that will be used for aligning the top lead to the bottom lead later in the process. We then use electron-beam lithography with the negative e-beam resist ma-N2401 and Ar ion milling to define the junctions. The junctions are elliptically shaped with lateral dimensions of $1.25 \times 0.5 \mu m^2$. Ion milling is immediately followed by thermal evaporation of SiOx without breaking vacuum, to isolate

the bottom and top superconducting electrodes. After the e-beam resist is removed, top leads of Nb(150)/Au(15) are sputtered through another photolithographic stencil after gentle in-situ ion milling of the protective Au layer. The diamond pattern in figure 4.6 is used for reference when the samples are being handled for measurement. The alignment process is not as important for the bottom lead as it is for the top lead since the bottom lead is going on a blank substrate. The important step to be cautious with is the the amount of contact pressure. The better the contact pressure the more resolved the feature of the mask will be on the substrate.

5.3 Measurement

We use I-V curves to characterize these junctions as a function of field applied along the direction of the long axis of the ellipse. These I-V curves follow the standard shape of an RSJ model for an overdamped junction. There is some rounding that occurs for current values near I_c that are visible in junctions with I_c less than about $10 \mu A$.

Figure 5.3 shows a typical Fraunhofer pattern for one of the spin-triplet junctions containing a PMA stack. The main central lobe and two side-lobes are clearly visible in the negative sweep. We typically stop the field sweep when the field passes through zero and reaches 20 mT in the direction opposite to the initialization direction. Continuing the field sweep past that point results in a distorted pattern due to the gradual switching of the two Ni layer magnetizations.

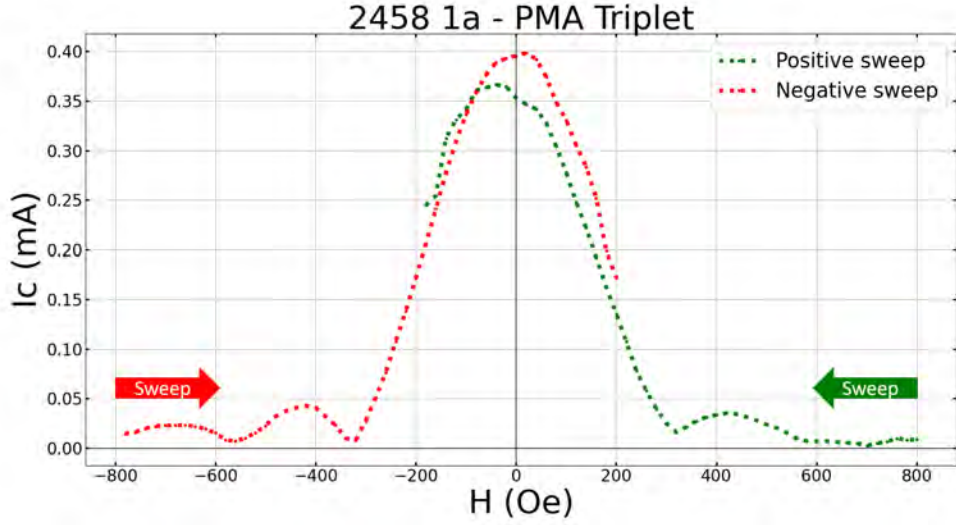


Figure 5.3: *Fraunhofer pattern of a PMA triplet Josephson junction*: Fraunhofer pattern for a PMA triplet Josephson junction containing Ni outer layers and a Pd/Co PMA central layer. The red data points were acquired during a field sweep from negative to positive after initialization at a large negative field. The green data points had a positive initialization. We chose not to go past a field of 200 Oe after passing through zero field because the slow reversal of the Ni magnetization causes distortions in the Fraunhofer pattern.

5.4 Results

The primary goal of this work is to understand the difference in supercurrent transmission between spin-triplet junctions containing a PMA-SAF and those containing a single PMA layer of the same total thickness. The data for $I_c R_N$ as a function of the total number N of [Co/Pd] bilayers in the PMA junctions are shown as green diamonds in figure 5.4, while the data for the PMA-SAF junctions are shown as red triangles. The data exhibit a striking difference between the PMA and PMA-SAF junctions. The decay of I_c with N is much shallower in the PMA junctions than in the PMA-SAF junctions. Least-squares fits of an exponential decay of the form $I_c R_N(N) = A_0 \exp(-\alpha N)$ to the data in figure 5.4 give $\alpha_{CoPd}^{PMA} = 0.191 \pm 0.017$ for the PMA junctions, and $\alpha_{CoPd}^{PMA-SAF} = 0.751 \pm 0.047$ for the PMA-SAF junctions. The ratio of those slopes is 3.9 ± 0.4 . In addition, the value of I_c is

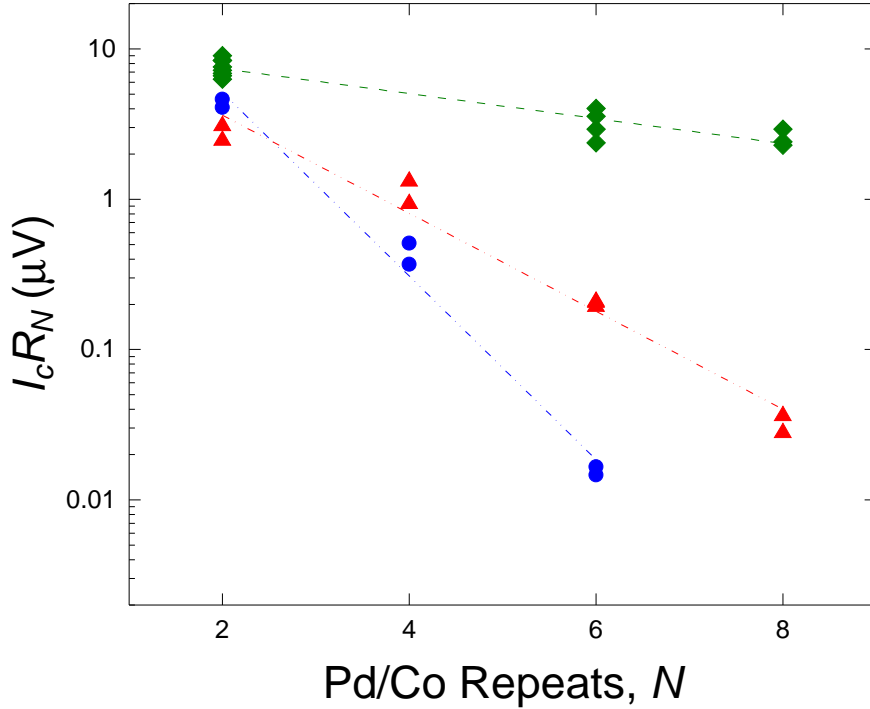


Figure 5.4: *PMA-SAF Decay*: $I_c R_N$ product vs Pd/Co repeats. PMA triplet: green diamonds. PMA-SAF triplet: red triangles. Singlet junctions: blue circles.

larger in the PMA junctions than in the PMA-SAF junctions for all values of N , including the smallest value, $N = 2$. This result is very promising for practical memory devices, if we are able to fabricate controllable-phase PMA junctions by replacing one of the two Ni layers with NiFe, as we did with PMA-SAF junctions

There are two theoretical works [94,95] that deal with the kind of system studied here. The “P-state” and “AP-state” in those works correspond to our PMA and PMA-SAF junctions, respectively. (The fact that their F layer is in plane as opposed to ours being out of plane is not relevant; only the relative orientations of the different magnetizations matters.) Both theoretical works predict that the critical current in the AP state will be slightly larger than in the P state, which clearly disagrees with the data shown in Fig. 5.4 That is not surprising. Both theoretical works utilize the quasi-classical theory, which does not account

for differences in transport properties between majority and minority spin bands in the bulk of the F materials and at F/N interfaces. The disagreement with experiment highlights the fact that the differences we observe between our PMA and PMA-SAF junctions are due to those band structure effects.

To understand what is causing this shallower decay we must first have a brief understanding of how a three layer spin-triplet junction converts spin-singlet supercurrent to spin-triplet supercurrent. When spin-singlet pairs enter the first ferromagnet F' from the bottom superconducting electrode they oscillate between singlet and $m_s=0$ triplet states as they propagate through the magnet. When the pairs enter the F layer, and assuming the $m_s=0$ triplet amplitude is not zero, they are converted to $m_s=\pm 1$ states in the new rotated basis. These triplet pair propagate freely in the F layer until they reach the F'' layer where they are now converted back into the $m_s=0$ triplet pairs. As they propagate from F'' the pairs again oscillate between the $m_s=0$ triplet and singlet states. The singlet component is allowed to enter the top superconducting electrode to be measured as a supercurrent.

Looking at normal-state spintronics can give some insight of what happens to current passing through ferromagnets. When charge current passes through a ferromagnetic material F it becomes partially spin-polarized due to the differences in density of states, Fermi velocity, and mean free path between majority and minority spin electrons. Since F acts as a spin filter for normal electrons, we expect that it also acts as a spin filter for $m_s = \pm 1$ spin-triplet electron pairs. [96–99]. Let us assume that the majority band triplet component has higher transmission through a $[\text{Co/Pd}]_n$ multilayer than the minority band component. The spin-triplet supercurrent passing through the multilayer then becomes partially spin-polarized, so that the $m_s = +1$ triplet component has larger amplitude than the $m_s = -1$ component. In the PMA-SAF junctions, however, the majority-spin pairs in the first PMA multilayer

become minority-spin pairs in the second PMA multilayer, and vice versa. As a result, both triplet components suffer from the lower transmission amplitude of the minority component somewhere in the system. In the PMA junctions, in contrast, the majority pairs propagate through the whole F layer with high transmission. If that were the whole story, then we would expect the I_c data from the PMA-SAF samples to be shifted downward in figure 5.2 with respect to the I_c data from the PMA samples. But that is not what we observe. Rather, the slope of the data vs N is steeper in the former, meaning that the downward shift increases with the number of bilayers N . That implies that the spin-filter efficiency of the PMA system increases with N , at least for N as large as 8, which is the largest value probed in this work.

A possible explanation for the increase in spin-filter efficiency with N is that each individual Co/Pd interface acts as a partial spin filter, due to a spin-scattering asymmetry at the Co/Pd interface favoring transmission of majority-spin pairs over minority-spin pairs. Unfortunately, the spin-scattering asymmetry at the Co/Pd interface has not been measured. Fortunately, however, the interfacial spin-scattering asymmetry has been determined for several other material interfaces by analyzing Giant Magnetoresistance data obtained from metallic multilayers and spin valves [100]. The analysis is based on the “two-current series resistor (2CSR) model”, [101–103] which has been very successful in describing a large collection of experimental results. [100, 104] The 2CSR model ascribes different effective resistivities to majority and minority-band electrons inside F materials, and different effective interface resistances at F/N or F₁/F₂ interfaces. A good example is the Co/Ni interface, where the spin-scattering asymmetry was found to be quite large [105]: the area-resistance product for majority-band electrons was found to be $AR_{Co/Ni}^\uparrow = 0.03 \pm 0.02 f\Omega m^2$ while the minority band interface resistance is much higher: $AR_{Co/Ni}^\downarrow = 1.00 \pm 0.07 f\Omega m^2$. Hence the

Co/Ni interface acts very strongly to spin-polarize a normal current, and we suspect it does the same for supercurrent. In addition, the probability for an electron to flip its spin at the interface has also been measured. It is expressed as $P=1-\exp(-\delta)$, with $\delta_{Co/Ni} = 0.35 \pm 0.05$.

We now present a model that can be helpful to understand the slopes in Figure 5.4. [22] We start with the assumption that the total supercurrent through the junctions is equal to the sum of the $m_s=+1$ and $m_s=-1$ triplet components of the supercurrent in the central F layer of the junction, which we write in shorthand as

$$I_c \propto T_{m_s=+1} + T_{m_s=-1} \quad (5.1)$$

where $T_{m_s=+1}$ and $T_{m_s=-1}$ represents the transmission amplitudes of the $m_s=+1$ and $m_s=-1$ triplet components through the central F layer of the junction. We will assume that each of those amplitudes can be expressed as a product of transmission amplitudes as the interfaces inside the F layer. (We neglect bulk effects for simplicity.) Let t_\uparrow and t_\downarrow be the transmission amplitudes through a single Co/Pd interface for the majority-band and minority-band electron pairs, respectively. A PMA junction with N Co/Pd bilayers contains $2N$ Co/Pd interfaces, hence we have

$$T_{m_s=+1}^{PMA} = t_\uparrow^{2N}, T_{m_s=-1}^{PMA} = t_\downarrow^{2N} \quad (5.2)$$

A PMA-SAF junction contains, in each half of the SAF, $N - 1$ Co/Pd interfaces and one Co/Ru interface. To keep the formulas as simple as possible, we will assume that the Co/Ru interface has the same properties as the Co/Pd interface, so we can say that each half of the SAF has N Co/Pd interfaces. (Deviations from that assumption will affect the intercept but not the slope of the line depicting $\log(I_c)$ vs N .) Since majority-band pairs in one half of

the SAF become minority-band pairs in the other half, we have:

$$T_{ms=+1}^{PMA-SAF} = T_{ms=-1}^{PMA-SAF} = t_{\uparrow}^N t_{\downarrow}^N \quad (5.3)$$

Putting all this together gives:

$$I_c^{PMA} \propto t_{\uparrow}^{2N} + t_{\downarrow}^{2N} \quad (5.4)$$

$$I_c^{PMA-SAF} \propto 2t_{\uparrow}^N t_{\downarrow}^N \quad (5.5)$$

If we define the ratio $r = t_{\uparrow}^N / t_{\downarrow}^N$, then we can write

$$\frac{I_c^{PMA-SAF}}{I_c^{PMA}} = \frac{2r^N}{1 + r^{2N}} \quad (5.6)$$

If $r^{2N} \ll 1$, then we get the simple result:

$$\ln(I_c^{PMA-SAF}) - \ln(I_c^{PMA}) = \ln(2) + N \ln(r) \quad (5.7)$$

If each I_c depends exponentially on N , as the data in Figure 5.4 show, then equation 5.7 implies that the difference between the exponential slopes of the PMA and PMA-SAF junction data should be $\ln(r)$. From the values for the Co/Pd interfaces, we found $-\alpha_{CoPd}^{PMA-SAF} + \alpha_{CoPd}^{PMA} = -0.751 + 0.191 = -0.56$, which gives $r_{CoPd} = 0.57$. It would be beneficial to compare that value to an independent measurement of r using GMR techniques, but that has not been done. This model does not incorporate spin-flip and spin-orbit scattering, which suppress spin-triplet supercurrent, although we would expect them to cause

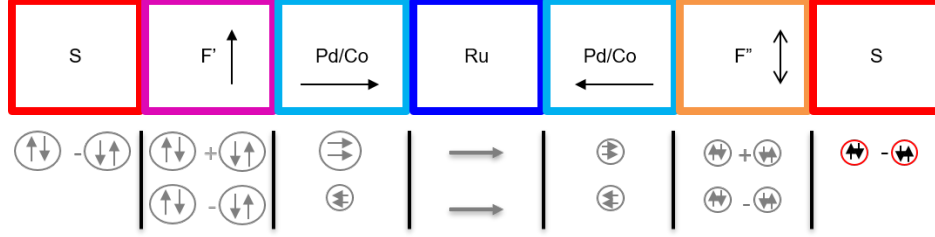


Figure 5.5: *PMA-SAF Decay*: PMA-SAF Decay. Visual interpretation of the decay mechanism in PMA-SAF Josephson junctions containing a Pd/Co multilayer sandwiched by two Ni layers.

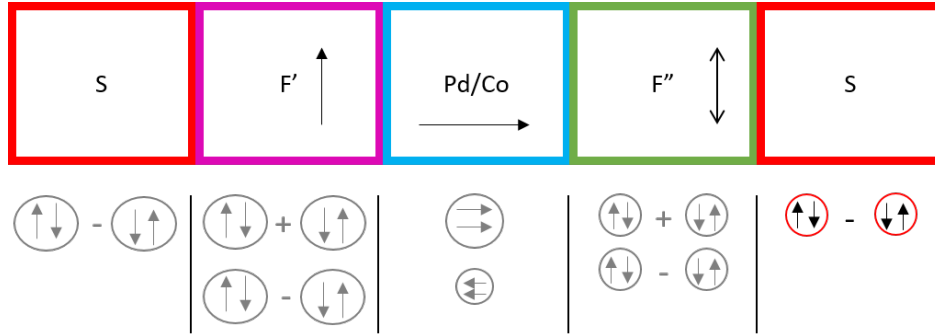


Figure 5.6: *PMA Decay*: PMA Decay. Visual interpretation of the decay mechanism in PMA Josephson junctions containing a Pd/Co multilayer sandwiched by two Ni layers.

equal suppression of I_c in the PMA and PMA-SAF junctions.

We also present a simple figure to help motivate the previous discussion. Figure 5.5 is a cartoon interpretation of the decay in spin-triplet PMA-SAF Josephson junctions. We notice in the F' layer that we have both singlet and $m_s=0$ triplet pairs. In the first stack of Pd/Co multilayers the $m_s=0$ triplet pairs are converted to $m_s=\pm 1$ triplet pairs. Some of the pairs are suppressed which we will call the minority band while the majority band is not suppressed. The triplet pairs pass through the Ru layer and enter the second Pd/Co multilayer where the magnetization is in the opposite direction of the first multilayer. The second multilayer suppresses the majority band and lets the minority band pass through untouched. The triplet pairs are then converted back into $m_s=0$ triplet which enters into the superconductor to be measured.

Figure 5.6 is a cartoon representation of the decay in a spin-triplet PMA Josephson junction. Picking up in figure 5.5 where the pairs enter the first Pd/Co multilayer we can see the suppression of the minority band pairs in the F layer. We now enter directly into the F'' layer where we convert to $m_s=0$ triplet which is converted to singlet and enters the superconducting electrode. We can see from the cartoon in 5.6 that we have only one of the bands is suppressed. The higher number of repeats in the Pd/Co multilayers the higher the suppression of that particular band. This give a graphical interpretation of what we see in Figure 5.4. The higher the number of repeats the more suppression of the IcRn products in both the PMA and PMA triplet junctions. The PMA-SAF has this suppression occur for both majority and minority spin band cause a larger suppression as we increase N.

5.5 Conclusions

In conclusion, we have measured the supercurrent in both spin triplet PMA and spin triplet PMA-SAF Josephson junctions that contain Pd/Co multilayers as the central out-of-plane ferromagnet and Ni as the in-plane ferromagnetic layers. The critical currents in the PMA-SAF junctions decay far more rapidly with increased number of multilayer repeats N , compared to the critical currents in the PMA junctions. We attribute that difference to the strong increase of spin polarization of the supercurrent with increasing repeats N , due to the cumulative spin-filtering effect of the interfaces in the PMA multilayers. The triplet PMA junctions have larger critical current at the lowest number of Pd/Co repeats, and the critical current decays much more slowly as a function of Pd/Co repeats. An important point to mention is that although in our experiments we like to avoid the suppression of critical current that occurs with increasing the number of Pd/Co repeats, this result may be

important for other fields of electronics. The ability to produce a spin triplet supercurrent in a Josephson junction that is highly polarized may have home applications in the spintronics field.

Chapter 6

Phase Controllable SQUIDS

In the previous chapters we were working towards the goal of increasing the propagation of supercurrent through spin triplet Josephson junctions. The goal of this chapter is to build on that previous work and show controllable switching of the triplet Josephson junctions through phase sensitive measurements. To accomplish this goal we must be able to make a junction that can switch between its zero and π ground states. The tool needed for making phase measurements is a Super Conducting QUantum Interference Device (SQUID). To fabricate this tool we need two Josephson junctions in parallel around a SQUID loop. As discussed in section 2.6 a SQUID is able to detect differences in the phase between current flowing through the two junctions in the loop. The fabrication of these SQUIDS is similar to the previous work but care needs to be taken in some key points that will be mentioned in the fabrication section.

In this chapter we plan to show phase control of Josephson junctions of the same type as presented in chapter 5. We want to demonstrate switching of the soft magnetic layer by changing its magnetization direction by 180° , without disturbing the other magnetic layers, causing switching between zero and π states. We have fabricated samples with varying repeats of Pd/Co layers. The measurements of the SQUIDS in this chapter confirm the result from the previous chapter that the spin triplet PMA junctions have larger critical current when compared to the spin triplet PMA-SAF junctions.

Figure 6.1 show a cartoon diagram of the junctions we use in these SQUIDS. The junctions

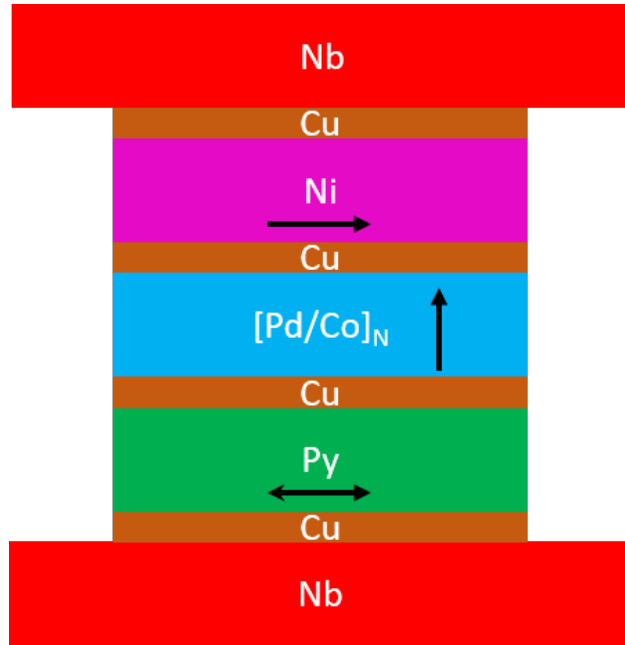


Figure 6.1: *Triplet PMA Josephson Junction*: Side view of the triplet PMA stack with Ni and Py. Py, as the soft layer, is at the bottom of the stack and is deposited as soon as possible to be as smooth as possible.

contain a similar stack as in the previous chapter but we have replaced the bottom Ni layer with Permalloy (Py), a NiFe alloy with low coercivity. The Py is deposited on the bottom of the stack to keep this layer as smooth as possible. The Py layer will act as the switching layer since it has a smaller switching field compared to Ni. The Py layer is referred to as the soft layer. We will also show how training of the sample changes the switching behavior of the same sample in a single cool down.

6.1 Magnetic characterization

As is done for all magnetic samples before going through the complete fabrication process we first need to look at the magnetic behavior of the layers. These measurements will help us understand the switching fields for these junctions with the PMA as the central ferromagnet. We start with sputtering films similar to what the junctions will contain except

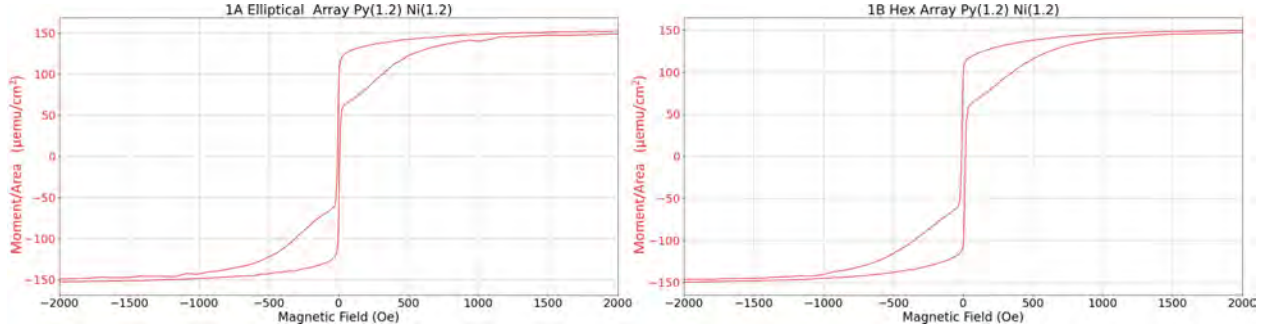


Figure 6.2: *Easy axis magnetometer measurement of elliptical and hex arrays*: M vs. H plots of arrays containing Ni(1.2) and Py(1.2) for both elliptical and hex arrays. This large field sweep switches both ferromagnetic layers. The Permalloy layer switches abruptly close to zero field, while the Ni layer switches slowly over the field range 0-1000 Oe.

for the bottom Nb layer being thinner than what we use for junctions. The film contains Nb(10)/Cu(2)/Py(1.2)/Cu(4)/PMA/Cu(4)/Ni(1.2)/Cu(2)/Au(2) where the PMA layer is $[\text{Pd}(0.9)/\text{Co}(0.3)]_N/\text{Pd}(0.9)$ and N is the number of repeated Pd/Co bilayers. The films are sputtered together for consistency since we will fabricate both elliptical and hexagonal arrays for direct comparison. The ellipses have an aspect ratio of 2.0 while the hexagons have an aspect ratio of 3.0, with both maintaining $0.5\mu\text{m}^2$ in cross-sectional area. There needs to be a significant difference in the switching field of the elliptical junctions compared to the hexagonal junctions since we need the soft layer (Py) of the ellipse to switch before the hexagon does for the SQUIDS to work properly.

Figure 6.2 shows M vs. H curves of large arrays of elliptical and hexagonal nanomagnets. These arrays have 45×45 patterns that each contain 39×99 individual nanomagnets (or “pillars”). The arrays must contain a large number of pillars to have a signal that is strong enough to measure in a SQUID magnetometer. These figures show the switching of both magnetic layers in the junctions. The Py layers appear to switch abruptly at very low field in these plots, while the Ni layers switch gradually over a very broad field range.

Figure 6.3 shows M vs. H curves but taken at small field to switch only one of the

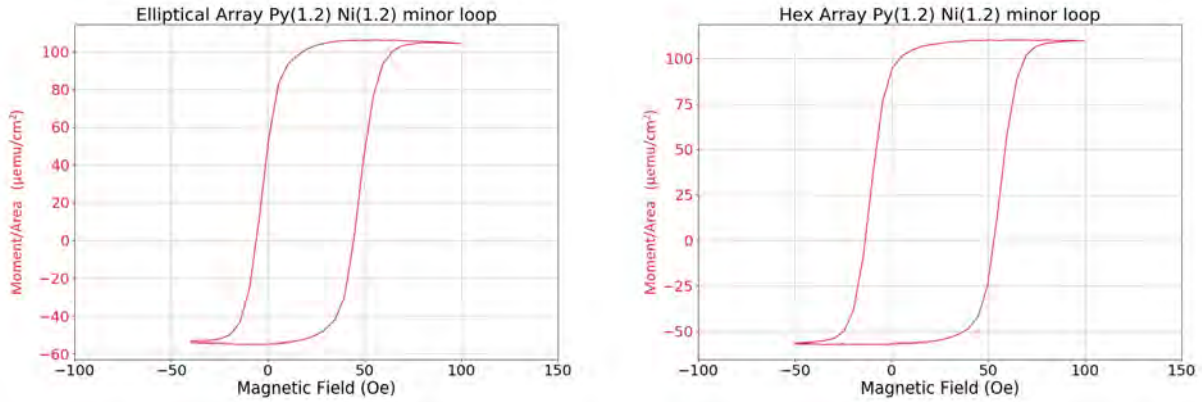


Figure 6.3: *Easy axis magnetometer measurement of elliptical and hex arrays*: Minor loop M vs. H plots of arrays containing Ni(1.2) and Py(1.2) for both elliptical and hex arrays. The vertical shift is due to the magnetization of the Ni layer, while the horizontal shift is due to trapped flux in the magnet. The minor loops let us measure the switching field for only the Py layer without disturbing the Ni layer. The coercive fields for the ellipse and hex arrays are 25 Oe and 35 Oe, respectively.

magnetic layers. These data represent minor loops where we can see an offset in the vertical and horizontal direction. The horizontal and vertical shifts are due to the trapped flux in the magnet and the magnetization of the Ni layers, respectively, but those are not important for this measurement. These data show the actual coercive field for the elliptical and hexagonal arrays. For the elliptical arrays we get about 25 Oe and for the hex arrays we get about 35 Oe. In the ideal case, each nanomagnet in the array would switch abruptly and all elements would switch at the same field, hence the switching of the arrays would be perfectly vertical on the M vs. H diagram. The finite slope observed is due either to a spread of switching fields in the array, or to slow switching of individual array elements by domain wall motion.

6.2 SQUID fabrication

The fabrication of the SQUIDS containing spin triplet Josephson junctions is similar to the previous experiments. There are two types of SQUID masks that are available to use

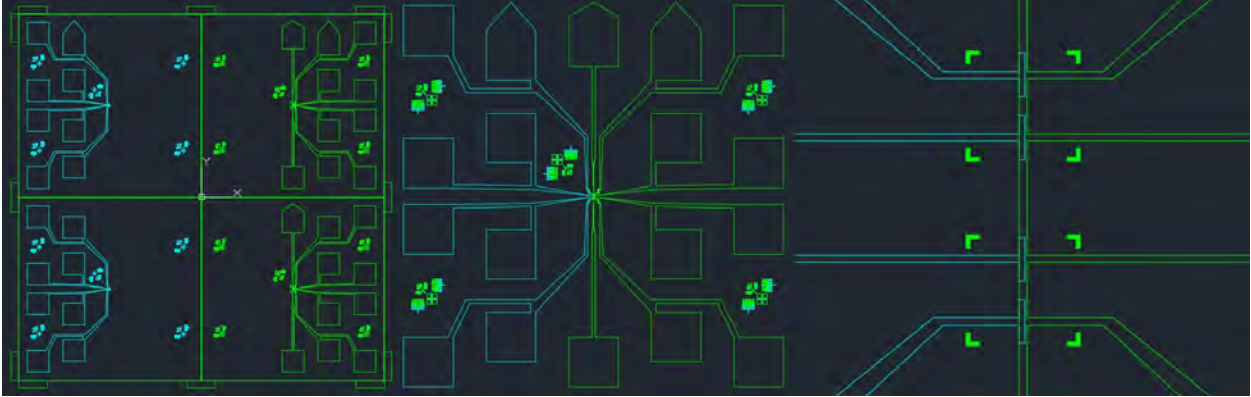


Figure 6.4: *Photolithography SQUID mask design*: Left to right, full chip, top and bottom lead overlap, ultra low inductance SQUID blow up. These masks are on quartz glass and measure five inches by five inches in size.

for these SQUIDS. One is the Symmetric SQUID and the other is the Ultra Low Inductance SQUID (ULI). For these samples we chose to use the ULI design since we have made previous SQUIDS that gave good results for this design.

Figure 6.4 shows the photolithography mask set for this SQUID design. The mask is designed using Autocad. From left to right we see the first design shows the full mask. In this image we can see the top leads on the left side and the bottom leads on the right. The bottom lead pattern has five large alignment markers that are used to align with the similar markers on the top lead pattern. There are ten pads on the bottom lead while the top lead has eight. The two extra pads the bottom lead has are for the on-chip flux line. Moving to the middle image we see the top and bottom lead overlap. This is what we expect to see on the substrates once we are finished with fabrication of the samples. In this image you can see the tapering of the leads as they get closer to the center of the design. The tapering of the lines helps prevent unwanted lift off the leads during processing. The previous mask design showed more lift off issues because it had much smaller leads further from the center of the chip. The image on the right show a close up of the ultra low inductance SQUID design. This is the design we used for this experiment. The ULI SQUID design has four SQUIDS per

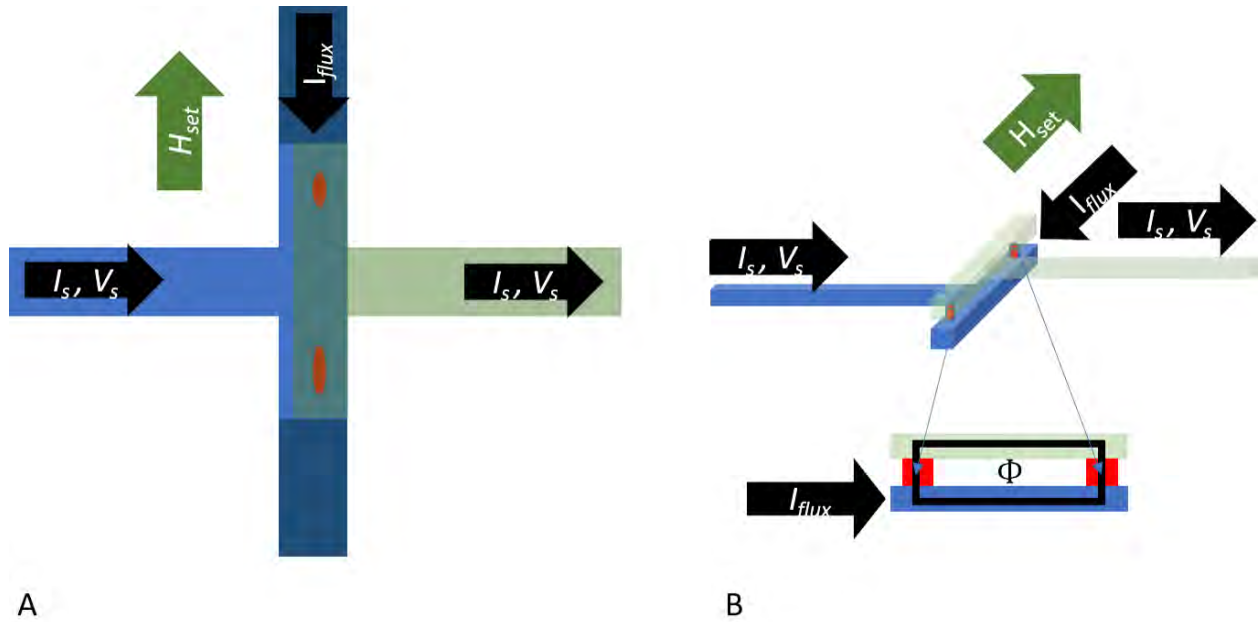


Figure 6.5: *Top and orthographics view of ULI SQUID design: Top down view of the ULI SQUID design(a) and Orthographic view of the ULI SQUID design(b).*

sample. This image shows the eight L-shaped electron beam lithography alignment marks. The bottom lead is four microns in width nearing the SQUID while the top lead of the SQUID is 3 microns wide at the center.

Figure 6.5 shows the top down view and orthographic view of the ULI SQUID design. Figure 6.5a shows the two different shapes we used in the SQUIDS. The upper junction in the figure is shaped as an ellipse with an aspect ratio of 2.0 while the lower junction is shaped as a hexagon with an aspect ratio of 3.0. These shapes were selected to take advantage of their shape anisotropy. Figure 6.5b shows the SQUID loop where we couple magnetic flux via current I_{flux} through an on-chip flux line. H_{set} is the field that is used to switch the soft layer in these junctions. H_{set} is produced by an external superconducting magnet.

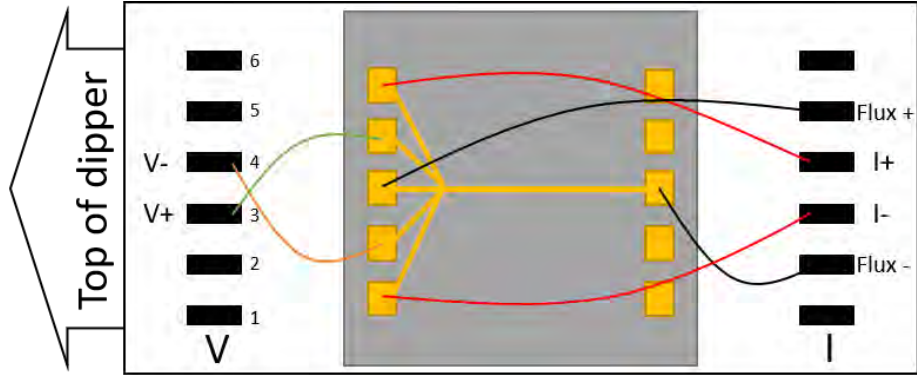


Figure 6.6: *Wiring diagram for SQUID using QDI*: Wiring diagram for SQUID 1 mounted on QDI for measurement. Not all the contact pads on the chip are shown.

6.3 Measurement

The measurement procedure has several differences from the procedure discussed in the previous two chapters. The single pillar measurements were taken in field to generate a Fraunhofer pattern for each junction to extract the maximum critical current. The SQUID measurements on the other hand are taken in zero field since we are trying to look at the phase of the current through the junctions. To begin the measurement process we first need to make connections to the SQUID. The connections are different than that of the single junctions since we measure one SQUID at a time as opposed to six junctions per dip.

Figure 6.6 show a wiring diagram for use when measuring a SQUID on QD-I. This particular wiring scheme is for measuring SQUID 1 of the ULI SQUID mask. The red lines are the sample current lines. The green and orange lines are the sample voltage lines. The black lines are the flux lines. To measure the rest of the SQUIDs on the sample all the connections must be moved except for the flux line leads. Since most of the wires are copper they must be replaced frequently except for the superconducting voltage leads. To replace the copper wires you must first remove the insulation from the new copper wires. The superconducting wire has insulation while the flux and current wires are bare. The

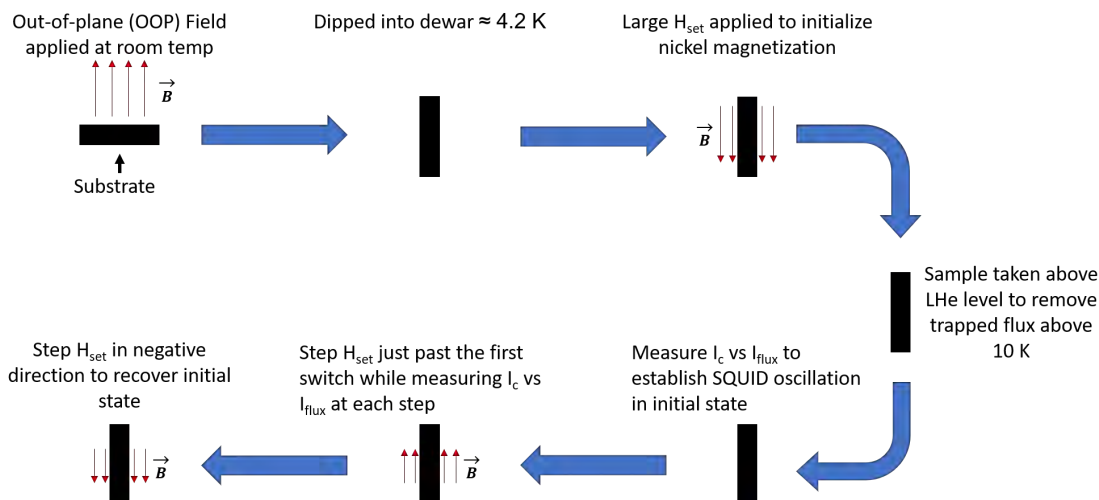


Figure 6.7: *Measurement Flow Diagram*: Flow diagram going clockwise from the top left.

superconducting wires are connected to a Quantum Design SQUID mounted inside the Quick Dipper. Since these wires are connected to a SQUID special care needs to be taken when connecting and handling them. The wires must lay flat and avoid having loops as well as being smooth avoiding any bends.

Figure 6.7 shows a flow diagram of our measurement procedure for the SQUIDs. For samples that contain a PMA multilayer as one of the ferromagnets we first initialize the samples with a field pointing out of plane. A strong permanent magnet is used to initialize the samples at room temperature by lowering the sample mounted on the dipper over the magnet. The dipper is then lowered slowly into the dewar filled with liquid helium. Just as before the Ni must be initialized in-plane using the external magnetic field H_{set} . We tried initialization values between 1200 and 3000 Oe, but it was not clear which value produced the optimal magnetic behavior of the samples. Then the probe is lifted up slowly until the sample is slightly above the liquid helium level, at which point the sample goes normal and trapped magnetic flux is removed. After the sample is lowered back into the liquid helium, we measure I_c vs I_{flux} to observe SQUID oscillations. We then start stepping the in-plane

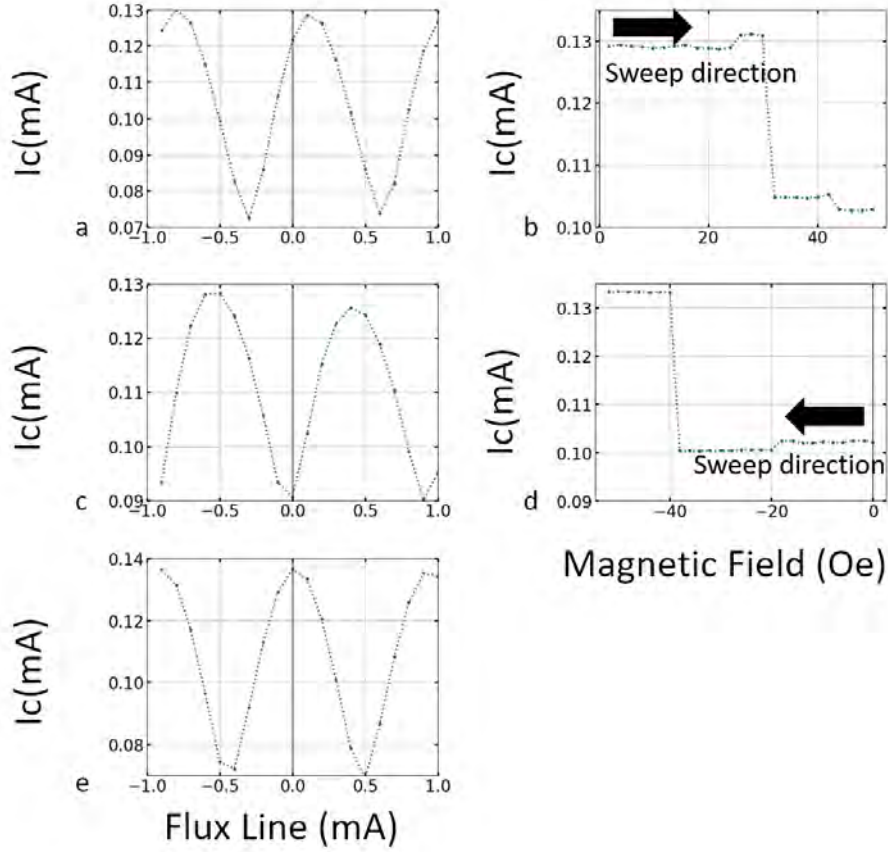


Figure 6.8: *Initial measurements*: A. Initial flux line sweep after initializing sample. B. First magnetic field sweep to measure first junction switch. C. Second flux sweep to check for phase switch. D. Second field sweep to switch back to initial state. E. Final flux sweep to compare to initial state. In this run, the phase of the final state differs slightly from the phase of the initial state.

field H_{set} in the direction opposite to the initialization direction, while measuring I_c vs I_{flux} at each step. If all goes well, the SQUID oscillations suddenly shift by π , indicating that one of the two junctions has switched from the 0-state to the π -state or vice versa. Finally, H_{set} is stepped in the opposite direction to bring the SQUID back to its initial state.

Figure 6.8 shows a series of measurements. In panel a, we first sweep the flux line from negative to positive to get a baseline for the SQUID oscillation. In panel b, we step the in-plane field in the opposite direction of the initialization to try to switch the soft magnetic layer of one of the junctions without switching the other junction. To save time in these

initial measurements we do not measure the SQUID oscillation at each field step. Instead, we take a series of IV curves at each step while keeping the flux line fixed at a maximum or minimum value of the SQUID oscillation. While stepping H_{set} we wait for the first switch of the junction and we measure a change in I_c . Once the switch happens, panel c shows a flux sweep measurement to see if the sample underwent a π phase shift. In panel d, we step the field back in the other direction to recover the initial state. When that occurs we can take a final flux sweep, part e, to verify we are back to the original state. These initial measurements will give the parameters for the much more time consuming waterfall plots. The waterfall plots can take several hours so careful monitoring of the measurements may be needed in order to assure proper switching. Note that panels a and e in Figure 6.8 do not match perfectly. The second phase change from c to e is much closer to π than the first phase change from a to c. This happens often, but the behavior of the samples often improves with repeated cycling through the field-stepping procedure.

6.4 Results

To better understand these samples we have chosen to present the data as 3d plots where the x and y axis are flux current and magnetic field H_{set} and the z axis is the critical current. Waterfall plots will give a clear indication of switches and phase information when reported this way. The waterfall plots will show when we have clear SQUID oscillations by showing a progression of peaks and valleys following along the same flux line current value. When a π phase switch occurs the peaks should go to where valleys were and vice versa for the valleys. Figure 6.9 shows an example of a waterfall plot with promising results. This sample was initialized at 3000 Oe. The measurement was then made by stepping H_{set} in the negative

direction. First, we notice the sample undergoes a π phase switch at about -25 Oe. Following the first switch we see another switch occurring above 60 Oe. This switch may be due to the Py in the hexagonal pillar switching. The measurement is then taken in the positive direction and we notice another π switch near 25 Oe. This SQUID showed a maximum critical current near $35 \mu\text{A}$, which is significantly higher than the $10 \mu\text{A}$ critical currents observed in the previous triplet PMA-SAF SQUIDs measured by Joseph Glick.

After initialization, both junctions in the SQUID should be in the parallel state, meaning the magnetizations of the Py free layer and Ni fixed layer are parallel. After the first switch, the elliptical junction should be in the antiparallel state. Theory suggests that the parallel state is expected to have the same critical current as the anti-parallel state, but due to a small field shift of the Fraunhofer pattern we might expect the parallel-state critical current to be smaller than the antiparallel-state critical current. In our experiments we have seen many samples where one state has higher current than the other state. Although there is an increase in the critical current through the triplet PMA SQUIDs when compared to the triplet PMA-SAF SQUIDs we do see a detriment in the magnetic behavior of these samples. Measurement of the samples show clear phase shifts but with some slight phase slipping in both directions. Depending on how the triplet PMA samples are initialized greatly effects the overall characteristics of the samples. We do see some of the expected results where we can measure higher critical current in the anti-parallel state after the first switch occurs in the Py layer of the elliptical junction. In Figure 6.9, the critical current for the anti-parallel state is more than $35\mu\text{A}$. The parallel state initially gave about $27\mu\text{A}$ and the final parallel state gave about $15\mu\text{A}$. Although the critical current is not the same in the initial and final state the phase looks to have been recovered after the switching of the Py layer. The samples that Joseph Glick fabricated which contained triplet PMA-SAF junctions gave critical currents

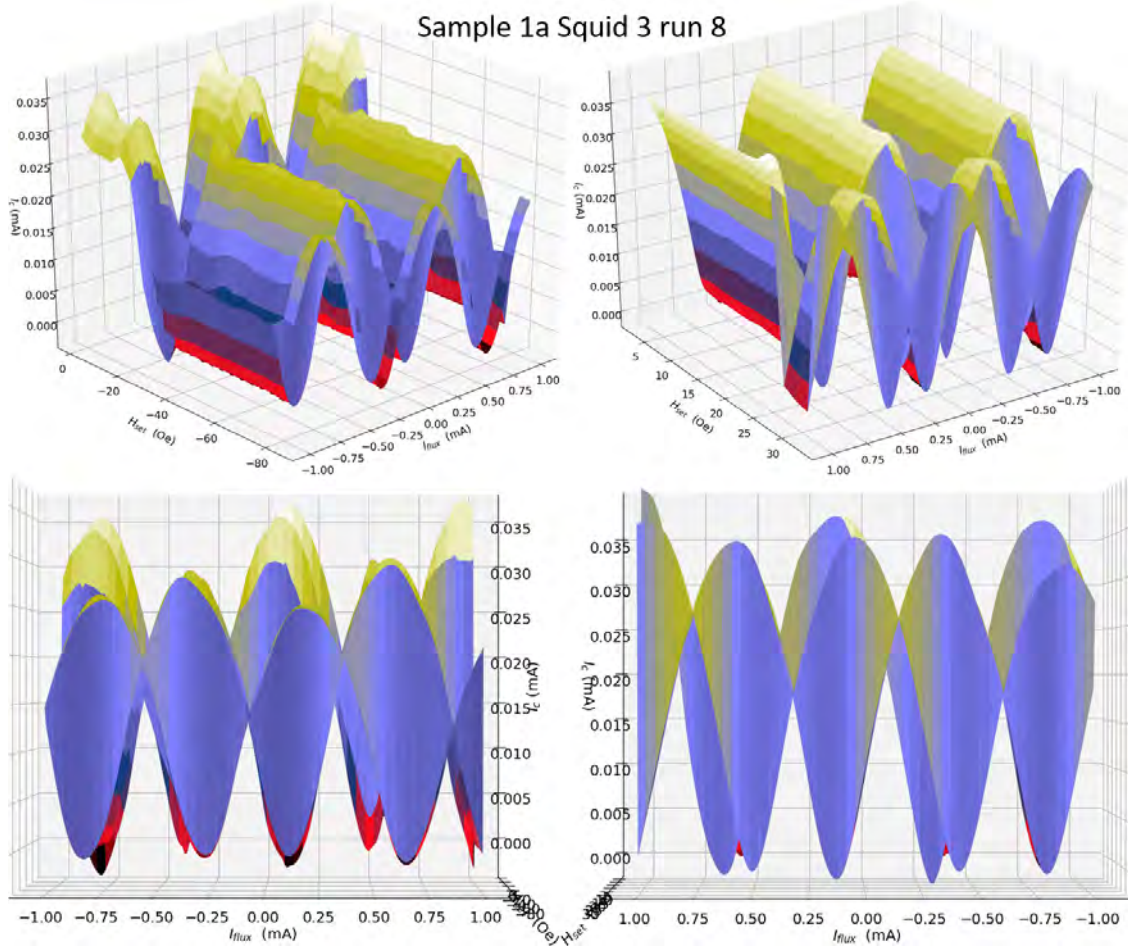


Figure 6.9: *Sample 1a SQUID 3 before training*: Sample 1a contains Py(1.2), Pd/Co repeats of N=2 and Ni(1.2) for the ferromagnetic layers. The sample was measured with an initialization field of 3000Oe. Left panels: H_{set} is swept in the negative direction to switch one of the junctions in the SQUID from the π -state to the 0-state. Right panels: H_{set} is swept in the positive direction to switch back to the initial state. Magnetic switching is observed at fields near 25 Oe in both sweep directions. We observe critical current values of up to $35\mu\text{A}$.

near $10\mu\text{A}$ [93].

After seeing that the initialization as well as the measurement can affect the behavior of the samples we decided to initialize the sample as before but then we switched the Py free layer back and forth several times using H_{set} . In most measurements the switch was done up to 20 times but we see more consistent switching with just 10. We describe some of the measurements below as the samples were measured before and after training of the

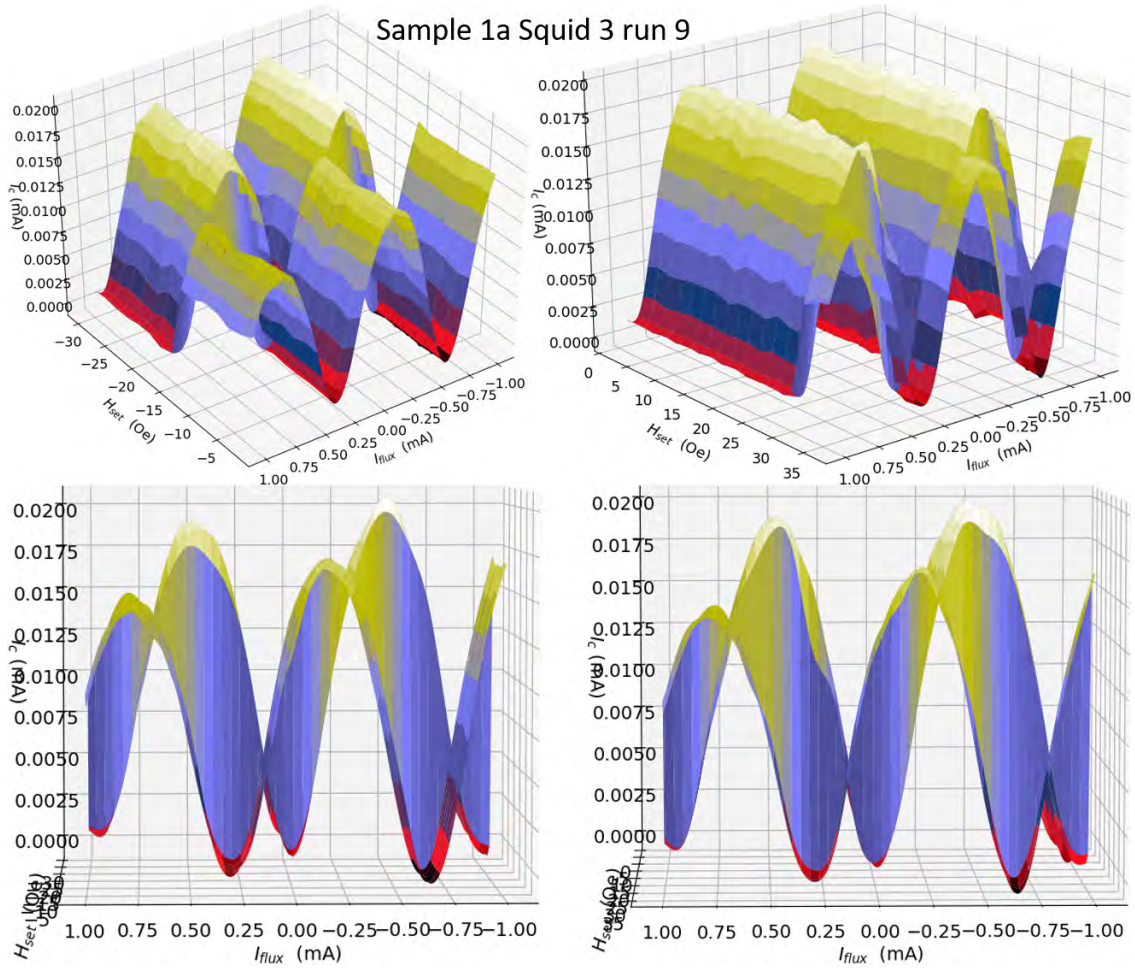


Figure 6.10: *Sample 1a SQUID 3 after training*: Sample 1a is the same sample as in the previous figure. The sample training was done in the same cooldown and followed the previous sample measurement. We can see improvements to the magnetics, no phase slipping, in this sample after training but we also notice a decrease in the critical current to about $20\mu\text{A}$.

junctions.

Figure 6.10 shows data from the same SQUID sample in a separate cool-down. The SQUID gave different results after it was trained by making the Py layer perform several switches. We see that the critical current has dropped to about $20\mu\text{A}$ when compared to the previous anti-parallel state. The switching behavior appears to be much cleaner but now we also see that the phase shift is not as close to π .

Figure 6.11 shows data from one of the first samples measured. In this figure we see that

Sample 1a Squid 1 run 6

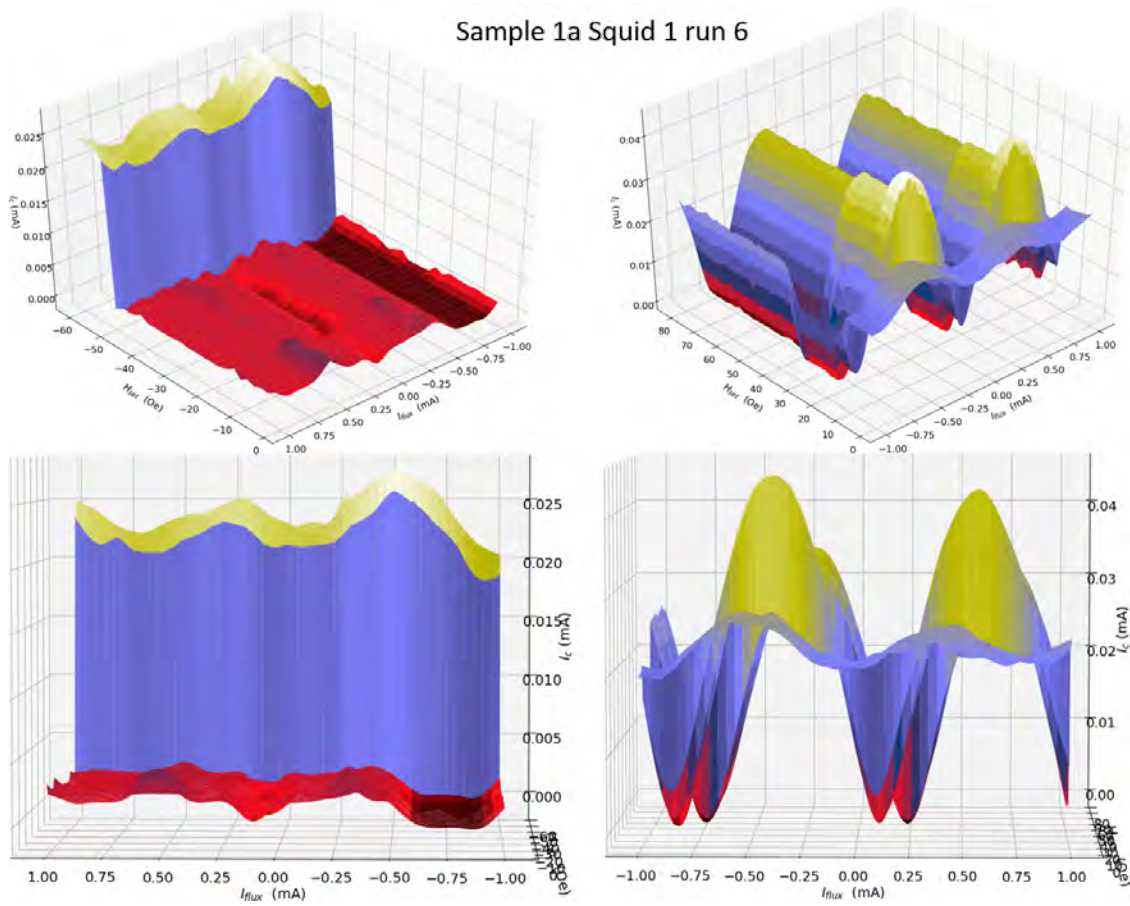


Figure 6.11: *Sample 1a SQUID 1*: Sample 1a SQUID 1 run6 shows the initial negative sweep to behave poorly in terms of magnetics. The positive sweep starts to behave better magnetically after switching back from the negative sweep. We observe critical currents near $45\mu\text{A}$.

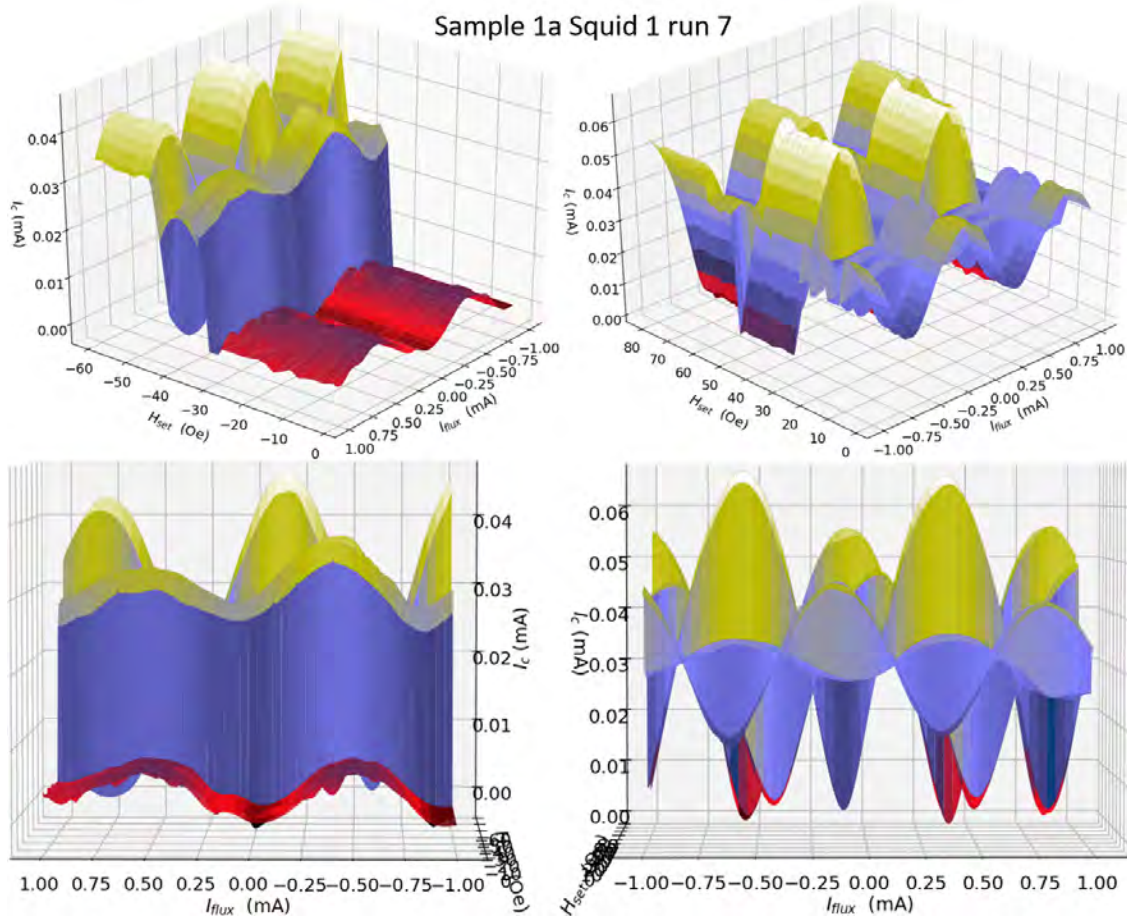


Figure 6.12: *Sample 1a SQUID 1*: This measurement was taken after the previous figure measurement. These initial improvements seen in these measurements were motivation used to start training the following samples. We seen a significant increase in critical current compared to the previous measurement. Critical current values are as high as $60\mu\text{A}$.

on the negative sweep there are initially very small SQUID oscillations, then a large jump in critical current after the first switch. On the positive sweep we can see improvements in the magnetics and cleaner SQUID oscillations. There are several places where we have phase slipping but never really have a π phase change.

Figure 6.12 now shows what some training can do to improve the magnetics of a sample. This measurement was taken after some training where we swept H_{set} up and down causing the soft-layer to toggle several times while trying to keep the hard layer fixed. Improvements in critical current and magnetics were seen. The switching behavior was not quite π but

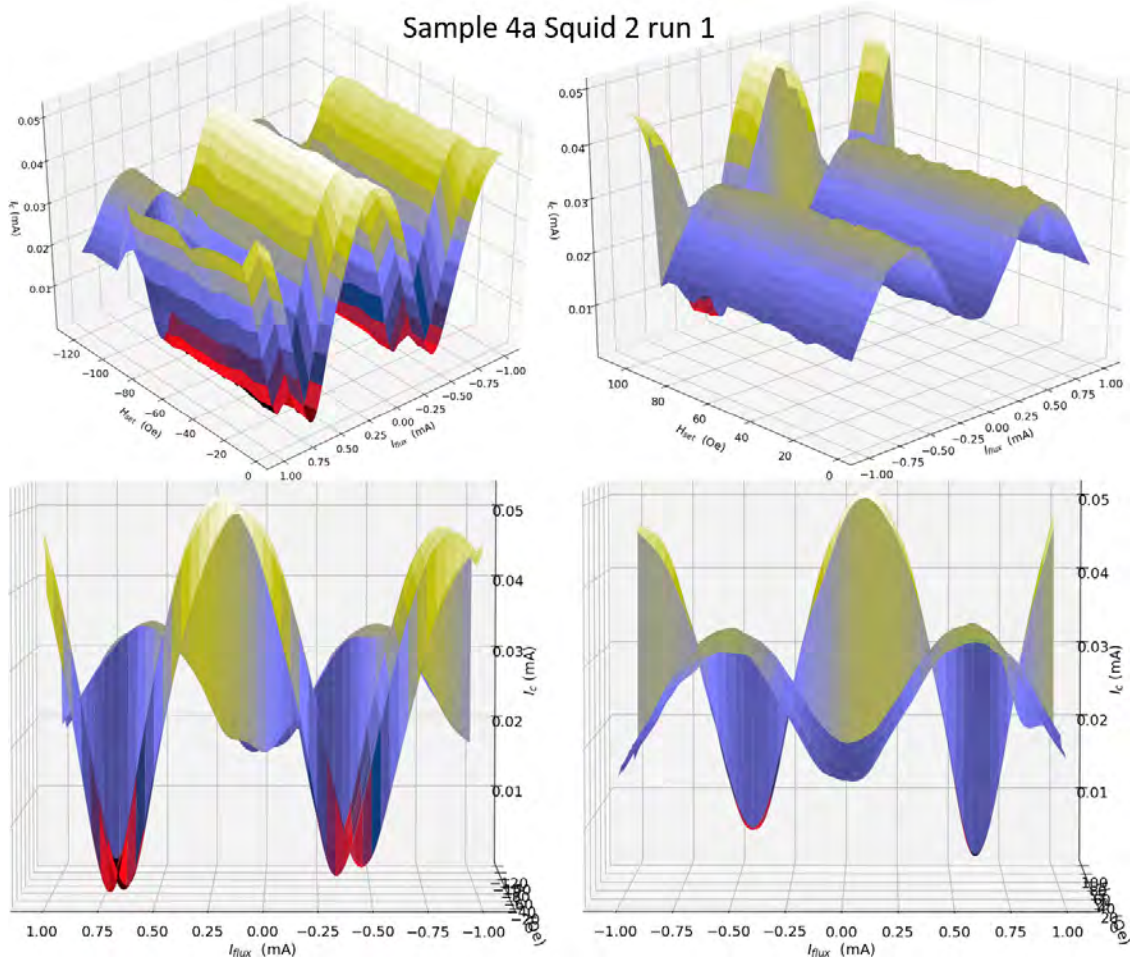


Figure 6.13: *Sample 4a SQUID 2*: This sample was measured after the training process. We see phase slipping in the negative sweep direction but very clean SQUID oscillations in the positive sweep direction. The switching field for this SQUID is rather high – about 80 Oe in both sweep directions.

in showed improvement over the initial measurements. One surprise in this sample is that we observe two distinct π phase changes in both sweep directions. We attribute the second switch to the Py layer in the hexagonal junction switching.

In figure 6.13 we see close to $0-\pi$ switching in both the positive and negative sweeps. There is some phase slipping in the negative directions hinting at possible issues with the magnetization of the Ni layer. The positive sweep looks very promising showing great switching with limited phase slipping.

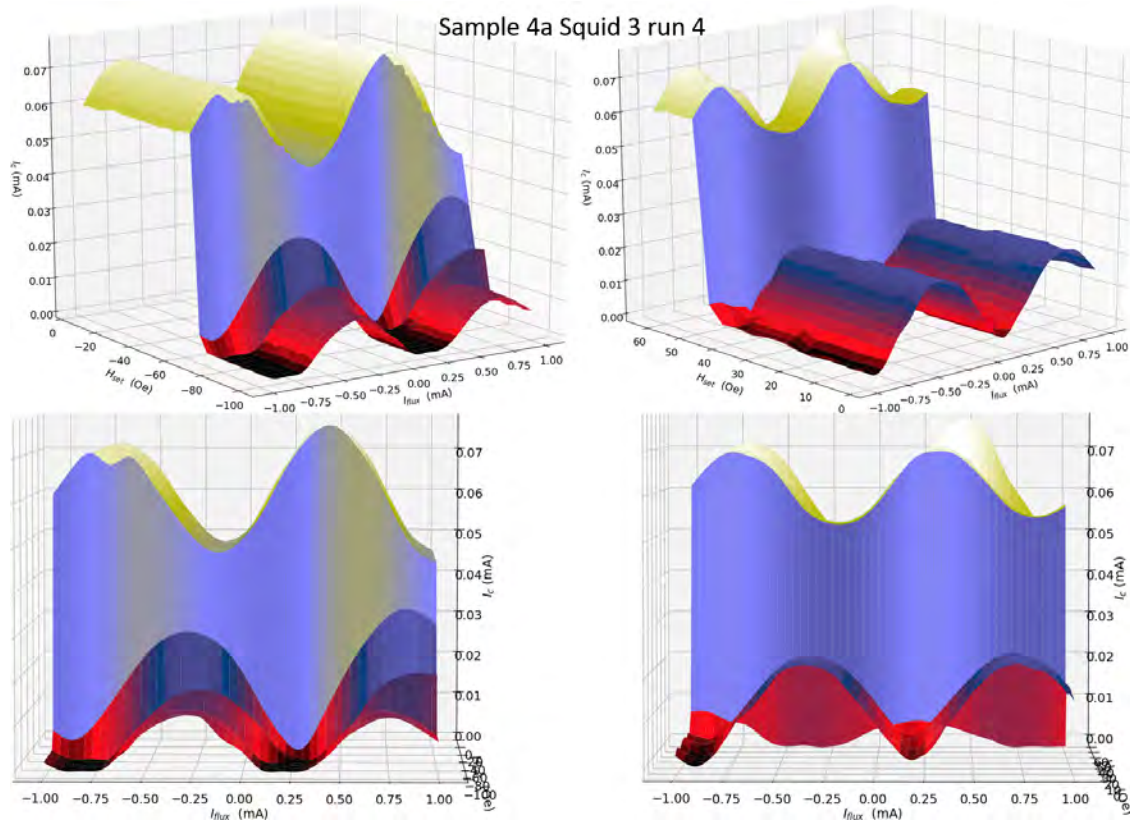


Figure 6.14: *Sample 4a SQUID 3*: This sample is measured after the training process. The critical current has a large offset (i.e. it never approaches zero) in the higher critical current state indicating that the critical currents of the two junctions in the SQUID are quite different. There are clear switches in both the positive and negative sweep directions which are nearly $0-\pi$ switching.

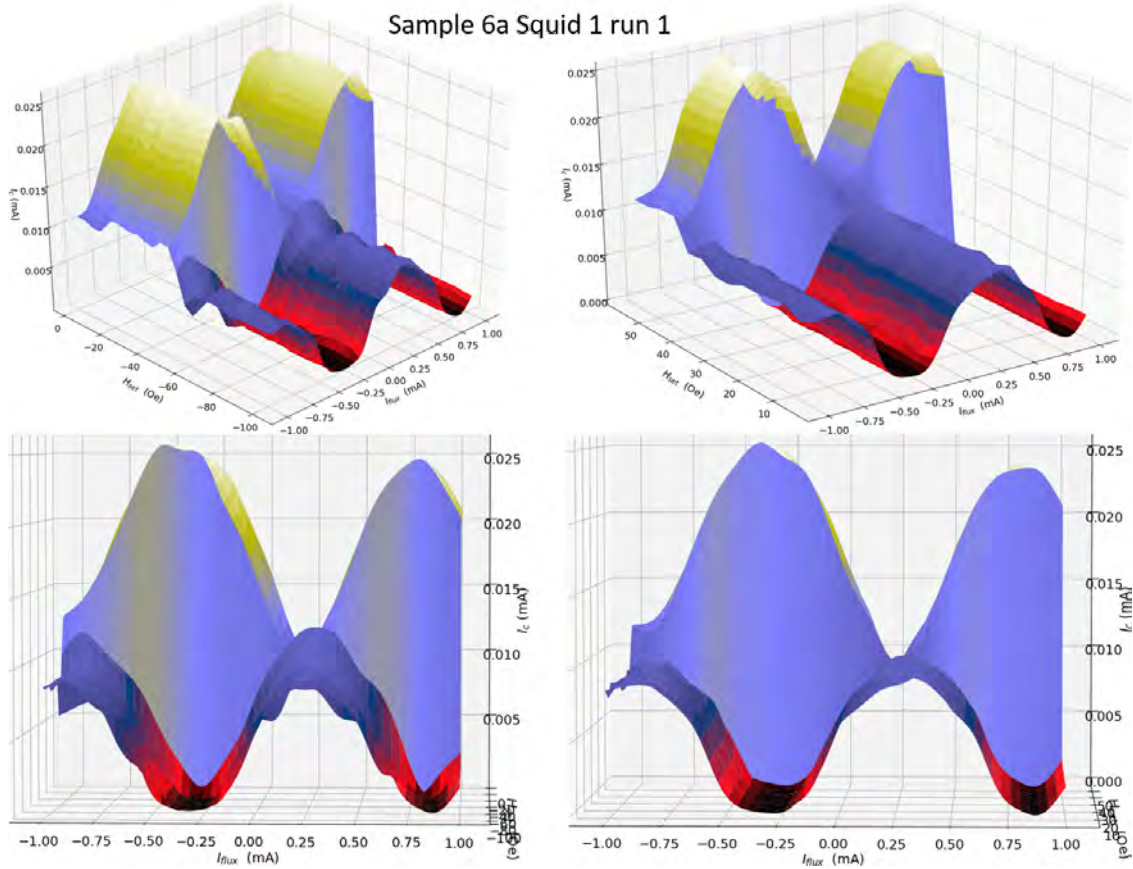


Figure 6.15: *Sample 6a SQUID 1*: This sample shows a similar offset to the previous sample. The higher critical current state is offset by about $10\mu\text{A}$. We do notice that there is some $0-\pi$ switching in this sample. This sample also shows very little phase slipping.

In figure 6.14 we see nearly $0-\pi$ switching in both the positive and negative sweeps. These sweeps show a large difference in the critical currents in the parallel and anti-parallel states. There is some limited phase slipping. We also notice a large critical current in this sample as high as $70\mu\text{A}$.

In figure 6.15 we see some great switching, essentially π , in both directions. The sample also has almost no phase slipping. Unfortunately, the critical current is smaller than expected even with reasonable resistance values as seen in Table 6.3.

The following three tables summarize the properties of all the SQUID samples measured in this work.

Table 6.1: *Sample parameters for each ferromagnetic layer.* The Py for all samples is 1.2 nm in thickness. The PMA layers consist of Pd/Co repeats that are 0.9 nm and 0.3 nm respectively. The Ni layer is either 1.2 nm or 2.0 nm in thickness.

Sample	Py (nm)	Pd/Co repeats (N)	Ni (nm)
1a	1.2	2	1.2
3a	1.2	2	2
4a	1.2	4	1.2
6a	1.2	4	2

Table 6.2: *Maximum measured critical current for each sample.* These are the maximum critical currents for each sample. The asterisks indicate samples that were measured for initial flux sweeps but not waterfall 3d plots. NA samples were not measured.

Maximum critical current (μA)	Squid 1	Squid 2	Squid 3	Squid 4
1a	64	NA	35	Bad
3a	79*	100*	NA	NA
4a	53	51	78	NA
6a	26	NA	16*	NA

6.5 Conclusions

This chapter shows the initial steps taken to verify proper control of the magnetic layers in the triplet PMA Josephson junctions. We presented the design of the SQUIDS used in the experiment and show where the flux line is and how it couples magnetic flux into the SQUID loop. We presented the exploratory measurements used to test whether a sample is working properly as well as to find parameters to be used in the setup process for the 3d waterfall plots. Finally we show the 3d waterfall plots of a sample where the data was taken in a single dip. As expected from the single-junction results discussed in the previous

Table 6.3: *Sample resistance in $m\Omega$ for each sample from fit using lowest critical current value. Asterisk samples had initial flux sweeps measured but not waterfall 3d plots. The Py for all samples is 1.2 nm in thickness. The PMA layers consist of Pd/Co repeats that are 0.9 nm and 0.3 nm respectively. The Ni layer is either 1.2 nm or 2.0 nm in thickness.*

Resistance ($m\Omega$)	Squid 1	Squid 2	Squid 3	Squid 4
1a	7.2		13	
3a	0.97*	7.6*		
4a	10	11	7.4	
6a	9.6		8.7*	

chapter, the SQUIDS made from triplet PMA junctions show higher critical current when compared to the triplet PMA-SAF SQUIDS measured previously by Joseph Glick. However, the higher critical current comes with a detriment to the magnetics in the sample. Often, the samples did not show clean $0-\pi$ switching and high critical current in the same run. We suspect that the problem is that the central PMA multilayer causes stray magnetic fields that can interfere with magnetic behavior of the F' and F'' layers. In the PMA-SAF system we have, in the best conditions, a complete cancellation of any out-of-plane fields caused by the middle layer. This means that in terms of magnetics the PMA-SAF system is superior for reproducible phase control. The PMA system on the other had has better triplet supercurrent propagation but with inconsistent magnetics. We hoped that the PMA multilayers would generate stray fields only along the edges of the junction since the MFM images showed single domain behavior. If that were the case the stray field effect would have not played such a strong role in the magnetic behavior of the junctions.

Chapter 7

Conclusions and outlook

In this chapter we will summarize the work discussed in the previous chapters and elaborate on some previously talked about points. We also mention what the goals of this work were when we first began along with what we accomplished along the way. Finally we look at where we are with this work and possible future plans for spin triplet Josephson junctions.

We start in Chapter 1 where we introduced important concepts and some of the motivation and overall goals of this work. The idea of being able to reduce the strain of energy cost for computer storage was one of the main driving forces and long term goals we are looking to attain.

Chapter 2 goes into details about the interplay of superconductivity and ferromagnetism that govern our Josephson junctions. There are many theoretical concepts that are presented which play important roles in our experiments. We also introduced some nomenclature that was throughout the rest of the chapters. We also briefly explained how our phase measurements using SQUIDs can be understood.

Chapter 3 explained in detail the fabrication and measurement processes of our samples. We discussed the initial investigative procedures of characterizing materials that are used for the experiment which must be done before any samples are fabricated. The characterizing of materials for Josephson junctions may include patterning of arrays for magnetic measurement, which was also briefly mentioned in this chapter. We go through step-by-step instructions for the fabrication process of the junctions including small details that are

specific to the fabrication of spin triplet Josephson junctions. This chapter also mentions details about the measurement sequences and sputtering chambers that are used in our lab. One sputtering chamber is used for most of the sample fabrication. The smaller sputtering chamber(Rezanator) is used more for exploratory physics.

Chapter 4 goes into details comparing the Shuffled and spin triplet Josephson junctions using a PMA-SAF as the central ferromagnet. Comparing the decay and amplitude differences of the supercurrent in the triplet and shuffled junctions gives us strong confirmation of the presence of the spin triplet supercurrent generation in spin-triplet Josephson junctions. Once this was established we could move on to the next step which was to optimize the propagation of triplet supercurrent. For completeness we mention the reason behind fabricating samples that had two thickness of Ni. This was done to avoid the possibility that the shuffled junctions may have had the two adjacent Ni layers combine to fall on a $0-\pi$ minimum. If this were the case for the shuffled junctions we could have measured a critical current near zero. For that case we could not have compared the supercurrents of these two junctions correctly.

In chapter 5 we showed data on samples what were fabricated with either a PMA-SAF or a PMA stack as the central ferromagnetic layer. In the previous chapter, chapter 4, we had shown that spin triplet pairs were the dominant contribution to the supercurrent in these junctions, but since the critical current was smaller than we needed we planned to find a way to fabricate junctions that could propagate more triplet supercurrent. We introduced the PMA multilayer in place of the PMA-SAF and fabricated both kinds of junctions at the same time for direct comparison. We observed larger supercurrent in the PMA junctions, and we discussed what could be causing the suppression of triplet supercurrent in the PMA-SAF junctions. Once we obtained junctions with higher critical current we were able to move on to the next step of the project.

In chapter 6 we presented measurements of several SQUID samples that had different ferromagnetic layer thicknesses, using different initialization procedures. In this chapter we were trying to show phase control in the spin triplet junctions along with increasing critical current propagation. The results of this chapter did show phase control in some cases after some extensive initialization procedures. The critical current in some cases were significantly higher when compared to previous work done on PMA-SAF samples. The possibility of having both high critical current and phase control proved to be more illusive than with the PMA-SAF samples. The samples with large critical current had no phase control until they were taken through an extensive initialization procedure. Some samples then showed great phase control but had smaller critical current than expected although still larger than similar samples with PMA-SAFs.

Although we were unable to measure samples that had good phase control along with high critical current the possibility still exists that finding better initialization procedures for aligning both the PMA layers as well as the nickel layers may be able to produce better behaving samples. We believe that the current samples may have had stray fields from the PMA layer that caused detrimental behavior when coupled with the nickel layers, giving lower critical current or bad magnetic behavior.

A exciting prospect for further expanding this work is to create a so-called ϕ_0 junction, where the ground-state phase difference across the junction can have an arbitrary value, not just zero or π [106–113]. Theory predicts that one can achieve a ϕ_0 junction using a spin-triplet junction of the kind discussed in this thesis, but with an arbitrary angle between the magnetizations of the top Ni fixed layer and the bottom NiFe free layer. To achieve such a state we would fabricate a new type of junction that has no shape anisotropy. The pattern of the junction would no longer be shaped as an ellipse but would be a circle. The junction

would contain a similar stack as the ones we have in the SQUID measurements from chapter 6. The patterning for that measurement would be to have one junction on the SQUID be hexagonal to not have any movement of any of the ferromagnetic layers in that stack while the other would be the circular junction where we could set the orientation of the NiFe free layer in any direction. The signature of the ϕ_0 junction would be SQUID oscillations with varying phase shift, depending on the magnetization angle set by the external field. To achieve this goal, the magnetics of such a junction would have to be very stable and reproducible. Not only would the physics a ϕ_0 junction be interesting to explore but the practical application of a superconducting phase battery could be valuable in some future work [114–117].

APPENDIX

REFERENCES

REFERENCES

- [1] D. S. Holmes, A. L. Ripple, and M. A. Manheimer. Energy-efficient superconducting computing—power budgets and requirements. *IEEE Trans. Appl. Supercond.*, 23(3):1701610, 2013.
- [2] Edler T. Andrae ASG. On Global Electricity Usage of Communication Technology: Trends to 2030. *Challenges*, 6:117–157, 2015.
- [3] Dr. Ian Cutress. Intel’s manufacturing roadmap from 2019 to 2029: Back porting, 7nm, 5nm, 3nm, 2nm, and 1.4 nm. <https://www.anandtech.com/show/15217/intels-manufacturing-roadmap-from-2019-to-2029>, Dec 2019.
- [4] Erich Strohmaier, Horst Simon, Jack Dongarra, and Martin Meuer. Top500 expands exaflops capacity amidst low turnover. <https://www.top500.org/lists/top500/2020/11/press-release/>, Nov 2020.
- [5] Mark Halper. Supercomputing’s super energy needs, and what to do about them. <https://cacm.acm.org/news/192296-supercomputings-super-energy-needs-and-what-to-do-about-them/fulltext>, Sep 2015.
- [6] K. K. Likharev, O. A. Mukhanov, and V. K. Semenov. Resistive single flux quantum logic for the Josephson-junction digital technology. In *SQUID’85*, pages 1103–1108. Walter de Gruyter, Berlin, 1985.
- [7] T. Ortlepp, O. Wetzstein, S. Engert, J. Kunert, and H. Toepfer. Reduced Power Consumption in Superconducting Electronics. *IEEE Transactions on Applied Superconductivity*, 21(3):770–775, 2011.
- [8] M. Tanaka, A. Kitayama, T. Koketsu, M. Ito, and A. Fujimaki. Low-Energy Consumption RSFQ Circuits Driven by Low Voltages. *IEEE Transactions on Applied Superconductivity*, 23(3):1701104–1701104, 2013.
- [9] M H Volkmann, A Sahu, C J Fourie, and O A Mukhanov. Implementation of energy efficient single flux quantum digital circuits with sub-aJ/bit operation. *Superconductor Science and Technology*, 26(1):015002, nov 2012.
- [10] Q. P. Herr, A. Y. Herr, O. T. Oberg, and A. G. Ioannidis. Ultra-low-power superconductor logic. *J. App. Phys.*, 109(10):103903, 2011.

- [11] Naoki Takeuchi, Yuki Yamanashi, and Nobuyuki Yoshikawa. Energy efficiency of adiabatic superconductor logic. *Superconductor Science and Technology*, 28(1):015003, nov 2014.
- [12] C. Bell, G. Burnell, C. W. Leung, E. J. Tarte, D.-J. Kang, and M. G. Blamire. Controllable Josephson current through a pseudospin-valve structure. *Appl. Phys. Lett.*, 84(7):1153–1155, 2004.
- [13] V. V. Ryazanov, V. V. Bol’ginov, D. S. Sobanin, I. V. Vernik, S. K. Tolpygo, A. M. Kadin, and O. A. Mukhanov. Magnetic Josephson junction technology for digital and memory applications. *Physics Procedia*, 36:35–41, 2012.
- [14] T. I. Larkin, V. V. Bol’ginov, V. S. Stolyarov, V. V. Ryazanov, I. V. Vernik, S. K. Tolpygo, and O. A. Mukhanov. Ferromagnetic Josephson switching device with high characteristic voltage. *Appl. Phys. Lett.*, 100(22):222601, 2012.
- [15] I. V. Vernik, V. V. Bol’ginov, S. V. Bakurskiy, A. A. Golubov, M. Y. Kupriyanov, V. V. Ryazanov, and O. A. Mukhanov. Magnetic Josephson Junctions With Superconducting Interlayer for Cryogenic Memory. *IEEE Trans. Appl. Supercond.*, 23(3):1701208, 2013.
- [16] M. Abd El Qader, R. K. Singh, S. N. Galvin, L. Yu, J. M. Rowell, and N. Newman. Switching at small magnetic fields in Josephson junctions fabricated with ferromagnetic barrier layers. *Appl. Phys. Lett.*, 104(2):022602, 2014.
- [17] B. Baek, W. H. Rippard, S. P. Benz, S. E. Russek, and P. D. Dresselhaus. Hybrid superconducting-magnetic memory device using competing order parameters. *Nat. Commun.*, 5:3888, 2014.
- [18] E. C. Gingrich, B. M. Niedzielski, J. A. Glick, Y. Wang, D. L. Miller, R. Loloee, W. P. Pratt Jr., and N. O. Birge. Controllable $0 - \pi$ Josephson junctions containing a ferromagnetic spin valve. *Nat. Phys.*, 12(6):564–567, 2016.
- [19] Joseph A. Glick, Mazin A. Khasawneh, Bethany M. Niedzielski, Reza Loloee, W. P. Pratt, Norman O. Birge, E. C. Gingrich, P. G. Kotula, and N. Missert. Critical current oscillations of elliptical josephson junctions with single-domain ferromagnetic layers. *Journal of Applied Physics*, 122(13):133906, 2017.
- [20] J. A. Glick, R. Loloee, W. P. Pratt, and N. O. Birge. Critical current oscillations of Josephson junctions containing PdFe nanomagnets. *IEEE Trans. App. Supercond.*, 27(4):1–5, 2017.
- [21] J. A. Glick, S. Edwards, D. Korucu, V. Aguilar, B. M. Niedzielski, R. Loloee, W. P. Pratt Jr., N. O. Birge, P. G. Kotula, and N. Missert. Spin-triplet supercurrent in Josephson junctions containing a synthetic antiferromagnet with perpendicular magnetic anisotropy. *arXiv:1710.07247*, 2017.

- [22] Victor Aguilar, Demet Korucu, Joseph A. Glick, Reza Loloee, W. P. Pratt, and Norman O. Birge. Spin-polarized triplet supercurrent in Josephson junctions with perpendicular ferromagnetic layers. *Phys. Rev. B*, 102:024518, Jul 2020.
- [23] I. M. Dayton, T. Sage, E. C. Gingrich, M. G. Loving, T. F. Ambrose, N. P. Siwak, S. Keebaugh, C. Kirby, D. L. Miller, A. Y. Herr, Q. P. Herr, and O. Naaman. Experimental demonstration of a josephson magnetic memory cell with a programmable π -junction. *IEEE Magnetics Letters*, 9:1–5, 2018.
- [24] Alexander E Madden, Joshua C Willard, Reza Loloee, and Norman O Birge. Phase controllable Josephson junctions for cryogenic memory. *Superconductor Science and Technology*, 32(1):015001, nov 2018.
- [25] Bethany M. Niedzielski, T. J. Bertus, Joseph A. Glick, R. Loloee, W. P. Pratt, and Norman O. Birge. Spin-valve josephson junctions for cryogenic memory. *Phys. Rev. B*, 97:024517, Jan 2018.
- [26] B. M. Niedzielski, E. C. Gingrich, R. Loloee, W. P. Pratt Jr., and N. O. Birge. S/F/S Josephson junctions with single-domain ferromagnets for memory applications. *Supercond. Sci. Technol.*, 28(8):085012, 2015.
- [27] Joseph A. Glick, Victor Aguilar, Adel B. Gougam, Bethany M. Niedzielski, Eric C. Gingrich, Reza Loloee, William P. Pratt, and Norman O. Birge. Phase control in a spin-triplet SQUID. *Science Advances*, 4(7), 2018.
- [28] T. S. Khaire, M. A. Khasawneh, W. P. Pratt Jr., and N. O. Birge. Observation of Spin-Triplet Superconductivity in Co-Based Josephson Junctions. *Phys. Rev. Lett.*, 104:137002, 2010.
- [29] C. Klose, T. S. Khaire, Y. Wang, W. P. Pratt, N. O. Birge, B. J. McMorran, T. P. Ginley, J. A. Borchers, B. J. Kirby, B. B. Maranville, and J. Unguris. Optimization of spin-triplet supercurrent in ferromagnetic Josephson junctions. *Phys. Rev. Lett.*, 108:127002, 2012.
- [30] E. C. Gingrich, P. Quarterman, Y. Wang, R. Loloee, W. P. Pratt Jr., and N. O. Birge. Spin-triplet supercurrent in Co/Ni multilayer Josephson junctions with perpendicular anisotropy. *Phys. Rev. B*, 86:224506, 2012.
- [31] W. M. Martinez, W. P. Pratt Jr., and N. O. Birge. Amplitude Control of the Spin-Triplet Supercurrent in S/F/S Josephson Junctions. *Phys. Rev. Lett.*, 116:077001, 2016.
- [32] H. K. Onnes and K. Hof. *Commun. Phys. Lab. Univ. Leiden.*, 120b, 122b, 124c, 1911.

- [33] W. Meissner and R. Ochsenfeld. Ein neuer effekt bei eintritt der supraleitfähigkeit. *Naturwissenschaften*, 21(44):787–788, 1933.
- [34] J. Bardeen, L. N. Cooper, and J. R. Schrieffer. Microscopic theory of superconductivity. *Phys. Rev.*, 106(1):162, 1957.
- [35] J. Bardeen, L. N. Cooper, and J. R. Schrieffer. Theory of superconductivity. *Phys. Rev.*, 108(5):1175, 1957.
- [36] Jayaram Balasubramanyam, Mahesh Lohith K S, and Sujith Thomas. *Lecture Notes on Engineering Physics*. 01 2014.
- [37] Ashima Arora. *Optical and electric field control of magnetism*. PhD thesis, University of Potsdam, 01 2018.
- [38] A. F. Andreev. The thermal conductivity of the intermediate state in superconductors. *Sov. Phys. JETP.*, 46(5):1823–1828, 1964.
- [39] Lüth H. *Collective Phenomena at Interfaces: Superconductivity and Ferromagnetism*. Springer, 2015.
- [40] P. G. DE GENNES. Boundary Effects in Superconductors. *Rev. Mod. Phys.*, 36:225–237, Jan 1964.
- [41] G. Deutscher and P. G. De Gennes. *Superconductivity*, volume 2. Marcel Dekker, New York, 1969.
- [42] A. I. Buzdin, L. N. Bulaevskii, and S. V. Panyukov. Critical-current oscillations as a function of the exchange field and thickness of the ferromagnetic metal (F) in an S-F-S Josephson junction. *Pis'ma Zh. Eksp. Teor. Fiz.*, 35(4):147–148, 1982. [*J. Exp. Theor. Phys. Lett.*, **35**, 4, 20 (1982)].
- [43] A. I. Buzdin and M. Yu. Kupriyanov. Josephson junction with a ferromagnetic layer. *Pis'ma Zh. Eksp. Teor. Fiz.*, 53(6):308–312, 1991. [*J. Exp. Theor. Phys. Lett.*, **53**, 6, 321 (1991)].
- [44] Z. Radović, L. Dobrosavljević-Grujić, A. I. Buzdin, and John R. Clem. Upper critical fields of superconductor-ferromagnet multilayers. *Phys. Rev. B*, 38:2388–2393, Aug 1988.
- [45] Zoran Radović, Marko Ledvij, Ljiljana Dobrosavljević-Grujić, A. I. Buzdin, and John R. Clem. Transition temperatures of superconductor-ferromagnet superlattices. *Phys. Rev. B*, 44:759–764, Jul 1991.
- [46] E. A. Demler, G. B. Arnold, and M. R. Beasley. Superconducting proximity effects in magnetic metals. *Phys. Rev. B*, 55:15174–15182, 1997.

- [47] Lina S. Abdallah, Tarek M. Tawalbeh, Igor V. Vasiliev, Stefan Zollner, Christian Lavoie, Ahmet Ozcan, and Mark Raymond. Optical conductivity of $\text{Ni}_{1-x}\text{Pt}_x$ alloys ($0 < x < 0.25$) from 0.76 to 6.6 eV. *AIP Advances*, 4(1):017102, 2014.
- [48] A. I. Buzdin. Proximity effects in superconductor-ferromagnet heterostructures. *Rev. Mod. Phys.*, 77:935–976, 2005.
- [49] D. E. Eastman, F. J. Himpsel, and J. A. Knapp. Experimental Band Structure and Temperature-Dependent Magnetic Exchange Splitting of Nickel Using Angle-Resolved Photoemission. *Phys. Rev. Lett.*, 40:1514–1517, Jun 1978.
- [50] D. E. Eastman, F. J. Himpsel, and J. A. Knapp. Experimental Exchange-Split Energy-Band Dispersions for Fe, Co, and Ni. *Phys. Rev. Lett.*, 44:95–98, Jan 1980.
- [51] L. N. Bulaevskii, V. V. Kuzii, and A. A. Sobyanin. Superconducting system with weak coupling to the current in the ground state. *Sov. JETP Lett.*, 25(7):290–294, 1977.
- [52] V. V. Ryazanov, V. A. Oboznov, A. Yu. Rusanov, A. V. Veretennikov, A. A. Golubov, and J. Aarts. Coupling of two superconductors through a ferromagnet: Evidence for a π junction. *Phys. Rev. Lett.*, 86:2427–2430, Mar 2001.
- [53] Y. Blum, A. Tsukernik, M. Karpovski, and A. Palevski. Oscillations of the superconducting critical current in Nb-Cu-Ni-Cu-Nb junctions. *Phys. Rev. Lett.*, 89:187004, 2002.
- [54] T. Kontos, M. Aprili, J. Lesueur, F. Genêt, B. Stephanidis, and R. Boursier. Josephson Junction through a Thin Ferromagnetic Layer: Negative Coupling. *Phys. Rev. Lett.*, 89:137007, 2002.
- [55] H. Sellier, C. Baraduc, F. Lefloch, and R. Calemczuk. Temperature-induced crossover between 0 and π states in S/F/S junctions. *Phys. Rev. B*, 68:054531, 2003.
- [56] V. A. Oboznov, V. V. Bol’ginov, A. K. Feofanov, V. V. Ryazanov, and A. I. Buzdin. Thickness Dependence of the Josephson Ground States of Superconductor-Ferromagnet-Superconductor Junctions. *Phys. Rev. Lett.*, 96:197003, 2006.
- [57] J. W. A. Robinson, S. Piano, G. Burnell, C. Bell, and M. G. Blamire. Critical current oscillations in strong ferromagnetic π junctions. *Phys. Rev. Lett.*, 97:177003, 2006.
- [58] V. Shelukhin, A. Tsukernik, M. Karpovski, Y. Blum, K. B. Efetov, A. F. Volkov, T. Champel, M. Eschrig, T. Löfwander, G. Schön, and A. Palevski. Observation of periodic π -phase shifts in ferromagnet-superconductor multilayers. *Phys. Rev. B*, 73:174506, 2006.

- [59] M. Weides, M. Kemmler, E. Goldobin, D. Koelle, R. Kleiner, H. Kohlstedt, and A. Buzdin. High quality ferromagnetic 0 and π Josephson tunnel junctions. *Appl. Phys. Lett.*, 89:122511, 2006.
- [60] J. W. A. Robinson, S. Piano, G. Burnell, C. Bell, and M. G. Blamire. Zero to π transition in superconductor-ferromagnet-superconductor junctions. *Phys. Rev. B*, 76:094522, 2007.
- [61] A. A. Bannykh, J. Pfeiffer, V. S. Stolyarov, I. E. Batov, V. V. Ryazanov, and M. Weides. Josephson tunnel junctions with a strong ferromagnetic interlayer. *Phys. Rev. B*, 79:054501, 2009.
- [62] F. S. Bergeret, A. F. Volkov, and K. B. Efetov. Josephson current in superconductor-ferromagnet structures with a nonhomogeneous magnetization. *Phys. Rev. B*, 64:134506, 2001.
- [63] A. Kadigrobov, R. I. Shekhter, and M. Jonson. Quantum spin fluctuations as a source of long-range proximity effects in diffusive ferromagnet-superconductor structures. *EPL (Europhysics Letters)*, 54(3):394, 2001.
- [64] M. Eschrig, J. Kopu, J. C. Cuevas, and G. Schön. Theory of half-metal/superconductor heterostructures. *Phys. Rev. Lett.*, 90:137003, 2003.
- [65] A. F. Volkov, F. S. Bergeret, and K. B. Efetov. Odd triplet superconductivity in superconductor-ferromagnet multilayered structures. *Phys. Rev. Lett.*, 90:117006, 2003.
- [66] F. S. Bergeret, A. F. Volkov, and K. B. Efetov. Odd triplet superconductivity and related phenomena in superconductor-ferromagnet structures. *Rev. Mod. Phys.*, 77:1321–1373, 2005.
- [67] R. S. Keizer, S. T. B. Goennenwein, T. M. Klapwijk, G. Miao, G. Xiao, and A. Gupta. A spin triplet supercurrent through the half-metallic ferromagnet CrO₂. *Nature*, 439(7078):825–827, 2006.
- [68] I. Sosnin, H. Cho, V. T. Petrashov, and A. F. Volkov. Superconducting phase coherent electron transport in proximity conical ferromagnets. *Phys. Rev. Lett.*, 96:157002, 2006.
- [69] J. W. A. Robinson, J. D. S. Witt, and M. G. Blamire. Controlled Injection of Spin-Triplet Supercurrents into a Strong Ferromagnet. *Science*, 329(5987):59–61, 2010.
- [70] D. Sprungmann, K. Westerholt, H. Zabel, M. Weides, and H. Kohlstedt. Evidence for triplet superconductivity in Josephson junctions with barriers of the ferromagnetic Heusler alloy Cu₂MnAl. *Phys. Rev. B*, 82:060505, 2010.

- [71] M. S. Anwar, F. Czeschka, M. Hesselberth, M. Porcu, and J. Aarts. Long-range supercurrents through half-metallic ferromagnetic CrO₂. *Phys. Rev. B*, 82:100501, 2010.
- [72] J. Wang, M. Singh, M. Tian, N. Kumar, B. Liu, C. Shi, J. K. Jain, N. Samarth, T. E. Mallouk, and M. H. W. Chan. Interplay between superconductivity and ferromagnetism in crystalline nanowires. *Nat. Phys.*, 6(5):389–394, 2010.
- [73] P. V. Leksin, N. N. Garif’yanov, I. A. Garifullin, Ya. V. Fominov, J. Schumann, Y. Krupskaya, V. Kataev, O. G. Schmidt, and B. Büchner. Evidence for triplet superconductivity in a superconductor-ferromagnet spin valve. *Phys. Rev. Lett.*, 109:057005, 2012.
- [74] V. I. Zdravkov, J. Kehrle, G. Obermeier, D. Lenk, H.-A. Krug von Nidda, C. Müller, M. Yu. Kupriyanov, A. S. Sidorenko, S. Horn, R. Tidecks, and L. R. Tagirov. Experimental observation of the triplet spin-valve effect in a superconductor-ferromagnet heterostructure. *Phys. Rev. B*, 87:144507, 2013.
- [75] N. Banerjee, C. B. Smiet, R. G. J. Smits, A. Ozaeta, F. S. Bergeret, M. G. Blamire, and J. W. A. Robinson. Evidence for spin selectivity of triplet pairs in superconducting spin valves. *Nat. Commun.*, 5:3048, 2014.
- [76] N. Banerjee, J. W. A. Robinson, and M. G. Blamire. Reversible control of spin-polarized supercurrents in ferromagnetic Josephson junctions. *Nat. Commun.*, 5:4771 EP, 2014.
- [77] A. Iovan, T. Golod, and V. M. Krasnov. Controllable generation of a spin-triplet supercurrent in a Josephson spin valve. *Phys. Rev. B*, 90:134514, 2014.
- [78] X. L. Wang, A. Di Bernardo, N. Banerjee, A. Wells, F. S. Bergeret, M. G. Blamire, and J. W. A. Robinson. Giant triplet proximity effect in superconducting pseudo spin valves with engineered anisotropy. *Phys. Rev. B*, 89:140508, 2014.
- [79] A. A. Jara, C. Safranski, I. N. Krivorotov, C. Wu, A. N. Malmi-Kakkada, O. T. Valls, and K. Halterman. Angular dependence of superconductivity in superconductor/spin-valve heterostructures. *Phys. Rev. B*, 89:184502, 2014.
- [80] M. G. Flokstra, T. C. Cunningham, J. Kim, N. Satchell, G. Burnell, P. J. Curran, S. J. Bending, C. J. Kinane, J. F. K. Cooper, S. Langridge, A. Isidori, N. Pugach, M. Eschrig, and S. L. Lee. Controlled suppression of superconductivity by the generation of polarized Cooper pairs in spin-valve structures. *Phys. Rev. B*, 91:060501, 2015.
- [81] A. Singh, S. Voltan, K. Lahabi, and J. Aarts. Colossal Proximity Effect in a Superconducting Triplet Spin Valve Based on the Half-Metallic Ferromagnet CrO₂. *Phys. Rev. X*, 5:021019, 2015.

- [82] J. Linder and J. W. A. Robinson. Superconducting spintronics. *Nat. Phys.*, 11(4):307–315, 2015.
- [83] M. Eschrig. Spin-polarized supercurrents for spintronics: a review of current progress. *Rep. Prog. Phys.*, 78(10):104501, 2015.
- [84] A. Di Bernardo, S. Diesch, Y. Gu, J. Linder, G. Divitini, C. Ducati, E. Scheer, M. G. Blamire, and J. W. A. Robinson. Signature of magnetic-dependent gapless odd frequency states at superconductor/ferromagnet interfaces. *Nat. Commun.*, 6:8053, 2015.
- [85] Z. Feng, J. W. A. Robinson, and M. G. Blamire. Out of plane superconducting Nb/Cu/Ni/Cu/Co triplet spin-valves. *Appl. Phys. Lett.*, 111(4):042602, 2017.
- [86] C. Cirillo, S. Voltan, E. A. Ilyina, J. M. Hernandez, A. Garcia-Santiago, J. Aarts, and C. Attanasio. Long-range proximity effect in Nb-based heterostructures induced by a magnetically inhomogeneous permalloy layer. *New J. Phys.*, 19(2):023037, 2017.
- [87] M. Houzet and A. I. Buzdin. Long range triplet Josephson effect through a ferromagnetic trilayer. *Phys. Rev. B*, 76:060504, 2007.
- [88] M. Eschrig. Spin-polarized supercurrents for spintronics. *Phys. Today*, 64:43, 2011.
- [89] R. C. Jaklevic, John Lambe, A. H. Silver, and J. E. Mercereau. Quantum Interference Effects in Josephson Tunneling. *Phys. Rev. Lett.*, 12:159–160, Feb 1964.
- [90] A. Barone and G. Paternò. *Physics and applications of the Josephson effect*. Wiley, 1982.
- [91] Boris Chesca, Reinhold Kleiner, and Dieter Koelle. *The SQUID Handbook, Volume 1*. Wiley-VCH Verlag GmbH & Co. KGaA, 2005.
- [92] R. de Bruyn Ouboter and A. Th. A. M. de Waele. Superconducting point contacts weakly connecting two superconductors. *Rev. Phys. Appl. (Paris)*, 5:25, 1970.
- [93] J. A. Glick. *Ferromagnetic Josephson Junctions Carrying Spin-Triplet Supercurrent For Cryogenic Memory*. PhD thesis, Michigan State University, 2017.
- [94] A. F. Volkov and K. B. Efetov. Odd spin-triplet superconductivity in a multilayered superconductor-ferromagnet Josephson junction. *Phys. Rev. B*, 81:144522, 2010.
- [95] L. Trifunovic and Z. Radović. Long-range spin-triplet proximity effect in Josephson junctions with multilayered ferromagnets. *Phys. Rev. B*, 82:020505, 2010.
- [96] The term "spin filtering" often refers to tunneling through magnetic insulators – either of single electrons or of electron pairs in Josephson junctions. but spin filtering is also an intrinsic property of metallic ferromagnets and their interfaces.

- [97] Jagadeesh S Moodera, Tiffany S Santos, and Taro Nagahama. The phenomena of spin-filter tunnelling. *Journal of Physics: Condensed Matter*, 19(16):165202, apr 2007.
- [98] Zoe H. Barber Kartik Senapati, Mark G. Blamire. Spin-filter Josephson junctions. *Nature Materials*, 10(849), 2011.
- [99] A. F. Volkov F. S. Bergeret, A. Verso. Spin-polarized Josephson and quasiparticle currents in superconducting spin-filter tunnel junctions. *Physical Review B*, 86(060506), 2012.
- [100] J. Bass in Spin Transport, Magnetism edited by E. Tsymbal, and I. Zutic. *Spin Transport and Magnetism*. CRC Press, 2011.
- [101] P.M. Levy S.F. Zhang. Conductivity perpendicular to the plane of multilayered structures. *Journal of Applied Physics*, 69(4786), 1991.
- [102] S.F. Lee, W.P. Pratt, Q. Yang, P. Holody, R. Loloee, P.A. Schroeder, and J. Bass. Giant magnetoresistance in magnetic nanostructures. *Journal of Magnetism and Magnetic Materials*, 136:335–359, 1994.
- [103] A. Fert T. Valet. Theory of the perpendicular magnetoresistance in magnetic multilayers. *Physical Review B*, 48(7099), 1993.
- [104] J. Bass. CPP magnetoresistance of magnetic multilayers: A critical review. *J. Magn. Mater.*, 408:244 – 320, 2016.
- [105] H. Y. T. Nguyen, R. Acharyya, E. Huey, B. Richard, R. Loloee, W. P. Pratt Jr., J. Bass, S. Wang, and K. Xia. Conduction electron scattering and spin flipping at sputtered Co/Ni interfaces. *Phys. Rev. B*, 82:220401, 2010.
- [106] A. Buzdin. Direct Coupling Between Magnetism and Superconducting Current in the Josephson φ_0 Junction. *Phys. Rev. Lett.*, 101:107005, Sep 2008.
- [107] Jun-Feng Liu and K. S. Chan. Anomalous Josephson current through a ferromagnetic trilayer junction. *Phys. Rev. B*, 82:184533, Nov 2010.
- [108] I Margaris, V Paltoglou, and N Flytzanis. Zero phase difference supercurrent in ferromagnetic Josephson junctions. *Journal of Physics: Condensed Matter*, 22(44):445701, oct 2010.
- [109] S V Bakurskiy, N V Klenov, T Yu Karminskaya, M Yu Kupriyanov, and A A Golubov. Josephson ϕ -junctions based on structures with complex normal/ferromagnet bilayer. *Superconductor Science and Technology*, 26(1):015005, nov 2012.
- [110] Iryna Kulagina and Jacob Linder. Spin supercurrent, magnetization dynamics, and φ -state in spin-textured Josephson junctions. *Phys. Rev. B*, 90:054504, Aug 2014.

- [111] M. A. Silaev, I. V. Tokatly, and F. S. Bergeret. Anomalous current in diffusive ferromagnetic Josephson junctions. *Phys. Rev. B*, 95:184508, May 2017.
- [112] S. V. Bakurskiy, V. I. Filippov, V. I. Ruzhickiy, N. V. Klenov, I. I. Soloviev, M. Yu. Kupriyanov, and A. A. Golubov. Current-phase relations in SISFS junctions in the vicinity of $0 - \pi$ transition. *Phys. Rev. B*, 95:094522, 2017.
- [113] Subhajit Pal and Colin Benjamin. Quantized Josephson phase battery. *EPL (Europhysics Letters)*, 126(5):57002, jul 2019.
- [114] D. B. Szombati, S. Nadj-Perge, D. Car, S. R. Plissard, E. P. A. M. Bakkers, and L. P. Kouwenhoven. Josephson ϕ_0 -junction in nanowire quantum dots. *Nature Physics*, 12(6):568–572, Jun 2016.
- [115] Hechen Ren, Falko Pientka, Sean Hart, Andrew T. Pierce, Michael Kosowsky, Lukas Lunczer, Raimund Schlereth, Benedikt Scharf, Ewelina M. Hankiewicz, Laurens W. Molenkamp, Bertrand I. Halperin, and Amir Yacoby. Topological superconductivity in a phase-controlled Josephson junction. *Nature*, 569(7754):93–98, May 2019.
- [116] Alexandre Assouline, Cheryl Feuillet-Palma, Nicolas Bergeal, Tianzhen Zhang, Alireza Mottaghizadeh, Alexandre Zimmers, Emmanuel Lhuillier, Mahmoud Eddrie, Paola Atkinson, Marco Aprili, and Hervé Aubin. Spin-Orbit induced phase-shift in Bi₂Se₃ Josephson junctions. *Nature Communications*, 10(1):126, Jan 2019.
- [117] William Mayer, Matthieu C. Dartiailh, Joseph Yuan, Kaushini S. Wickramasinghe, Enrico Rossi, and Javad Shabani. Gate controlled anomalous phase shift in Al/InAs Josephson junctions. *Nature Communications*, 11(1):212, Jan 2020.